Dissertation

submitted to the

Combined Faculty of Natural Sciences and Mathematics

of Heidelberg University, Germany

for the degree of

Doctor of Natural Sciences

Put forward by

Sebastian Hornung

born in Speyer, Germany

Oral examination: 13 July 2020

Production of (anti-)^{3}He and (anti-)^{3}H in p–Pb collisions at $\sqrt{s_{\mathrm{NN}}}$ = 5.02 TeV measured with ALICE at the LHC

Referees:

Prof. Dr. Silvia Masciocchi

apl. Prof. Dr. Monica Dunford

Abstract

In high-energy ion collisions, a medium governed by strong interactions is created and can be investigated via the particles produced during the evolution of this medium. Also light (hyper-) nuclei and their antiparticles are produced. The underlying production mechanism is not understood but usually described employing two different types of phenomenological models, the coalescence and the statistical hadronization model. The transverse-momentum differential production yields of (anti-)helium-3 and (anti-)triton measured in proton–lead collisions at a center-of-mass energy per nucleon pair of 5.02 TeV with ALICE at the LHC are presented which complement the measurements in proton–proton and lead–lead collisions. The measurements confirm a smooth evolution of the production yields with the size of the produced medium. For the first time, a direct comparison of statistical hadronization and coalescence model predictions with data is performed for the coalescence parameter and the ^{3}He-to-proton yield ratio. In contrast to the expectation of the coalescence model, the coalescence parameter obtained from the measurement of (anti-)^{3}He increases with transverse momentum. A new observable, the ^{3}H-to-^{3}He yield ratio, is measured and its capability to distinguish between models is discussed. In addition, an upper limit on the production of $^4\overline{\mathrm{He}}$ nuclei based on the non-observation of candidates is reported.

Zusammenfassung

In hochenergetischen Ionenkollisionen entsteht ein Medium, das von der starken Wechselwirkung beherrscht wird und welches durch Teilchen untersucht werden kann, welche im Zuge der Entwicklung dieses Mediums entstehen. Unter anderem werden auch leichte Atomkerne, Hyperkerne und ihre Antiteilchen produziert. Der zugrunde liegende Produktionsmechanismus ist nicht verstanden, wird aber häufig unter Verwendung von zwei verschiedenen Arten phänomenoclogischer Modelle beschrieben, dem Koaleszenz- oder dem statistischen Hadronisierungsmodell. Die transversalimpulsabhängigen Produktionsraten von (Anti-)Helium-3 und (Anti-)Tritonen in Proton-Blei-Kollisionen bei einer Schwerpunktsenergie pro Nukleonenpaar von 5.02 TeV wurden mit Hilfe des ALICE Detektors am LHC gemessenen. Diese ergänzen die Messungen in Proton-Proton- und Blei-Blei-Kollisionen. Die Messungen bestätigen eine gleichmäßige Entwicklung der Produktionsrate mit der Größe des in der Kollision entstandenen Mediums. Zum ersten Mal wird ein direkter Vergleich der Vorhersage des statistischen Hadronisierungs- und des Koaleszenzmodells mit den experimentellen Ergebnissen für den Koaleszenzparameter und das Verhältnis der Produktionsraten von ^{3}He und Protonen durchgeführt. Im Gegensatz zur Erwartung des Koaleszenzmodells, nimmt der aus der Messung von (Anti-)^{3}He erhaltene Koaleszenzparameter mit dem Transversalimpuls zu. Eine neue beobachtbare Größe, das Verhältnis der Produktionsraten von ^{3}H zu ^{3}He, wird gemessen und ihr Potenzial zur Unterscheidung zwischen den Modellen diskutiert. Außerdem wird eine Obergrenze für die Produktionsrate von $^4\overline{\mathrm{He}}$-Kernen bestimmt, die auf der Nichtbeobachtung entsprechender Kandidaten beruht.

Contents

1. Introduction

Throughout history mankind developed several ideas to describe the universe and how it was created. The current cosmological model, the standard Big-Bang model [1], requires very specific initial conditions which can be provided by introducing the hypothesis of inflation[2]. The evolution of our universe is sketched in Figure 1.1.

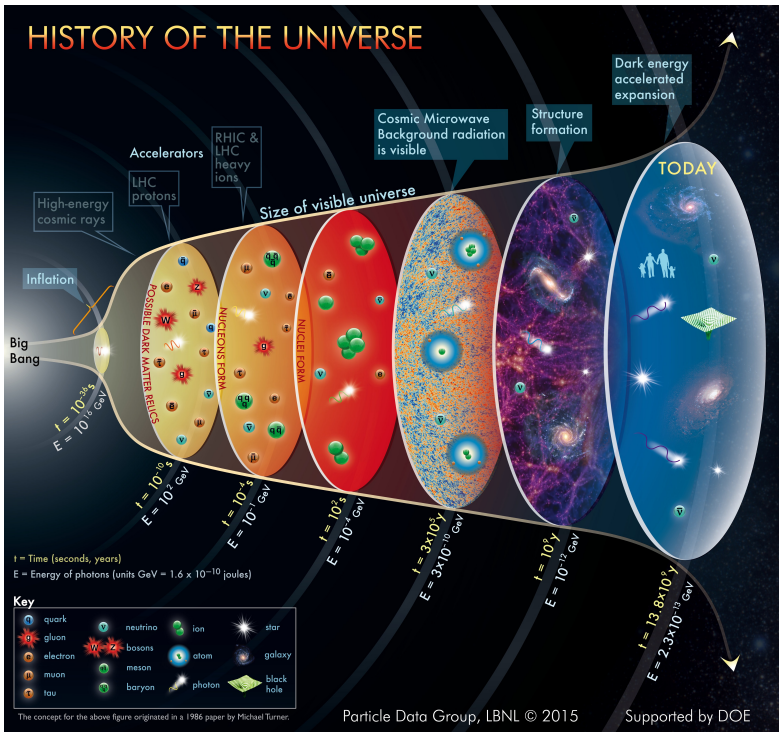

Figure 1.1: Scheme of the evolution of the universe in the Big-Bang scenario of the Standard Model of cosmology provided by the Particle Data Group at Lawrence Berkeley National Lab in 2015 [3].

The Big-Bang model including the inflation hypothesis postulates that the universe started from a very dense state, possibly even a singularity with infinite energy density. At such high energy densities, the fundamental forces described in the Standard model of Particle Physics [4], i.e. electromagnetism, weak and strong force, are expected to be unified into one single force described by a Grand Unified Theory (GUT) [1, 5, 6]. This dense state experienced a

very fast expansion reaching energy densities which were low enough that the forces were separated from each other. This phase is followed by an epoch which was governed by deconfined quarks and gluons. Due to further expansion of this medium, called quark-gluon plasma (QGP), the system cooled down further and got more and more dilute. This development led to formation of nucleons and other color-neutral particles in which quarks are confined. At some point in the evolution of the universe a not yet understood process, called baryogenesis [7], produced a net-baryon asymmetry by violating the baryon number conservation as well as charge conjugation (C)[1] and charge parity (CP) symmetry[2] [8]. In addition, the process of baryogenesis must have been taken place out of thermal equilibrium because otherwise the process which created a baryon excess would have been balanced by its reverse reaction. Due to the baryogenesis, a small fraction of matter survived the annihilation with the antimatter with which it was created during the initial stage of the universe. Thus, it is an important ingredient to the evolutionary history of our universe since no primordial antimatter in the universe is observed and the baryon density compared to the photon density is extremely low [9]. During the further evolution of the universe, light nuclei were formed and their abundances are described by the model of Big-Bang nucleosynthesis (BBN) [10]. It predicts the abundances of primordial ^{1}H, ^{2}H, ^{3}He, ^{4}He and ^{7}Li, which was one of the starting points for the invention of the Big-Bang model. The processes of the BBN led to a primordial mass fraction of about 25% for ^{4}He. The other elements are produced in much lower quantities relative to the amount of hydrogen. When the nuclei and the electrons combined into atoms, electromagnetic radiation decoupled from matter. Due to the further expansion of the universe, this radiation has cooled down to 2.73 K today and can be measured as the cosmic microwave background radiation (CMB) [11, 1]. Detailed analysis of the temperature and angular power spectrum of the CMB allow to extract information about the early universe, e.g. its baryon density [9]. Due to slight density fluctuations in the distribution of matter, which originate from initial quantum fluctuations, structure formation sets in via gravitational processes. A more detailed description of the evolution of our universe can be found in [12] and references therein.

The first few microseconds of the universe after elementary particles have been formed are an important phase during the evolution of the universe and physicists all over the world investigate the production and interactions of particles as well as the properties of the QGP.

[1] If the laws of physics are left unchanged under the change of the sign of all charges, i.e. the electrical charge, the baryon number, lepton number, the flavour numbers, and the isospin, the underlying theoretical description is C-symmetric.

[2] If the laws of physics altered under the combination of charge conjugation and at the same time inverting the spatial coordinates, CP symmetry is violated.

The QGP can experimentally only be produced in ultra-relativistic heavy-ion collisions where it lasts only for a tiny fraction of seconds ($\approx$ 10 fm/c) before the quarks hadronize. This lifetime is ultra short compared to the lifetime of the QGP in the early universe which was about 17 orders of magnitude longer. Also the volume of the medium produced in heavy-ion collisions is much smaller (a few 10-100 fm^3) than the size of the universe comparing at the moment when the quarks hadronize into color-neutral particles [13]. The process of hadronization and the production of light (anti-)nuclei in heavy-ion collisions is not yet fully understood.

Throughout the following chapter, natural units are used which implies that the speed of light c, the reduced Planck constant $\hbar$ and the Boltzmann constant k_B are set to the dimensionless value of one and thus are omitted in the mathematical formulations.

1.1. Quantum chromodynamics

The interaction of elementary particles is described via four different fundamental forces, i.e. electromagnetism, weak and strong interaction as well as gravitation. Since gravity has only a negligible influence on the particle physics processes and is difficult to describe in similar way as the other forces, the Standard Model of Particle Physics (SM) does only contain the other three fundamental forces. It describes the interactions of the building blocks of ordinary matter, i.e. quarks and leptons. The interactions are mediated via the gauge bosons which are the photons for the electromagnetic, the Z and W bosons for the weak, and the gluons for the strong interaction. In addition, the Higgs boson is included in the SM which is linked to the mechanism giving mass to the elementary particles [14, 15, 16]. Despite the fact that effects from electromagnetism and gravitation are most commonly known from our every day life, the strong interaction has the largest magnitude. It is responsible for keeping the quarks confined into hadrons and for the formation of atomic nuclei by binding protons and neutrons together. The strong force is described by quantum chromodynamics (QCD) which is a non-abelian relativistic field theory with an explicit local SU(3) gauge invariance. It can be expressed in terms of the following Lagrangian function

$$\mathscr{L}_\mathrm{QCD} = \sum_q \bar{\psi}_{q,k} \left(i\gamma^\mu (D_\mu)_{kl} - m_q \delta_{kl} \right) \psi_{q,l} - \frac{1}{4} G^a_{\mu\nu} G^{\mu\nu}_a \text{ with} \tag{1.1}$$

$$G^a_{\mu\nu} = \partial_\mu A^a_\nu - \partial_\nu A^a_\mu + g_\mathrm{s} f^{abc} A^b_\mu A^c_\nu \text{ and} \tag{1.2}$$

$$(D_\mu)_{kl} = \partial_\mu \delta_{kl} - i g_\mathrm{s} A^a_\mu \frac{(\lambda_a)_{kl}}{2}, \tag{1.3}$$

where $\psi_{q,l}$ is the quark field spinor with flavour q and color l and A^a_μ describes the gluon fields of type a. The theory includes three different color and anticolor charges, as well as, eight gauge bosons, which are called gluons. The gluons themselves carry color charge. The indices μ, ν label the space-time coordinates. The connection to the spinor space is done using the Dirac matrices γ^μ. The interaction of quarks and gluons is decoded in the first part of the equation which contains the gauge covariant derivative $(D_\mu)_{kl}$ with the Gell-Mann matrices λ_a. The current masses of the quarks and the coupling constant of the theory are given by m_q and g_s, respectively. The gluon field tensor $G^a_{\mu\nu}$ contains an additional part $(g_\mathrm{s} f^{abc} A^b_\mu A^c_\nu)$ compared to the field tensor for photons in quantum electrodynamics (QED) which results into two self-interaction vertices for gluons, the 3-gluon and 4-gluon vertices. f^{abc} is the structure constant of the SU(3) which is defined by $[\lambda_a, \lambda_b] = 2i f_{abc} \lambda_c$. Experimentally only color-neutral objects can be observed which indicates that colored objects have to be confined into color-neutral states. This effect, called color confinement, is believed to be caused by the intergluonic interactions [4]. The process of confinement is not yet fully understood and there is no analytic proof for its existence. Nevertheless, the concept can be understood by thinking about the processes happening if one tries to separate a quark-antiquark pair. The quark and the antiquark will interact via the exchange of virtual gluons. These gluons feel an attractive interaction due to the gluonic self-interaction which results in a color tube between the quark and the antiquark. If the distance becomes large enough, the energy density is constant inside the tube and the energy stored is proportional to the distance of the pair. Thus, the energy needed to separate the pair becomes increasingly large until a new quark-antiquark pair is produced.

Another effect caused by the gluonic self-interaction is that interacting particles see a smaller color charge the closer they come to each other [17]. This effect is called antiscreening and leads to a decreasing strength of the QCD interactions with increasing energy scale of the interaction. Due to this decreasing trend of the QCD coupling constant, quarks can be considered ”free” in the limit of infinitely large energies. A possible characterization of the energy scale of an interaction is the momentum transfer Q. The behaviour of the strong coupling constant, $\alpha_\mathrm{S} = g_\mathrm{s}^2/(4\pi)$, was confirmed by measuring its value for processes at different Q as shown in Figure 1.2 [1]. Since QCD is not analytically solvable, the calculation of the properties of hadrons and processes governed by the strong interaction has to be done using perturbative or non-perturbative techniques. For processes involving a large momentum transfer Q and the strong coupling constant $\alpha_S \ll 1$, a perturbative approach can be used. At low energies, the coupling constant become large, $\alpha_S \approx O(1)$, and non-perturbative approaches, like Lattice QCD (LQCD) [18], have to be used. In LQCD, the calculations are done on a

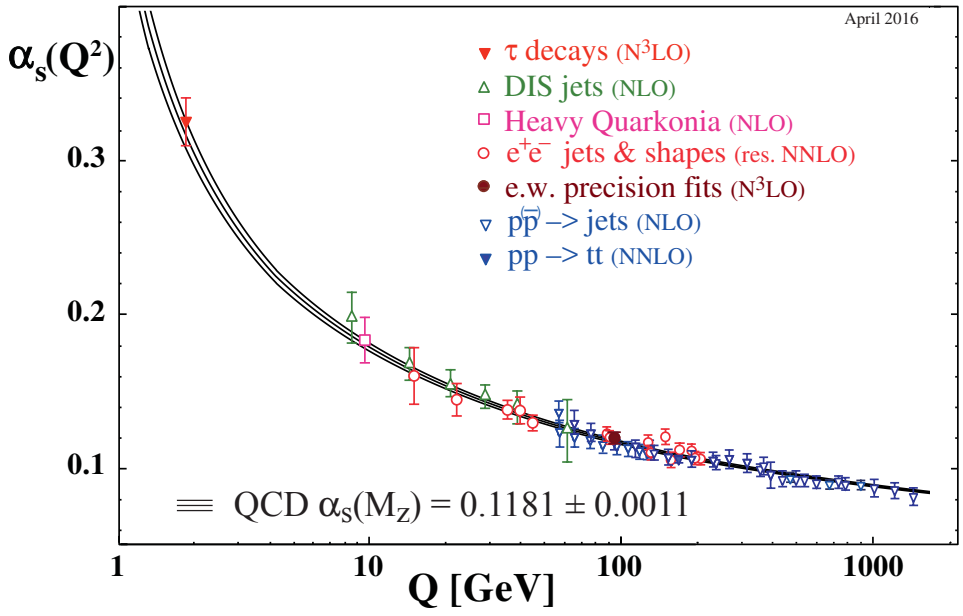

Figure 1.2: Evolution of the strong coupling constant α_s as a function of the energy scale given by the transferred momentum Q. This figure is taken from [1].

discretized Euclidean space-time lattice with a spacing which acts as an ultraviolet cut-off. The quarks are put on the sites of the lattice while the gluons are placed on the links between the sites. On this lattice, the path integral, involved in the calculation of the physical quantities of interest, can be solved numerically and the continuum limit of the result has to be evaluated by extrapolating to the limit of zero lattice spacing. An alternative option to address QCD phenomena within certain limits is the usage of QCD-inspired models, like the MIT bag [19] and the Quark-Meson model [20, 21], or effective field theories [22]. In the MIT bag model, hadrons are treated as color-neutral bags with finite dimensions embedded into the non-perturbative QCD vaccum. Inside these bags, the quarks are massless and interact only weakly. The quark and gluon fields are confined to the bag. All the non-perturbative physics outside the bag is included in one universal quantity, the bag constant, which can be interpreted as a pressure acting against the kinetic energy of the quarks. In the Quark-Meson model, the fundamental degrees of freedom are mesons which couple to quarks.

1.1.1. States of QCD matter

Based on the concept of asymptotic freedom, a new state of QCD matter was predicted for high energy densities reached at high temperatures [23] and/or high net-baryon densities [24]. This state, called quark-gluon plasma, is characterized by quarks and gluons which can be considered deconfined within the medium. The landscape of QCD matter can be summarized in the QCD phase diagram sketched in Figure 1.3. At low net-baryon densities and high tem-

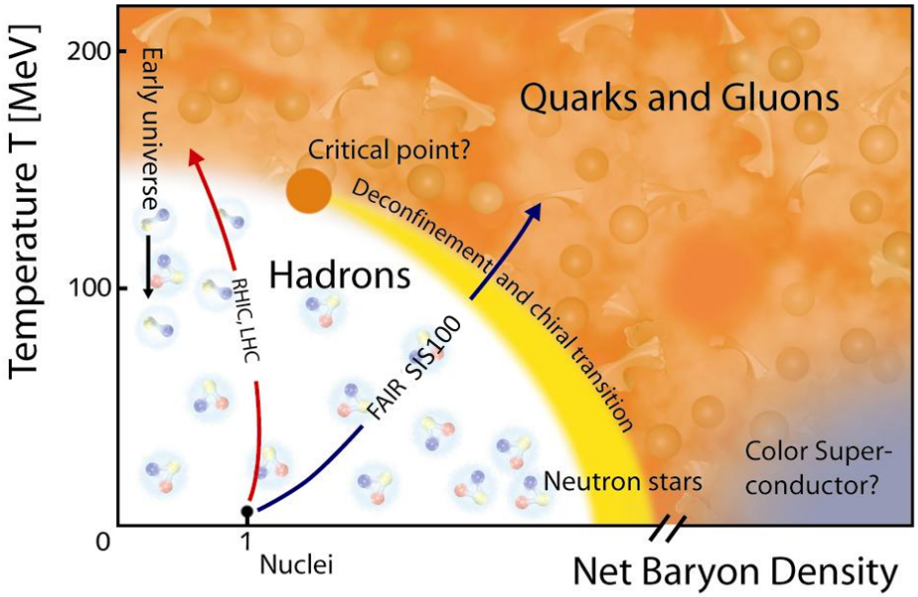

Figure 1.3: The QCD phase diagram is sketched including a critical point together with typical trajectories of heavy-ion collisions at the LHC, at RHIC and at FAIR. The figure is taken from [25].

peratures, LQCD calculations indicate that the change from hadronic matter to the QGP is of cross-over type, which means that it takes place without discontinuities in the thermodynamic quantities or their derivatives. The critical temperature at which the transition takes place is $T_C = 155 \pm 1\,(\text{stat.}) \pm 8\,(\text{syst.})$ MeV at vanishing net-baryon density [26] which corresponds to a critical energy density of about $\varepsilon_C = 0.5$ GeV/fm^3 [27]. At larger densities, first principle calculations are not possible anymore because the determinant of the covariant derivative becomes complex and an interpretation as a probability is not possible anymore. As a consequence, different contributions to the process of interest cannot be sampled according to their probability or importance. Due to this effect, which is called the fermion sign problem [28], LQCD cannot be applied anymore and QCD-inspired models have to be used. Such models

predict a decreasing critical temperature with increasing density and a first order phase transition from the hadronic phase to the QGP. Due to the different type of phase transition at zero and high net-baryon densities, the existence of a critical endpoint is expected. In addition, the formation of a color superconducting phase had been predicted for high densities and low temperatures [29, 30] in which quarks form pairs similar to the Cooper pairs known from electromagnetic superconductors.

The QCD phase diagram can be studied experimentally by the investigation of relativistic heavy-ion collision. At the Relativistic Heavy Ion Collider (RHIC) at the Brookhaven National Laboratory, Upton, New York, in the United States of America or the Large Hadron Collider (LHC) [31] at CERN near Geneva, Switzerland, this is done for the region of very high temperatures and small to nearly vanishing net-baryon densities. Thanks to the beam energy scan program at RHIC [32], a search for the critical endpoint can be performed. The region of high net-baryon densities will be explored by the future Compressed Baryonic Matter experiment [33] at the Facility for Antiproton and Ion Research (FAIR), currently under construction in Darmstadt, Germany. The high net-baryon density which will be accessible for CBM will allow to perform a search for the critical endpoint and to study the first order phase transition.

1.2. Heavy-ion collisions

If the energy density produced in relativistic heavy-ion collisions is above $\varepsilon_C = 0.5$ GeV/fm^3, a deconfined phase of QCD matter, the QGP, is created. At the LHC, its lifetime, which is about $\tau = 10$ fm/c [34], is long enough to form an equilibrated state but not long enough to study the properties of the QGP with external probes. As a consequence, either particles which are produced inside the QGP or particles produced at the very early stage of the collision, which interact with the QGP, have to be used. The signatures of the QGP carried by these particles can be modified by interactions in the later stage of collision. Therefore, a good understanding of the full evolution of the heavy-ion collision is needed. In the following sections, the space-time evolution of a heavy-ion collision as well as the procedure to determine its initial collision geometry is described. The collision geometry is an important ingredient to model the initial conditions of the collision correctly. Afterwards, selected observables used to investigate the QGP and the other stages of the collision are discussed.

1.2.1. Space-time evolution of heavy-ion collisions

The space-time evolution of a heavy-ion collision is sketched in Figure 1.4. If the produced energy density is larger than the critical value at which the phase transition from confined matter to the QGP takes place, the evolution of the system can be separated into a pre-equilibrium, a QGP, and a hadron gas phase before the produced particles escape as free streaming particles. These stages will be discussed in more detail in the following.

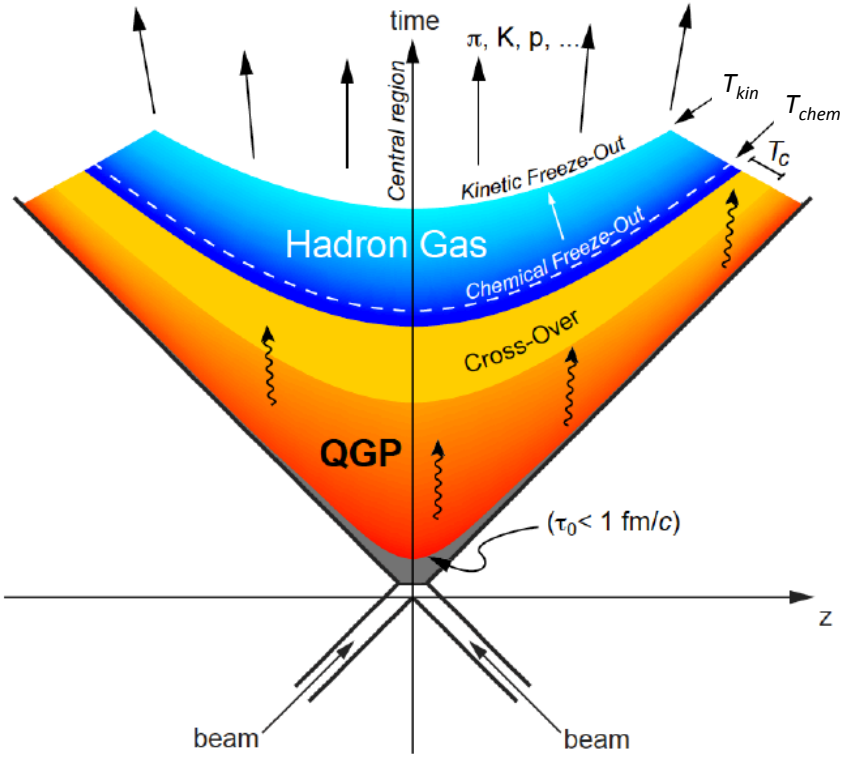

Figure 1.4: The evolution of a heavy-ion collision with an energy density high enough to form a QGP. The two nuclei collide at the time $t = 0$ and the longitudinal position $z = 0$. The temperature T_C characterizing the system at the transition from QGP to hadron gas, as well as the one of the chemical, T_{chem}, and kinetic, T_{kin}, freeze-out are indicated. The figure is taken from [35].

Before the collision which takes place at $t = 0$ fm/c the two nuclei move towards each other at almost the speed of light and, thus, they are strongly Lorentz contracted. At the initial stage of the collision, a large number of deconfined quarks and gluons are produced via hard and soft parton scatterings. These particles interact via inelastic and elastic collisions until the system reaches a local thermal equilibrium after a proper time $\tau = \sqrt{t^2 - z^2}$ of about 1 fm/c. Only during this initial stage, hard scattering processes between the incoming quarks and gluons

take place and particles can be produced with a large momentum transfer, e.g. heavy quarks or high-momentum quarks which hadronize and emerge as jets. Quantum fluctuations of the color charge, e.g. due to fluctuation of the distribution of nucleons inside the nuclear wave functions or the distribution of the color charge inside the nucleons, lead to event-by-event fluctuating energy densities. These initial state fluctuations can be investigated e.g. via flow observables (see section 1.2.3). There are several approaches to model the initial stage of the collision, e.g. the Glauber [36], IP-Glasma [37], TRENTo [38] and EKRT [39] model. For the sake of brevity, only the first two of these models, which are frequently used, are briefly discussed but further information about all the models can be found following the provided references.

The Glauber model treats the collision as a sequence of binary nucleon-nucleon collisions where the nucleons are assumed to move on straight lines which remain unchanged by subsequent collisions. In addition, the inelastic nucleon-nucleon cross section is assumed to be unaltered by the number of previous collisions. Glauber model calculations are performed in the optical limit [40] which assumes a smooth density inside the colliding nuclei and no event-by-event local density fluctuations are included. The interaction probability of the two nucleons in the colliding nuclei A and B is given by the product of the measured inelastic nucleon-nucleon cross section, σ_{NN}, and the nuclear thickness function, T_{AB}. The latter can be interpreted as the effective overlap area for which a given nucleon from the nucleus A can interact with a given nucleon of the nucleus B. It is expressed as a function of the impact parameter of the two colliding nuclei, which is the distance of the centers in the plane transverse to the beam direction. Thanks to the invention of desktop computers, a simulation approach for the Glauber model was developed, the Glauber Monte Carlo (GMC)[36]. In the GMC simulation approach, the nuclei are initialized as uncorrelated nucleons sampled following the measured density distributions. The impact parameter b between the two nuclei is chosen randomly following the distribution $\mathrm{d}\sigma/\mathrm{db} = 2\pi\mathrm{b}$ where σ denotes the (geometrical) interaction cross section. Two nucleons interact if the Euclidean transverse difference between their centers is smaller than $D = \sqrt{\sigma_{\mathrm{NN}}/\pi}$.

Another approach is realized in the IP-Glasma model which combines the impact parameter dependent saturation model (IP-Sat) [41] with dynamics described by flowing Glasma gluon fields. The IP-Sat model is used to determine the configuration of the color charges in the two colliding nuclei by sampling the nucleon positions and the color charge per nucleon. At high energies, the density of the partons in the hadronic wave functions becomes very large leading to the saturation of the partonic distributions. This medium can be described by the Color Glass Condensate (CGC) effective theory [42]. In the collision of the two nuclei, non-

equilibrium matter is produced in which the frozen CGC degrees of freedom are melted and which develops into a QGP, the so-called Glasma [43].

Due to the internal thermodynamic pressure, the system expands and cools down until the critical temperature, T_C, is reached and the system turns into a hadron gas. Especially, for collisions at higher net-baryon densities, where the phase transition could be of first order, the existence of a mixed phase is being discussed [44, 45]. When the rate of inelastic collisions between the hadrons becomes negligible, the chemical freeze-out takes place at which the relative abundances of the particle species are fixed. The system at the chemical freeze-out is characterized by the temperature T_{chem}, which is found to be 156.5 ± 1.5 MeV in lead–lead (Pb–Pb) collisions at $\sqrt{s_{\mathrm{NN}}} = 2.76$ TeV at the LHC [46]. The momentum distributions of the particles might still change due to elastic collisions. The medium expands until it becomes dilute enough that also elastic collisions cease and the kinetic freeze-out occurs. The resulting particles freely stream out of the collision zone and are measured with particle detectors or might decay on the way.

1.2.2. Collision geometry

Due to the extended size of the colliding nuclei, the region in which the nucleons interact depends on the impact parameter b, which is the distance of the centers of colliding ions in the plane transverse to the beam direction as indicated in Figure 1.5. In the most central collisions, which corresponds to small impact parameter values, the nuclei collide almost head on. The overlap region is the largest and, thus, the largest number of participating nucleons[3] N_{part} and binary nucleon–nucleon collisions N_{coll} can be obtained. The overlap region becomes smaller and less circular the more peripheral the two nuclei collide, i.e. for larger b. Thus, events can be characterized using the centrality according to the size and shape of the overlap region. Unfortunately, neither the impact parameter nor the number of participant nucleons or binary collisions can be measured directly. Therefore, the centrality has to be obtained by measuring related quantities, like the number of spectator nucleons, i.e. nucleons which have not participated in the collisions, or the number of produced particles, the charged-particle multiplicity. The latter is assumed to decrease monotonically with increasing impact parameter which is confirmed e.g. in [48]. Based on this, the centrality is commonly expressed in centrality classes by fitting the distribution of the charged-particle multiplicity with a theoretical description obtained from a Glauber Monte Carlo simulation convoluted with a particle-production model which is based on a negative binomial distribution (NBD) [49]. The production model uses

[3] A participant nucleon is a neutron or proton from one of the nuclei which collides with at least one of the nucleons of the other nucleus.

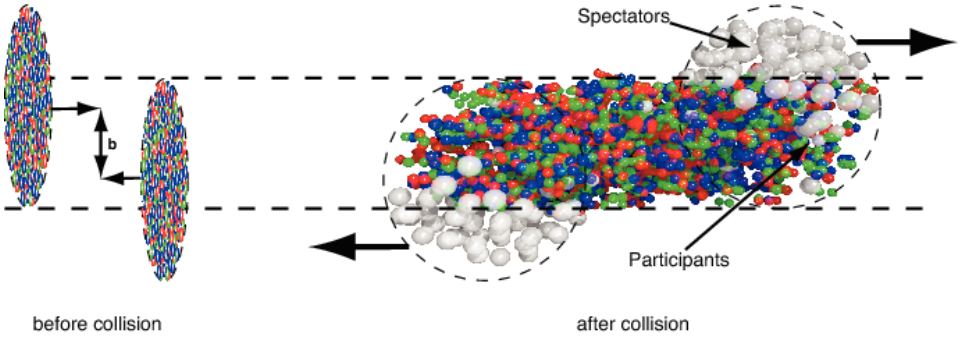

Figure 1.5: Left: The two heavy ions before the collision with impact parameter b. Right: The spectators continue unaffected, while in the overlap region interactions take place [47].

a two-component approach. One component for particles produced in hard initial scattering processes, which scale with N_{coll}. The rest of the particles are assumed to be produced in soft interactions and, thus, the number is proportional to N_{part}. The NBD-based model was chosen because it succeeds in describing the charged-particle multiplicity measured in high-energy proton-proton (pp) collisions over a wind range of rapidity [50]. This allows to define centrality classes as percentiles of the total integral of the charged-particle multiplicity distribution in Monte Carlo and data. Hereby, the most central collisions are identified with values close to 0% while the most peripheral ones belong to the percentile range close to 100%. For example, the 5-10% most central collisions are the ones with a multiplicity in between n_5 and n_{10} given by

$$\frac{\int_{n_5}^{\infty} \frac{\mathrm{d}N_{\mathrm{ev}}}{\mathrm{d}N_{\mathrm{ch}}} \mathrm{d}N_{\mathrm{ch}}}{\int_{0}^{\infty} \frac{\mathrm{d}N_{\mathrm{ev}}}{\mathrm{d}N_{\mathrm{ch}}} \mathrm{d}N_{\mathrm{ch}}} = 0.05 \quad \text{and} \quad \frac{\int_{n_{10}}^{\infty} \frac{\mathrm{d}N_{\mathrm{ev}}}{\mathrm{d}N_{\mathrm{ch}}} \mathrm{d}N_{\mathrm{ch}}}{\int_{0}^{\infty} \frac{\mathrm{d}N_{\mathrm{ev}}}{\mathrm{d}N_{\mathrm{ch}}} \mathrm{d}N_{\mathrm{ch}}} = 0.1 \tag{1.4}$$

This is indicated in Figure 1.6 where the amplitude measured in the ALICE V0 detector is used as a proxy for the charged-particle multiplicity. A more detailed discussion of the determination of the event centrality can be found in [51].

1.2.3. Signals from the QGP

A personal selection of observables used to investigate the QGP and other stages of a heavy-ion collision is given in this subsection.

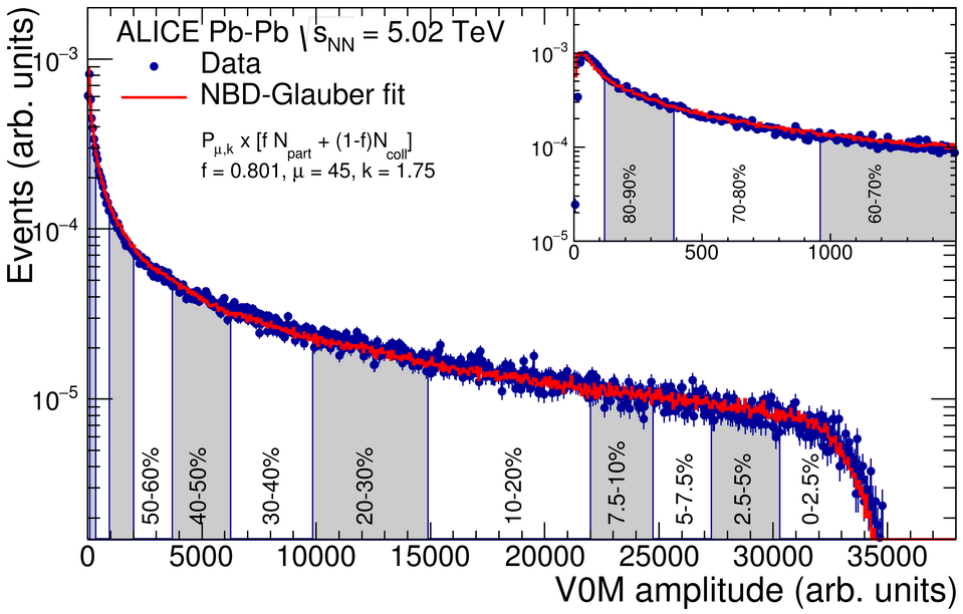

Figure 1.6: The distribution of the charged-particle multiplicity, approximated by the sum of the amplitudes observed in the V0 scintillators of ALICE, as presented in [52]. The distribution is fitted with a NBD-Glauber parametrization shown as a red line. The insert shows a zoom of the most peripheral region.

Hard probes

In the initial stage of the collision, scattering processes of partons with a large momentum transfer lead to the production of particles with high momenta or masses, e.g. heavy quarks (i.e. charm and beauty quark). These particles propagate through the QGP and, if they carry color change, interact strongly with its color-charged constituents and thereby lose energy. This medium induced energy loss can be quantified using the nuclear modification factor R_{AA} because the production via hard processes is expected to scale with the number of binary nucleon-nucleon collisions. The R_{AA} is defined as

$$R_{\mathrm{AA}}(p_{\mathrm{T}}) = \frac{1}{\langle N_{\mathrm{coll}} \rangle} \frac{\mathrm{d}N_{\mathrm{AA}}/\mathrm{d}p_{\mathrm{T}}}{\mathrm{d}N/\mathrm{d}p_{\mathrm{T}}}, \tag{1.5}$$

where $\mathrm{d}N_{\mathrm{AA}}/\mathrm{d}p_{\mathrm{T}}$ and $\mathrm{d}N/\mathrm{d}p_{\mathrm{T}}$ are the p_{T}-differential yields of the particle measured in A–A and pp collisions, respectively. $\langle N_{\mathrm{coll}} \rangle$ denotes the mean number of nucleon–nucleon collisions for the respective collision type, e.g. centrality class, studied.

If there is no medium-induced energy loss, the R_{AA} of hard probes should be equal to unity. A value below unity is expected for hard probes with color-charged constituents, like high momentum hadrons or hadrons containing heavy quarks. This expectation is experimentally

confirmed as shown in Figure 1.7 where the R_{AA} as a function of the transverse momentum (p_{T}) for unidentified charged particles measured in Pb–Pb collisions by CMS and ALICE is shown. For the charged hadrons ($h^{\pm}$) with $p_{\mathrm{T}} > 8$ GeV/c, a strong suppression is observed.

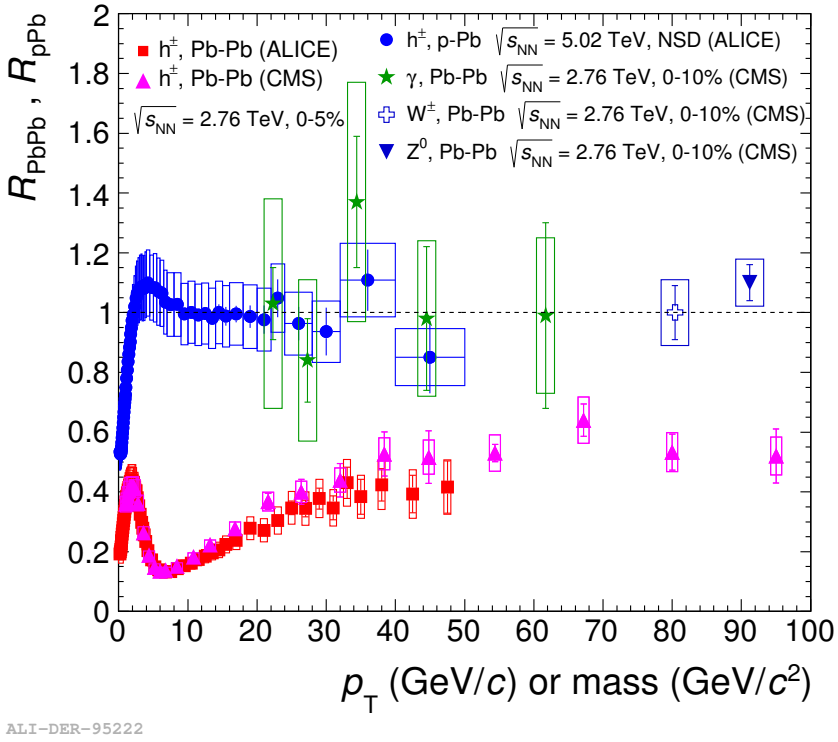

Figure 1.7: The nuclear modification factor R_{PbPb} of charged particles ($h^{\pm}$) measured by ALICE and CMS in central Pb–Pb collisions at $\sqrt{s_{\mathrm{NN}}} = 2.76$ TeV is shown as a function of the transverse momentum. In addition, the results for the direct photons, Z and W bosons from CMS are displayed. To indicate the behaviour coming from cold nuclear matter effects, the R_{pPb} measured in p–Pb collisions at $\sqrt{s_{\mathrm{NN}}} = 5.02$ TeV by ALICE is presented as well. The figure was taken from [53].

As expected, the nuclear modification is compatible with unity for hard probes which do not carry color charge or color-charged constituents, i.e. Z and W bosons, as well as photons with a high momentum. The R_{pPb}, which is calculated using the measured yield in proton–lead (p–Pb) collisions instead of the Pb–Pb result, indicates the impact of cold nuclear matter effects. These are mainly the modifications of the parton distribution functions of the neutrons and protons inside the nuclei as well as the Cronin effect [54]. The later describes the enhancement of high-p_{T} hadrons emitted from nucleons bound in the colliding nuclei. This effect is caused by multiple interactions of the nucleons in nuclear matter and is responsible for the peak of the R_{pPb} at $p_{\mathrm{T}} \approx 3$ GeV/c. The fact that the R_{pPb} is also compatible with unity ensures that the observed suppression for the charged hadrons is due to energy loss in the QGP and is

not caused by cold nuclear matter effects. For $p_{\mathrm{T}} < 8$ GeV/c, the charged hadrons are not only produced via initial hard scattering processes and their production is not expected to scale with the number of binary collisions anymore. The behavior of the R_{AA} below $p_{\mathrm{T}} = 2-3$ GeV/c is governed by collective effects and the hydrodynamic expansion of the medium produced in the collisions which will be discussed in more detail in section 1.2.3. A good description of the R_{AA} in the intermediate transverse momentum range ($2 \leq p_{\mathrm{T}} < 8$ GeV/c) is given by models containing in-medium hadronization via quark recombination [55]. As shown in Figure 1.8,

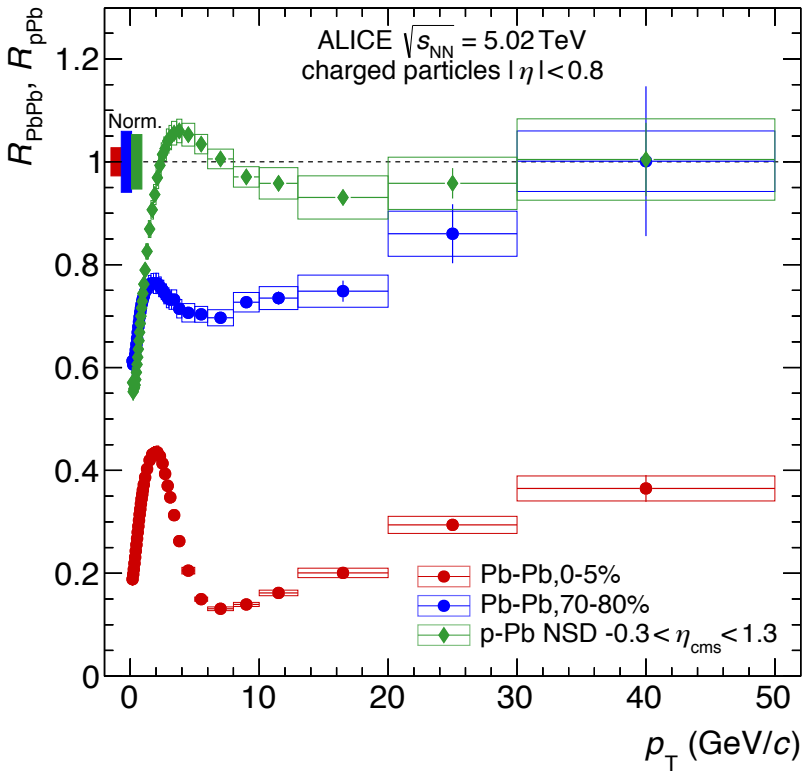

Figure 1.8: The nuclear modification factors of charged particles ($h^{\pm}$) measured by ALICE in central (0–5%) and peripheral (70–80%) Pb–Pb collisions at $\sqrt{s_{\mathrm{NN}}} = 5.02$ TeV are shown as a function of the transverse momentum. The figure was taken from [56].

the suppression of the R_{AA} is observed to be less pronounced in peripheral compared to central collisions which indicates a centrality dependence of the parton energy loss [56]. This indicates a lower density of the medium produced in peripheral compared to central collisions. With the measurements of the R_{AA} for different identified hadrons, the existence of a possible hierarchy in the energy loss can be investigated. Gluons are expected to lose more energy than the light quarks (up, down, strange) due to the color factor. In addition, the dead cone effect [57] leads to a lower energy loss for heavy quarks due to the suppression of gluon radiation at forward angles for low momenta. According to these considerations, the R_{AA} of hadrons

containing beauty quarks is expected to be less suppressed than the one of hadrons with charm quarks, while the one for hadrons containing only light quarks should show a even stronger suppression. This hierarchy of the R_{AA} is not observed for high p_{T}, where the suppression is the same within uncertainties. This indicates a vacuum-like parton fragmentation for partons leading to high-p_{T} hadrons in the final state [58]. For low p_{T}, the expected hierarchy can be observed for the heavy quarks [59] which are hard probes due to their high mass. Comparisons of the measured R_{AA} with calculations from different theoretical models containing different energy loss mechanisms, like gluon radiation and collisional energy loss, provide information about the properties of medium, e.g. its density via the transport coefficients [60, 61].

Quarkonia

Another observable which is of importance to prove the deconfinement in the QGP is the measurement of quarkonia states composed of heavy quarks and antiquarks, i.e. charmonia (like J/ψ) and bottomonia. Already in 1986, Matsui and Satz proposed that the suppression of J/ψ is an unambiguous sign for deconfinement because the color screening mechanism within the QGP prevents the resonant interaction between charm-anticharm quark pairs to become active [62]. As a consequence, J/ψ cannot be produced inside the medium anymore and the charm quark will end up in „open“ charm mesons, e.g. D mesons. Since the production is still possible at the boundary of the medium, where the energy density is low, the J/ψ yield is expected to be suppressed but not completely zero in heavy-ion collisions with a high enough energy density to from a deconfined medium compared to proton-proton collisions. This behavior was already observed in measurements at the CERN SPS [63, 64] and RHIC [65, 66]. The observation of quantitative similar suppression at the SPS and RHIC, which is in contrast to the expected increase of suppression with increasing collision energy, has lead to two possible theoretical explanations. On the one hand, the observed yield of J/ψ is only to 60% caused by direct production of J/ψ, the rest is feed-down from excited charmonium states, like ψ' and χ_c. According to LQCD calculations, the temperature of the medium produced at SPS and RHIC could be below the temperature needed to prohibit the production of J/ψ but the formation of excited charmonium states could have been prevented. Thus, the observed suppression at the SPS and RHIC could be caused by the suppression of the feed-down from excited charmonium states [67]. On the other hand, the production of charm and anticharm quark pairs is abundant at RHIC energies, which could lead to regeneration of the J/ψ signal via formation at the hadronization stage due to pairs of charm and anticharm quarks originating from different hard scattering processes [68, 69, 70]. The observation of a less suppressed J/ψ yield at the LHC compared to the observations at the SPS and RHIC, which is shown in

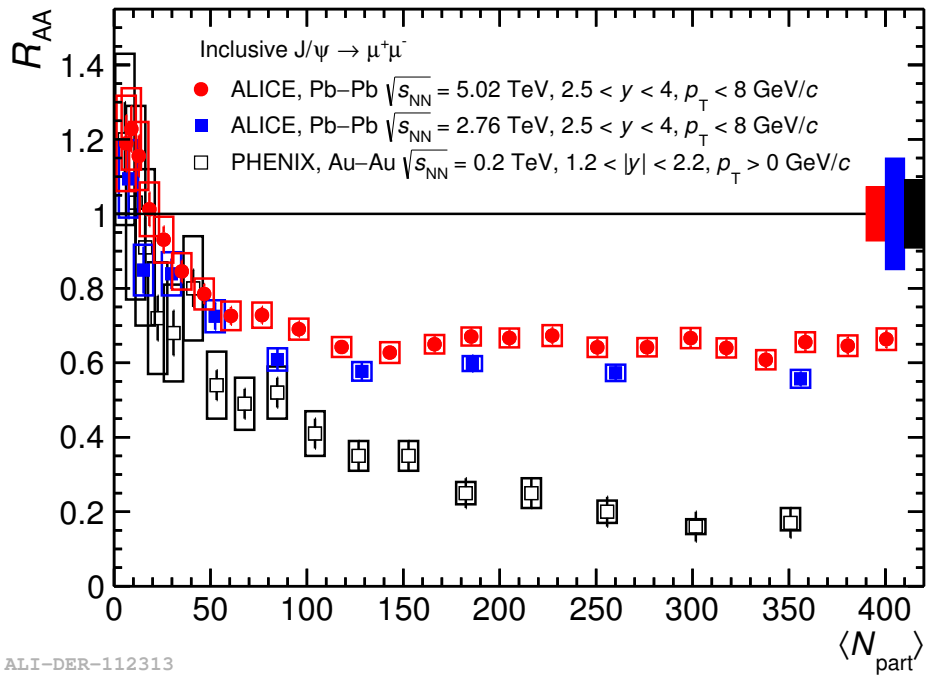

Figure 1.9: The R_{AA} of inclusive J/ψ measured in Pb–Pb collisions at $\sqrt{s_{NN}} = 5.02$ TeV by ALICE is shown in comparison to ALICE measurement at $\sqrt{s_{NN}} = 2.76$ TeV and the PHENIX results in Au–Au collisions at $\sqrt{s_{NN}} = 0.2$ TeV at forward rapidity.

Figure 1.9, as well as, the measurement of positive elliptic flow[4] of J/ψ favors the regeneration picture [71]. The high collision energy provided by the LHC allows for detailed studies of bottomonium states in addition to the already discussed charmonium states. The suppression of excited quarkonium states sets in at different temperatures depending on their binding energies which leads to the expectation of stronger suppression for increasingly higher-mass excited states [72]. As shown in Figure 1.10, this expected behavior is observed for both, the charmonium and bottomonium states measured at the LHC [73].

Radial and anisotropic flow

The measurement of hadron spectra and elliptic flow at RHIC indicated that the QGP acts like a almost ideal fluid [74]. After a quick thermalization, the dynamics of the medium produced in the collision can be described using a relativistic hydrodynamic description. The medium undergoes a rapid collective expansion caused by the thermal pressure inside the medium which acts against the surrounding vacuum. This collective flow can be observed as radial

[4]The elliptic flow is the second harmonic coefficient of the azimuthal Fourier decomposition of the invariant yield with respect to the reaction plane, as discussed in section 1.2.3

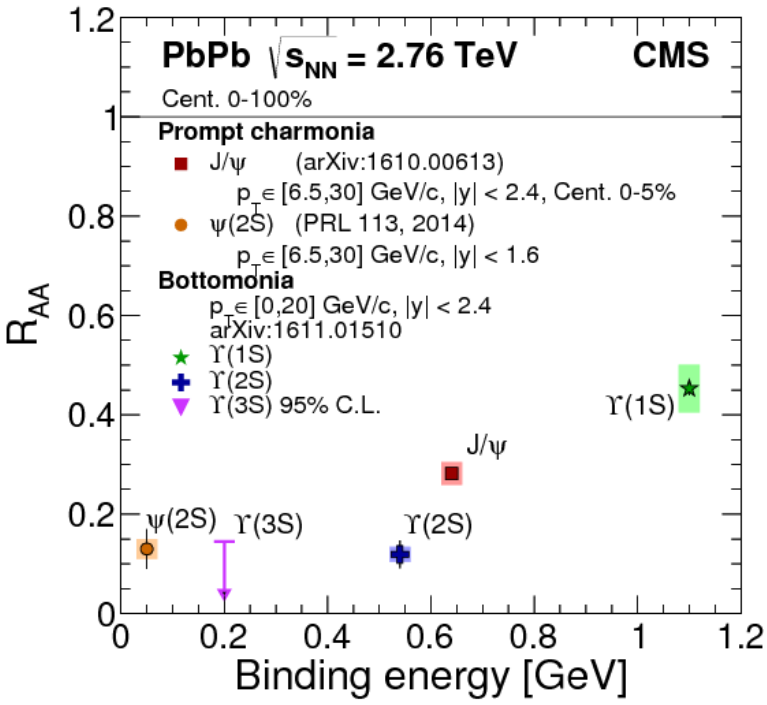

Figure 1.10: The sequential suppression pattern of S-wave quarkonium states is shown via the R_{AA} observables as a function of the binding energy of the individual quarkonium states measured in Pb–Pb collisions at $\sqrt{s_{\mathrm{NN}}} = 2.76$ TeV [73].

and anisotropic flow. Due to radial flow the maximum of the transverse-momentum spectra of hadrons is pushed to higher momenta when going from peripheral to central collisions. The bulk of the hadrons, emitted from the medium at the kinetic freeze-out, will flow with a common average transverse velocity $\langle\beta_{\mathrm{T}}\rangle$. This common average transverse expansion velocity, as well as the kinetic freeze-out temperature, T_{kin}, can be extracted from the p_{T}-spectra of different hadron species by simultaneous fits with a simplified hydrodynamical model, the Boltzmann-Gibbs Blast-Wave model [75]. According to the Blast-Wave model, the invariant yield of a given particle species is given by

$$E\frac{\mathrm{d}^3N}{\mathrm{d}^3\mathbf{p}} \approx \int_0^R m_{\mathrm{T}} I_0\left(\frac{p_{\mathrm{T}}\sinh(\rho)}{T_{\mathrm{kin}}}\right) K_1\left(\frac{m_{\mathrm{T}}\cosh(\rho)}{T_{\mathrm{kin}}}\right) r\mathrm{d}r, \tag{1.6}$$

where $m_{\mathrm{T}} = \sqrt{m^2 + p_{\mathrm{T}}^2}$ is the transverse mass. Here, I_0 and K_1 are the modified Bessel functions and the velocity profile ρ can be expressed as

$$\rho = \tanh^{-1}\beta_{\mathrm{T}} = \tanh^{-1}\left[\beta_{\mathrm{s}}\left(\frac{r}{R}\right)^n\right], \tag{1.7}$$

where β_s denotes the transverse expansion velocity at the surface and n is the exponent of the velocity profile. The radial distance in the transverse plane is expressed as r and R is the radius of the medium. The correlation between T_{kin} and $\langle\beta_T\rangle$ obtained from simultaneous fits of the

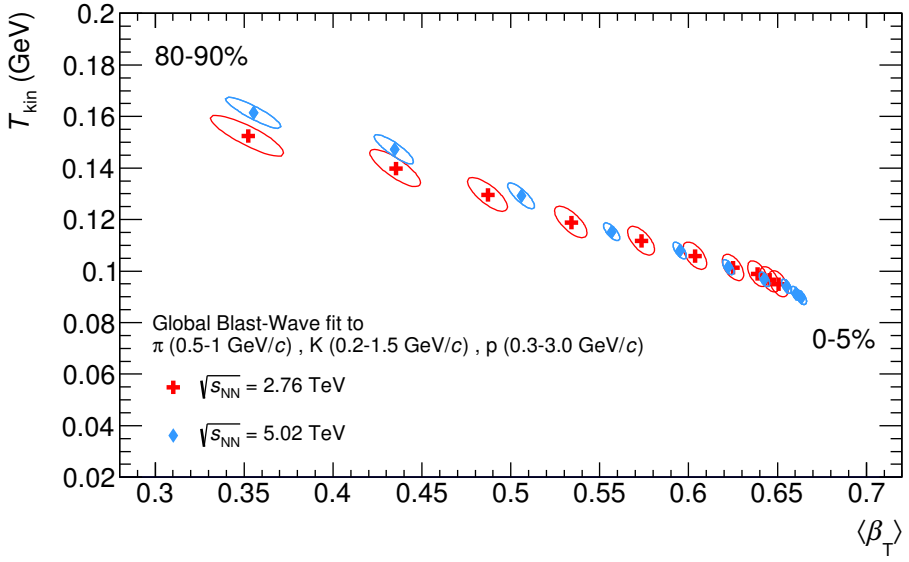

Figure 1.11: The evolution of the average expansion velocity ($\langle\beta_T\rangle$) and kinetic freeze-out temperature (T_{kin}) from the simultaneous Boltzmann-Gibbs Blast-Wave fit to the $\pi^{\pm}$, $\mathrm{K}^{\pm}$ and p($\bar{\mathrm{p}}$) spectra measured in Pb–Pb collisions at $\sqrt{s_{\mathrm{NN}}} = 2.76$ TeV and 5.02 TeV by ALICE. The correlated uncertainties from the global fit corresponding to 1σ uncertainties are shown as ellipses [76].

p_T-spectra of pions, kaons and protons measured in Pb–Pb collisions at $\sqrt{s_{\mathrm{NN}}} = 2.76$ TeV and 5.02 TeV by ALICE is shown in Figure 1.11. The mean transverse velocity is observed to increase with centrality, while T_{kin} decreases at the same time. This is compatible with a shorter lived fireball with stronger radial pressure gradients in peripheral collisions [77].

Another effect observed for many different particle yields are azimuthal angular anisotropies in (non-central) collisions. They are characterized by the coefficients v_n of the Fourier expansion of the invariant yield with respect to the reaction plane:

$$E\frac{\mathrm{d}^3N}{\mathrm{d}^3\mathbf{p}} = \frac{1}{2\pi p_T}\frac{\mathrm{d}^2N}{\mathrm{d}p_T\mathrm{d}y}\left[1+2\sum_{n=1}^{\infty} v_n \cos n(\varphi-\Psi_{\mathrm{RP}})\right]. \tag{1.8}$$

Here, E, $\mathbf{p}$ and y denote the energy, momentum and rapidity of the particle, while φ is its azimuthal angle. The reaction plane is defined by the beam axis and the impact parameter of the collision. The Fourier coefficients are given by $v_n = \langle\cos(n(\varphi-\Psi_{\mathrm{RP}}))\rangle$, where the average is done over all particles in all events. The reaction plane is not measurable but it can

be estimated e.g. using directly the anisotropic flow itself via the event-plane method. The event-plane angle Ψ_n is determined from the n-th harmonic via

$$\Psi_n = \frac{1}{n}\left(\tan^{-1}\frac{\sum_i w_i \sin(n\varphi_i)}{\sum_i w_i \cos(n\varphi_i)}\right), \tag{1.9}$$

where i is the index for the particles used in the event plane estimation and w_i are weights which are chosen such that the reaction plane resolution is optimized. A detailed discussion of the methods which can be used to evaluate the anisotropic flow coefficients can be found in [78]. In non-central collisions, the geometrical overlap region has an almond-like shape which results in an anisotropic initial matter distribution. Due to the interactions of the particles inside the medium, this spatial anisotropy is converted into a momentum anisotropy via multiple collisions, and it is expected to be measurable as non-zero even Fourier coefficients. Due to event-by-event fluctuations of the initial energy density, the shape of the events deviate

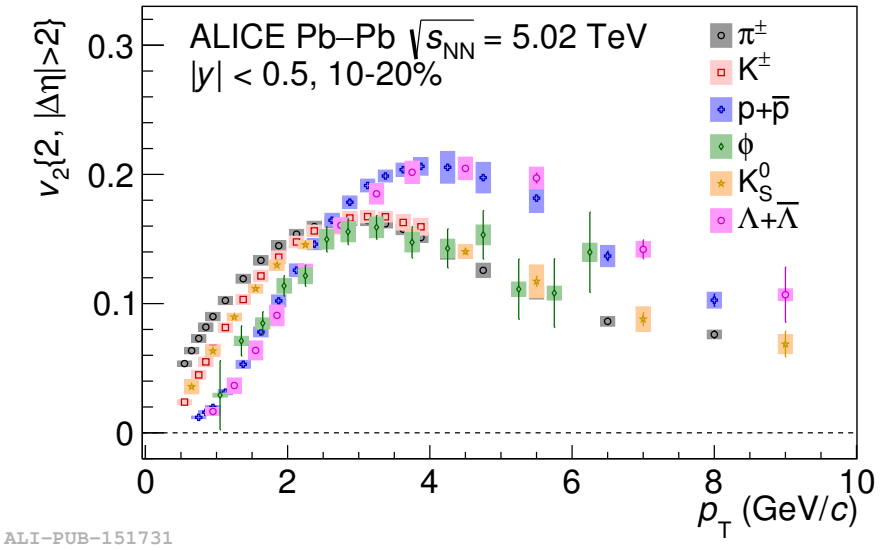

Figure 1.12: p_{T}-differential v_2 for $\pi^{\pm}$, $\mathrm{K}^{\pm}$, $\mathrm{K}^0_{\mathrm{s}}$, ϕ, $\mathrm{p}+\overline{\mathrm{p}}$ and $\Lambda+\overline{\Lambda}$ measured in 10–20% central Pb–Pb collision at $\sqrt{s_{\mathrm{NN}}} = 5.02$ TeV by ALICE [79].

from the ideal symmetric almond shape, which causes also odd Fourier coefficients to be non-zero. In Figure 1.12, the p_{T}-differential v_2 for $\pi^{\pm}$, $\mathrm{K}^{\pm}$, $\mathrm{K}^0_{\mathrm{s}}$, ϕ, $\mathrm{p}+\overline{\mathrm{p}}$ and $\Lambda+\overline{\Lambda}$ measured in 10–20% central Pb–Pb collision at $\sqrt{s_{\mathrm{NN}}} = 5.02$ TeV are summarized. For $p_{\mathrm{T}} < 2-3$ GeV/c, a mass ordering of the v_2 is observed, i.e. the v_2 of lighter particles is larger than the value for heavier particles. In addition, a grouping in mesons and baryons is found above $p_{\mathrm{T}} = 3$ GeV/c, which favours the hypothesis of particle production via quark coalescence [80]. The

crossing between baryon and meson v_2 depends on the centrality and is connected to a larger radial flow in central compared to peripheral collisions. A similar behaviour is also observed for v_3 and v_4 [79]. The v_n coefficients are related to the equation of state of the medium and its thermodynamic transport coefficients, e.g. v_2 is sensitive to the shear viscosity to entropy ratio (η/s) [81]. The latter is found to be small which indicates that the QGP can be treated as an almost ideal fluid ($\eta/s \approx 0$).

Particle correlations

In heavy-ion collisions, the size and the expansion rate of the medium at the moment of the decoupling of the particles from it can be measured via the correlation of two or more particles. The traditional way to perform such femtoscopy analyses, which is often denoted as Hanbury Brown-Twiss (HBT) intensity interferometry [82], is via correlating two identical bosons, e.g. photons or pions, and exploits the Bose-Einstein enhancement of identical bosons emitted close by in phase space [83]. Femtoscopic analyses allow to determine the width of the distribution of the relative separation between the places of emission, which are often denoted as HBT radii. In general, the HBT radii do not correspond the total size of the medium but the dimensions of the homogeneity region which is the size of the region that contributes to the particle spectrum at a particular momentum $\mathbf{p}$. These radii are calculated in the longitudinally co-moving system, in which the longitudinal pair momentum vanishes, and are decomposed into three components, R_{out}, R_{side}, and R_{long}. Following the Bertsch–Pratt convention [84, 85], the "out" axis points along the pair transverse momentum, the "side" axis is perpendicular to it in the transverse plane, and the "long" axis along the beam. The measured quantity is the two-particle correlation function, $C(k^*)$, which can be obtained by comparing the measured distribution of the relative momentum difference of the two particles, $k^* = |\mathbf{p}_1 - \mathbf{p}_2|/2$, with the corresponding distribution obtained from uncorrelated pairs. The k^* distribution of uncorrelated pairs are usually obtained using an event-mixing technique by combining each particle in a given event with each particle in several other events. Thus an appropriate normalisation factor $\mathcal{N}$ is needed. The correlation function can be fitted taking into account the two-particle interaction kernel Ψ and the two-particle source function S via the Koonin-Pratt equation [86, 87]:

$$C(k^*) = \mathcal{N}\,\frac{N_{\text{same}}(k^*)}{N_{\text{mixed}}(k^*)} = \int S(r)|\Psi(k^*, r)|^2 \mathrm{d}^3 r \tag{1.10}$$

The source function S can be interpreted as the probability density for the emission of a pair of particles with a given relative momentum, k^*, and space-time separation, r. For heavy-ion

collisions, it is usually approximated with a Gaussian function depending on the HBT radii. The kernel contains the information about all possible interaction between the two particles. In the simplest case of two non-interacting particles it can be identified as the pair wave-function. For two charged pions, the Coulomb interaction and strong final state interactions have to be taken into account and $|\Psi|^2$ is given by the Bethe-Salpeter amplitude [88]. The HBT radii

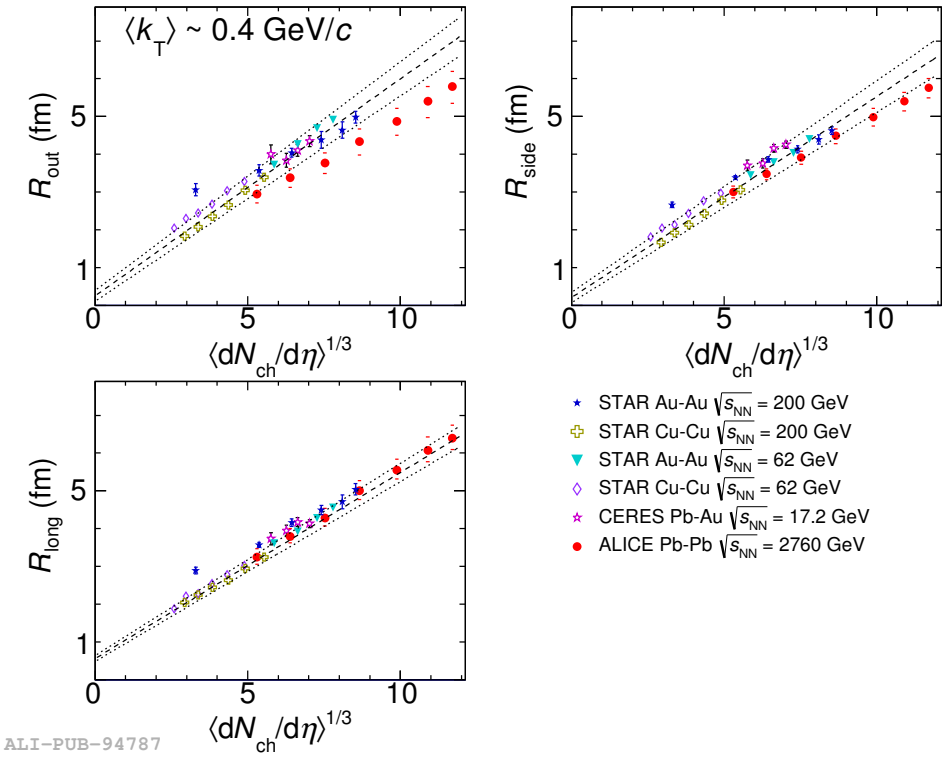

Figure 1.13: The femtoscopic radii as a function of the measured mean charged-particle multiplicity density for a number of collision systems and collision energies [89, 90, 91, 92] are compared at the value of the average transverse pair momentum $\langle k_{\mathrm{T}} \rangle$ closest to 0.4 GeV/c. Systematic uncertainties are shown where available. A linear fit to the heavy-ion data, excluding the ALICE results, is shown as a dashed line with a 1σ contour indicated by the dotted lines.

are observed to scale approximately linearly with the cubic root of the number of participant nucleons, $N_{\mathrm{part}}^{1/3}$, and with the cubic root of the final state mean charged-particle multiplicity density, $\langle \mathrm{d}N_{\mathrm{ch}}/\mathrm{d}\eta_{\mathrm{lab}} \rangle^{1/3}$ [83]. As summarized in Figure 1.13, the charged-particle multiplicity dependence of the femtoscopic radii was observed to be a universal trend for the measurements at all collision energies. The ALICE result deviates from this universal scaling behaviour for the out and side direction because of modifications of the freeze-out shape [93]. A similar scaling behaviour is observed by the ALICE collaboration also in pp and p-Pb collisions [94]

but with significantly different parameters. A detailed discussion of the techniques and the theoretical background of femtoscopy in heavy-ion collisions can be found in [83].

By fixing the source function to the one observed in different femtoscopic studies, e.g. pion femtoscopy, other particle correlations can be used to investigate elastic interactions between the particles, e.g. for pΞ^-. The first observation of an attractive strong interaction between the

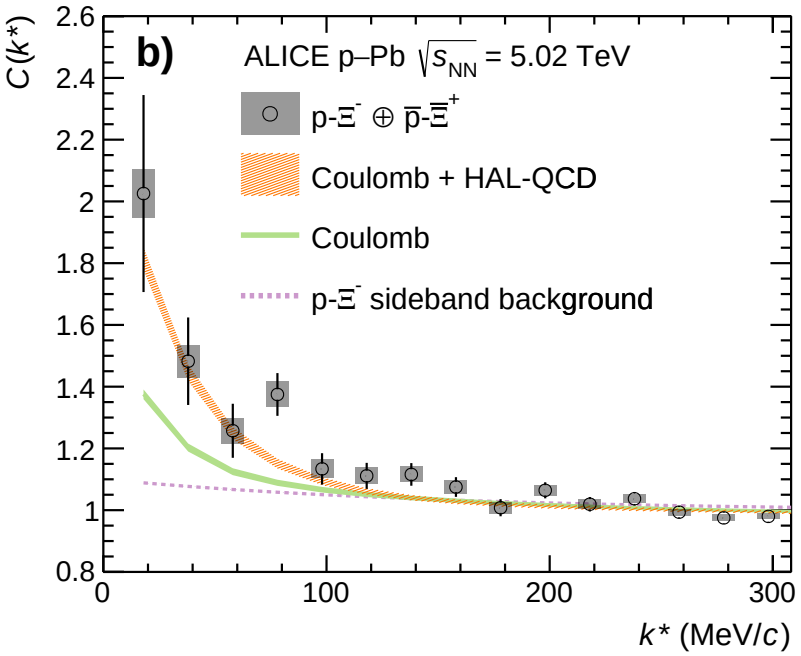

Figure 1.14: The correlation functions of p$-\Xi^-$ as a function of k^* [95] is compared to the expectations for Coulomb-only interactions and Coulomb plus an additional attractive strong interaction provided by the HAL-QCD collaboration [96]. Statistical and systematic uncertainties are indicated by vertical bars and boxes, respectively. The contribution from misidentified p$-\Xi^-$-pairs is estimated via a sideband analysis and shown as dashed line.

proton and Ξ^-, a multi-strange baryon, has been reported by the ALICE collaboration [95]. Figure 1.14 clearly shows that the measured correlation function deviates from the expectation taking only Coulomb interaction into account which indicates the presence of an additional attractive strong interaction. The measured correlation function is found to be consistent with the expectation calculated employing lattice QCD by the HAL-QCD collaboration [96] and constrains the modeling of neutron stars containing hyperons to stiffer equations of state. A hyperon is baryon containing one or more strange quark but no charm, beauty or top quark.

2. Light nuclei in ultra-relativistic ion collisions

The production mechanism of primary light (anti-)nuclei and (anti-)hypernuclei, i.e. (anti-) nuclei containing at least one (anti-)hyperon, in ultra-relativistic ion collisions is one of the open puzzles in high-energy physics. It cannot be calculated from first principles in QCD and, thus, two different classes of phenomenological models are often employed. On the one hand, the statistical hadronization model (SHM) describes particle yields, including the yields of light nuclei, over a wide range of energies in AA collisions [97, 46]. SHM fits to the abundances of different particle species measured in the same data set allow to extract the properties of the medium at the moment when the particle abundances are fixed, i.e. at the chemical freeze-out.

In heavy-ion collisions, the grand canonical formulation of the statistical hadronization model is commonly used, which is very successful in describing the measured yields of hadrons and nuclei. Figure 2.1 shows the comparison between three different implementation of the SHM, i.e. the GSI-Heidelberg model [46], THERMUS [98], and Statistical Hadronization with Resonances (SHARE) [99], and the integrated yields for different hadron species measured in 0–10% central Pb–Pb at $\sqrt{s_{\mathrm{NN}}} = 5.02$ TeV by ALICE. For all model fits, the baryochemical potential, which expresses the imbalance between matter and antimatter, was set to zero. This assumes a perfect balance which is indicated by the yield ratios of particles and antiparticles which are consistent with unity at the LHC. A good overall agreement covering many orders of magnitude is observed with a chemical freeze-out temperature of $T_{\mathrm{chem}} = 152 \pm 2$ MeV which is slightly lower than the values of $T_{\mathrm{chem}} = 156.5 \pm 1.5$ MeV found in Pb–Pb collisions at $\sqrt{s_{\mathrm{NN}}} = 2.76$ TeV [46]. In a recent publication [100], the deviation of the theoretical description from the measured proton yield in Pb–Pb collisions at $\sqrt{s_{\mathrm{NN}}} = 2.76$ TeV by about 2.7 standard deviations was resolved by considering resonant and non-resonant πN and $\pi\pi$N interactions. For the theoretical description of the measured particle yields in smaller systems, the grand canonical ensemble implementation of the SHM has to be changed to the canonical statistical hadronization model (CSM). In the canonical

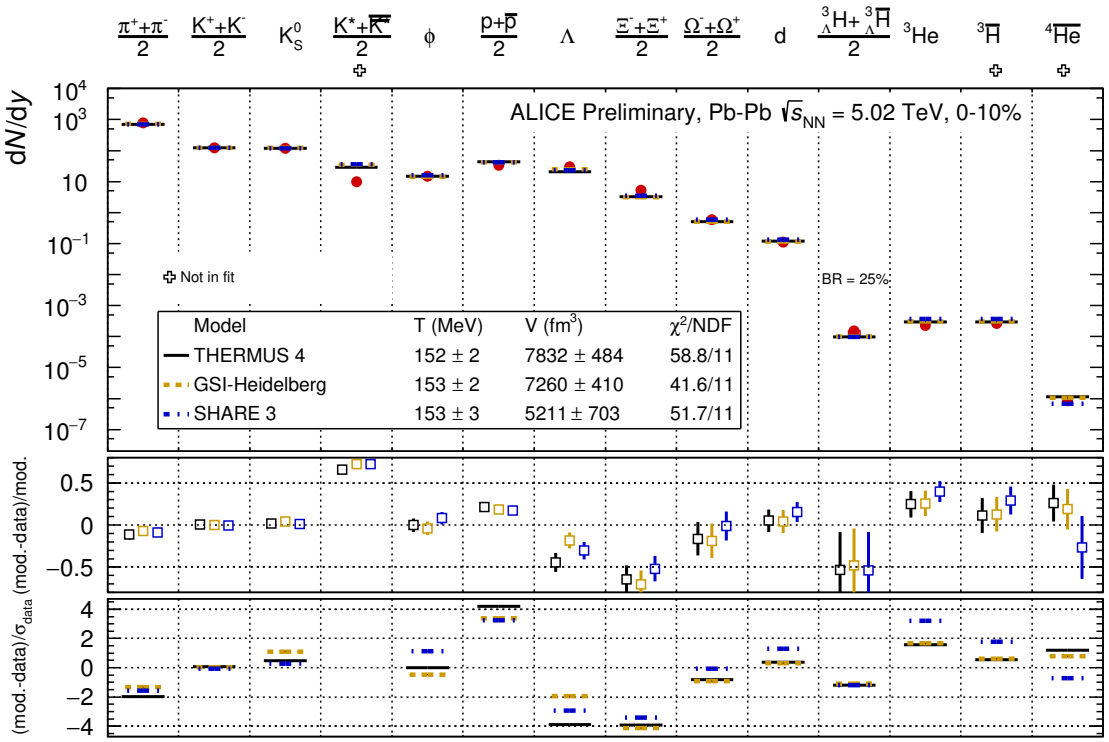

Figure 2.1: Abundances dN/dy for different hadron species, which were measured at midrapidity with ALICE in 0–10% central Pb–Pb collisions at $\sqrt{s_{\mathrm{NN}}} = 5.02$ TeV, are compared to the expectations from three different statistical hadronization model implementations [46, 98, 99]. The temperature and volume corresponding to the best fit result are listed in a table shown in the upper most panel. The mid panel shows the relative difference between the model expectation and the measurement compared to the model expectation, while the lower panel reports the same difference in terms of the uncertainty on the measured abundances.

ensemble version, the exact conservation of charges, like the baryon and strangeness number, within a correlation volume V_{c} is taken into account [101], while for the grand canonical description these charges are only conserved on average. A more detailed discussion of the statistical hadronization model will be given in section 2.1. Despite the good agreement of the SHM model prediction with the measured yield of light (anti-)nuclei, it is hard to understand how light nuclei, which have separation energies in the order of at most a few MeV, remain bound during the hadronic phase with temperatures between $T_{\mathrm{chem}} = 156.5 \pm 1.5$ MeV and $T_{\mathrm{kin}} = 89 - 164$ MeV [76]. One possible explanation could be that disintegration and regeneration of light (hyper-)nuclei and their antiparticles compensate each other and the overall number of (anti-)nuclei remains constant during the hadronic phase. This approach was recently discussed within the framework of the Saha equation [102], making use of the analogy

between the Big Bang and heavy-ion collisions at the LHC. A similar strategy was employed in [103], where a hybrid model was used to study the deuteron production at the LHC. In this hybrid model, a relativistic hydrodynamic description is used for the evolution of the QGP until chemical freeze-out at $T_{\mathrm{chem}} = 155$ MeV. For the further description of the medium produced in the collision a non-equilibrium hadronic transport model [104] was used. The authors claim that $\pi\mathrm{d} \leftrightarrow \pi\mathrm{pn}$ reactions after the chemical freeze-out lead to deuteron yields close to that expected from the SHM in Pb–Pb collisions no matter if deuterons are produced at the end of the QGP phase or not. A more speculative approach is that (hyper-)nuclei and their antiparticles are produced as compact, colorless droplets of quark matter with quantum numbers of the final state hadrons [46]. Unfortunately, no predictions employing this idea are available until now.

On the other hand, the coalescence of protons and neutrons, which are close by in phase space, has been proposed as production mechanism of light (anti-)nuclei [105]. This process is typically quantified based on the coalescence parameter B_A which is linked to the coalescence probability to produce a nucleus of mass number A. It is defined via

$$E_A \frac{\mathrm{d}^3 N_A}{\mathrm{d}p_A^3} = B_A \left(E_{\mathrm{p}} \frac{\mathrm{d}^3 N_{\mathrm{p}}}{\mathrm{d}p_{\mathrm{p}}^3} \right)^A \Bigg|_{\vec{p}_{\mathrm{p}} = \frac{\vec{p}_A}{A}} \tag{2.1}$$

where $E_i \mathrm{d}^3 N_i / \mathrm{d}p_i^3$ with $i = A$, p are the invariant yields of the nucleus and the proton, respectively. The coalescence parameter can be calculated from the overlap of the Wigner function of the nucleus and the phase-space distributions of its constituents [106, 107].

Both the thermal-statistical and the coalescence approach result in similar predictions [109]. As presented in Figure 2.2, recent studies [106] suggest a sizeable difference between the statistical and the coalescence model expectations for the coalescence parameter as a function of the mean charged-particle multiplicity density at midrapidity, $\langle \mathrm{d}N_{\mathrm{ch}}/\mathrm{d}\eta_{\mathrm{lab}} \rangle$, for ^{3}He and even more significantly for $^3_\Lambda$H. Previous measurements in pp [110] and Pb–Pb [111] collisions by ALICE have shown a trend towards a more coalescence like B_3 for low mean charged-particle multiplicity densities, while it approaches a more thermal behaviour at larger $\langle \mathrm{d}N_{\mathrm{ch}}/\mathrm{d}\eta_{\mathrm{lab}} \rangle$. The transition seems to take place at $\langle \mathrm{d}N_{\mathrm{ch}}/\mathrm{d}\eta_{\mathrm{lab}} \rangle$ accessible in p–Pb or peripheral Pb–Pb collisions.

The measurement of nuclei in pp and p–Pb collision also contribute significantly to the indirect searches for segregated primordial antimatter and dark matter via satellite-borne instruments, such as AMS-02 [112]. These experiments search for excesses in the measured antinuclei yields above the secondary antinuclei background from pp and p–A collisions in

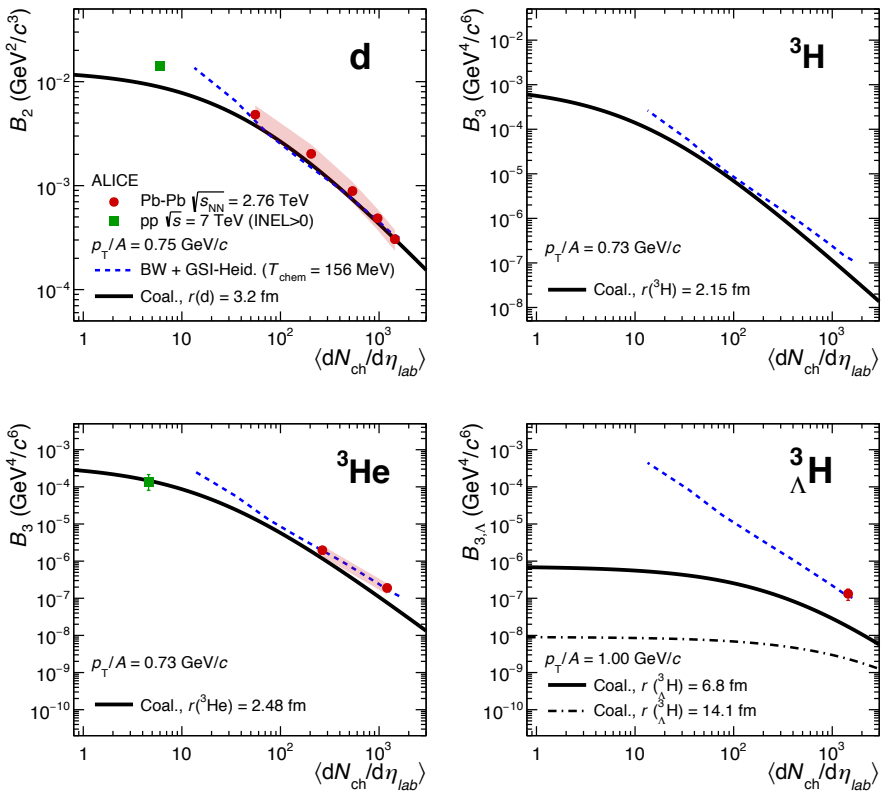

Figure 2.2: The expectations for the coalescence parameters for deuterons (upper left panel), ^{3}H (upper right panel), ^{3}He (lower left panel), and $^3_\Lambda$H (lower right panel) from the coalescence approach and a combination of the GSI-Heidelberg SHM with the Blast-Wave model are shown as a function of the mean charged-particle multiplicity density [106, 108]. The dashed-dotted line in the lower right panel corresponds to the coalescence prediction for $^3_\Lambda$H with a larger radius. In addition, the available measurements in pp and Pb–Pb collisions by ALICE are added for comparison. This figure is taken from [108].

the interstellar medium which can be predicted using the coalescence parameter measured at the LHC.

The particle production in heavy-ion collisions can be separated into two different contributions. Primary particles are produced in the collision itself and are of interest in most analyses. In addition, particles can be produced in decays of heavier particles and via interactions with the beam pipe and the detector material. These particles are called secondary particles. For nuclei, the main source of secondary nuclei is the production in spallation reactions of primary particles with the detector material which leads to the ejection of fragments as discussed in section 2.3. In addition, secondary (anti-)nuclei can be produced by the weak decay of heavier (anti-)(hyper-)nuclei, e.g. the decay of (anti-)hypertriton produces deuterons, ^{3}H and ^{3}He.

2.1. Statistical hadronization models

The Statistical Hadronization Model, also called thermal model, is based on the assumption that the QCD interactions give rise to the formation of extended massive object called cluster or fireball which decays into hadrons in a statistical way when the system reaches a critical energy density. The description is based on the statistical concept developed by Fermi [113] in the year 1950. Fermi postulated that all available phase-space states are occupied by particles produced from an excited region. This translates into one of the core assumptions of the SHM:

All multihadronic states within the cluster volume and compatible with its quantum numbers are equally likely [114].

Thus, the SHM can be interpreted as an effective model describing the decay of relativistic extended massive hadronic objects, like quark bags, which is an idea introduced by Hagedorn [115]. In the statistical bootstrap model, he introduced the idea that the fireballs as well as resonances are nothing else than excited hadrons leading to the bootstrap condition, "fireballs consist of fireballs, which consist of fireballs, which ...".

One difficulty of the SHM is that the localized states within the cluster are equally likely but they are in general different from the asymptotic states which can be observed in the experiment. This effect is negligible if the volume of the cluster is large and, thus, it can be neglected in most canonical and grand canonical applications because the volume of the medium is large compared to the Compton wavelength of the hadrons. However, it leads to difficulties for small cluster volumes and fundamental descriptions following the micro-canonical ensemble approach[1].

Towards the (microcanonical) partition function

The probability to observe an asymptotic multiparticle state $|f\rangle$ is given by

$$p_f \propto \sum_{h_V} |\langle f|\mathbf{P}_i|h_V\rangle|^2 = \sum_{h_V} \langle f|\mathbf{P}_i|h_V\rangle\langle h_V|\mathbf{P}_i|f\rangle = \langle f|\mathbf{P}_i\mathbf{P}_V\mathbf{P}_i|f\rangle\,, \tag{2.2}$$

[1] The micro-canonical ensemble describes an isolated system while the canonical and grand canonical description allows the exchange of energy between the system and a heat reservoir. In the grand canonical case, also particles can be exchanged which leads to the introduction of chemical potentials ensuring the conservation of quantum numbers, like baryon number and strangeness, on average. The chemical potential of a given state quantifies the change of the inner energy of system when the number of particles in the given state is changed.

where $\mathbf{P}_i$ and $\mathbf{P}_V$ are projectors onto the internal quantum numbers as well as the conserved quantities of the fireball and the localized states $|h_V\rangle$, respectively. The projector $\mathbf{P}_i$ can be factorized into a kinetic part and the projection onto inner symmetries

$$\mathbf{P}_i = \mathbf{P}_{P,J,\lambda,\pi}\mathbf{P}_\chi\mathbf{P}_{I,I_3}\mathbf{P}_\mathbf{Q}. \tag{2.3}$$

The kinetic part includes the conservation of energy and momentum P, as well as the spin J, the helicity λ and the parity π. The inner symmetries, taken care by the second part of the projector, are the abelian charges $\mathbf{Q}$, like baryon number, strangeness and electrical charge, the C-parity χ, the isospin I and its third component I_3. The projector part for the C-parity is only necessary for neutral systems, i.e. $I = 0$ and $\mathbf{Q} = 0$.

By summing over all final states, this leads to the microcanonical partition function Ω

$$\sum_f p_f \propto \sum_{f,h_V} \langle f|\mathbf{P}_i|h_V\rangle\langle h_V|\mathbf{P}_i|f\rangle = \sum_{h_V}\langle h_V|\mathbf{P}_i\sum_f|f\rangle\langle f|\mathbf{P}_i|h_V\rangle \tag{2.4}$$

$$= \sum_{h_V}\langle h_V|\mathbf{P}_i^2|h_V\rangle = a\sum_{h_V}\langle h_V|\mathbf{P}_i|h_V\rangle = a\,\Omega. \tag{2.5}$$

Here, there completeness of the final states, $\sum_f |f\rangle\langle f| = \mathbb{1}$, and $\mathbf{P}_i^2 = a\mathbf{P}_i$ with $a \geq 0$ is used. The interactions of the particles are taken into account via the Dashen–Ma–Bernstein theorem [116] by including all hadronic resonances as free particles with a mass distributed following a relativistic Breit-Wigner parametrization. Thus, the medium described is a hadron-resonance gas. A more detailed description of the basic formulation of the SHM can be found in [117].

Grand canonical ensemble approach

In the field of heavy-ion physics, the statistical hadronization model calculations usually ignore the conservation of the angular momentum, isospin, parity and C-parity. Thus, only the conservation of energy, momentum and the abelian charges are taken into account. As a consequence, $\mathbf{P}_i$ can be expressed as

$$\mathbf{P}_i = \delta(P_0 - \hat{H})\delta(\mathbf{Q}_0 - \hat{\mathbf{Q}}), \tag{2.6}$$

where P_0 and $\mathbf{Q}_0$ are the initial energy, momentum and abelian charged of the fireball, while $\hat{H}$ and $\hat{\mathbf{Q}}$ are the Hamilton and charge operators, respectively.

In addition, most applications use the grand canonical formulation of the SHM because the produced fireball is expected to be sufficiently large. This is possible since the experiments measure only particles from a small fraction of the system, e.g. ALICE measures the

midrapidity region with its central detectors. The investigated part of the phase space is in equilibrium with the remaining medium which acts as a thermal reservoir. Thus, the relevant quantum numbers as well as the energy and momentum have to be only conserved on average. The partition function is given by

$$Z(T,V,\mu) = \sum_{h_V} \langle h_V | \exp(-\beta(\hat{H} - \mu\hat{Q})) | h_V \rangle , \tag{2.7}$$

with the inverse temperature $\beta = 1/T$, volume V and the chemical potential μ. It can be written as the product of the partition functions of all hadron and resonance species. The multiplicity density of a given hadron species j can be calculated as

$$n_j^{\mathrm{th}}(T,V,\mu) = -\frac{T}{V}\frac{\partial \ln Z_j}{\partial \mu} = \frac{g_j}{2\pi^2}\int_0^\infty \frac{p^2 \mathrm{d}p}{\exp(\beta E_j)\lambda_j^{-1} \pm 1}, \tag{2.8}$$

where $g_j = 2J_j + 1$ is the spin and isospin degeneracy factor. $E_j = \sqrt{p^2 + m_j^2}$ and p denote the energy and momentum of one particle of the species. For fermions, the version with the plus sign (Fermi-Dirac statistics) has to be used while for bosons the one with minus sign is the correct equation (Bose-Einstein statistics). The fugacity λ_j of the particle species j is given by $\lambda_j(T,\mu) = \exp[\beta(\mu_B B_j + \mu_S S_j + \mu_Q Q_j)]$ and depends on the charges taken into account, here only electrical charge, baryon number and strangeness. In most of the calculations, this lead to five parameters: the temperature T, the volume V and three chemical potentials (μ_B, μ_S and μ_Q). Due to the initial collision conditions, two of the chemical potentials are constrained because the initial net strangeness is known and the charge conservation is linked to the isospin balance [118]. To compare the prediction of the SHM with measurements, the feed-down from strong resonance decays has to be added to the particle densities obtained with Equation 2.8. In some models, an additional factor γ_s is used to account for the possibility of incomplete strangeness equilibration. It is introduced by multiplying the partition function of each species with $\gamma_s^{S_j}$ where S_j is the number of valence strange and antistrange quarks.

Canonical ensemble approach

For smaller systems, like p–Pb, pp and $\mathrm{e}^+\mathrm{e}^-$, the exact conservation of the quantum numbers across the correlation volume V_c has to be taken into account since the abundance of hadrons with a given quantum number is small. Thus, the canonical ensemble version of the SHM has to be used. In this approach, the mean multiplicity density of hadron species j is given by

$$\langle n_j^{\mathrm{th}} \rangle^{\mathrm{ce}} = \frac{Z(B - B_j, Q - Q_j, S - S_j)}{Z(B, Q, S)} \langle n_j^{\mathrm{th}} \rangle^{\mathrm{gce}}, \tag{2.9}$$

where $\langle n_j^{\mathrm{th}} \rangle^{\mathrm{gce}}$ is the mean multiplicity calculated in the grand canonical ensemble and the canonical ensemble version of the hadron resonance gas partition function is expressed as $Z(B,Q,S)$. A more detailed description can be found in [101, 119, 120] and references therein.

This treatment leads to a suppression of the yields of particles carrying the exactly conserved charge compared to the grand canonical result which is denoted as "canonical suppression". This leads to a system size dependence of the particle yields which is also observed in experimental results for the (anti-)nuclei production as shown in Figure 2.3. In this figure the deuteron-to-proton yield ratio in pp, p–Pb and Pb–Pb collisions at different collision energies is reported in comparison to the expectations from the canonical statistical hadronization model, Thermal-FIST [101], and the coalescence approach [121], which will be discussed in more detail in section 2.2. For large system sizes, the canonical ensemble description converges towards the grand canonical result. The Thermal-FIST results are obtained from a simplified version of the canonical statistical hadronization model where the chemical freeze-out temperature is assumed to be constant as a function of the system size. This model has difficulties in describing yield ratios of hadrons, like protons and kaons, to pions. In addition, the behaviour predicted for the ϕ/π ratio is opposite to the measured one. The agreement between the hadron-to-pion ratios can be improved by involving a system size dependent chemical freeze-out temperature and a strangeness undersaturation factor γ_S [123]. Nevertheless, one can hope that further developments of the model will lead to a more consistent description of all the measurements at the LHC in the near future. Since the availability of canonical statistical model expectations for the comparison to the light nuclei results obtained at the LHC is a rather new development, the theoretical predictions are only available for the simplified version of Thermal-FIST model. These are used for the comparison to the results discussed in chapter 5.

2.2. Coalescence models

The coalescence approach describes the formation of nuclei in ion collisions by nucleons which are close to each other in phase space and thus form a bound state at the kinetic freeze-out. These models can provide information about the nuclei yields as a function of their momentum depending on the production spectra of the constituent nucleons. The coalescence

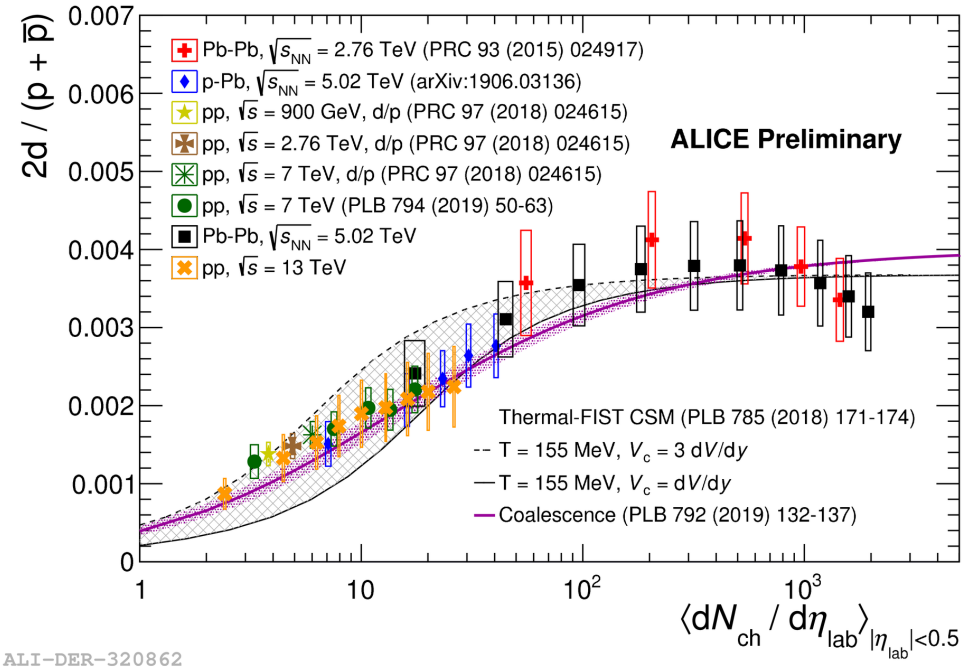

Figure 2.3: The deuteron-to-proton yield ratios in pp, p–Pb and Pb–Pb collisions at different collision energies are shown as a function of the mean charged-particle multiplicity density at midrapidity [122]. The expectations for the canonical statistical hadronization model, Thermal-FIST [101], and the coalescence approaches [121] are shown. For the thermal model, two different values of the correlation volume are displayed. The uncertainties of the coalescence calculations, which are due to the theoretical uncertainties on the emission source radius, are denoted as shaded bands.

parameter B_A is used to quantify the coalescence probability to produce a nucleus of mass number A and is defined via

$$E_A \frac{\mathrm{d}^3 N_A}{\mathrm{d}p_A^3} = B_A \left(E_\mathrm{n} \frac{\mathrm{d}^3 N_\mathrm{n}}{\mathrm{d}p_\mathrm{n}^3} \right)^{(A-Z)} \Bigg|_{\vec{p}_\mathrm{n}=\frac{\vec{p}_A}{A}} \left(E_\mathrm{p} \frac{\mathrm{d}^3 N_\mathrm{p}}{\mathrm{d}p_\mathrm{p}^3} \right)^{Z} \Bigg|_{\vec{p}_\mathrm{p}=\frac{\vec{p}_A}{A}}$$
$$\approx B_A \left(E_\mathrm{p} \frac{\mathrm{d}^3 N_\mathrm{p}}{\mathrm{d}p_\mathrm{p}^3} \right)^{A} \Bigg|_{\vec{p}_\mathrm{p}=\frac{\vec{p}_A}{A}} \tag{2.10}$$

where $E_i \frac{\mathrm{d}^3 N_i}{\mathrm{d}p_i^3}$ with $i = A$, p, n are the invariant yields of the nucleus, the proton and the neutron, respectively. The produced nuclei with mass number $A = Z + N$ are composed of Z protons and N neutrons. At the energies reached at the Large Hadron Collider (LHC), protons and neutrons are expected to be produced in equal amounts at midrapidity and, due to their

similar masses, their spectra are assumed to be identical. This allows for the simplification shown in Equation 2.10.

Simple coalescence

The simplest ansatz to calculate the coalescence parameter is to neglect the spatial part of the coalescence requirements and to focus only the momentum of the particles involved. Thus, nucleons with a momentum difference smaller than a maximum value, p_0, and which are in the correct spin state will coalesce into a nucleus. The parameter p_0 is not further specified by the theory and has to be obtained by comparison to experimental data. A detailed discussion of this approach, as well as further steps towards a more realistic result can be found in [105].

The relativistically invariant momentum space density of a particle with Lorentz factor γ before the coalescence process is given by

$$\rho = \gamma \frac{\mathrm{d}^3 N}{\mathrm{d}p^3}. \tag{2.11}$$

Thus, the probability for a nucleon to be inside a sphere in the momentum space centred around a given momentum $\vec{p}$ with radius p_0 can be expressed in the following form:

$$P = \frac{1}{M} \frac{4\pi}{3} p_0^3 \rho, \tag{2.12}$$

where M is the mean nucleon multiplicity. Using Equation 2.12, the probability to find A nucleons in the sphere is given by

$$P_M(A) = \binom{M}{A} P^A (1-P)^{M-A}. \tag{2.13}$$

Assuming that all nucleons which are close enough in momentum form a nucleus, this probability should be equal to the probability to find the nucleus with an atomic number A in the sphere. Taken into account that many nucleons ($M \gg 1$) are produced in a collision and that the production of a nucleus is a rare process ($PM \ll 1$), $(1-P)^{M-A}$ becomes approximately unity and $\frac{1}{M^A}\binom{M}{A} \approx \frac{1}{A!}$.

$$\frac{4\pi}{3}p_0^3\,\gamma_A\frac{\mathrm{d}^3N_A}{\mathrm{d}p^3} = \frac{1}{A!}\left(\frac{4\pi}{3}p_0^3\right)^A\left(\gamma_\mathrm{p}\frac{\mathrm{d}^3N_\mathrm{p}}{\mathrm{d}p^3}\right)^A$$
$$\gamma_A\frac{\mathrm{d}^3N_A}{\mathrm{d}p_A^3} = \frac{1}{A^3}\left(\frac{4\pi}{3}p_0^3\right)^{A-1}\frac{1}{A!}\left(\gamma_\mathrm{p}\frac{\mathrm{d}^3N_\mathrm{p}}{\mathrm{d}p^3}\right)^A \tag{2.14}$$

The additional factor $1/A^3$ comes from changing from the momentum p of the nucleons to the momentum $p_A = Ap$ of the nucleus on the left side of the equation. Comparing the result to Equation 2.10 using $\gamma = \frac{E}{m}$, the coalescence parameter can be identified as

$$B_A = \frac{1}{A^3}\frac{1}{A!}\left(\frac{4\pi}{3}p_0^3\right)^{A-1}\frac{M_A}{m^A}, \tag{2.15}$$

with the nucleon mass m and the nucleus mass M_A. To take the spin of the nucleons and the resulting nucleus into account, the spin factor, $(2J_A+1)/2^A$, has to be inserted into the equation

$$B_A = \frac{2J_A+1}{2^A}\frac{1}{A^3}\frac{1}{A!}\left(\frac{4\pi}{3}p_0^3\right)^{A-1}\frac{M_A}{m^A}, \tag{2.16}$$

Following this simplified approach, the coalescence parameter is independent of the transverse momentum as well as the size of the emitting source and the produced nucleus. This type of coalescence parameter is not compatible with the transverse momentum and centrality dependence observed in Pb–Pb collisions with ALICE at the LHC [111] as shown in Figure 2.4.

Advanced coalescence

For a more realistic ansatz to derive the coalescence parameter, the size of the emission source and of the produced nucleus should be taken into account. In this section, only the basic steps of such a derivation of B_A are presented. A full discussion can be found in [124].

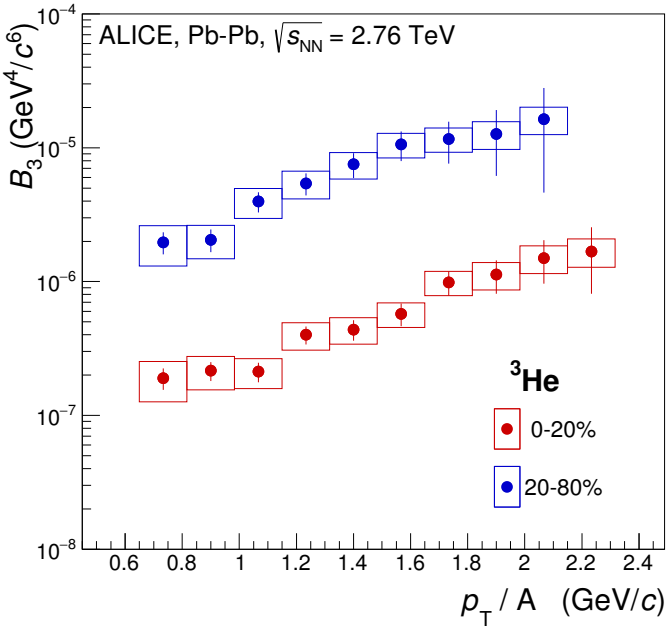

Figure 2.4: The coalescence parameter B_3 for ^{3}He as a function of the transverse momentum per nucleon measured by ALICE in 0-20% and 20-80% central Pb–Pb events at $\sqrt{s_{\mathrm{NN}}} = 2.76$ TeV [111].

First, the nuclei are treated as point-like particles produced by thermal emission from an expanding source. The invariant yield of nuclei with a mass number A and spin J_A is thus given by the (generalized) Cooper-Frye formula [125]

$$E_A \frac{\mathrm{d}^3 N_A}{\mathrm{d}p_A^3} = \frac{2J_A+1}{(2\pi)^3} \int_{\Sigma_f} p_A^\mu \, \mathrm{d}^3\sigma_\mu(R) \, f_p^Z(R, p_A/A) \, f_n^N(R, p_A/A)$$
$$\text{with } f_i(R,p) = \left[\exp\left(\frac{p \cdot u(R) - \mu_i(R)}{T(R)} \right) \pm 1 \right]^{-1}, \tag{2.17}$$

where Σ_f is the freeze-out hypersurface with a normal 4-vector $\mathrm{d}^3\sigma_\mu(R)$. The 4-momentum of the nucleus is denotes as p_A^μ, while the local flow 4-velocity at a point R is expressed as $u^\mu(R)$. For nucleons and nuclei, the (local) chemical potential, $\mu_i(R)$, is much smaller than the mass and the local equilibrium distributions f_i can be approximated by a local Boltzmann distribution. In addition, a simultaneous freeze-out at a constant temperature $T(R) = T$ and local chemical equilibrium among the different particle species is assumed. This simplifies the local equilibrium distributions f_i to

$$f_i(R,p) = \exp\left(\frac{\mu_i}{T}\right) \exp\left(\frac{-p \cdot u(R)}{T}\right) H(R), \tag{2.18}$$

with a common density profile $H(R)$. The chemical potential of the nucleus is defined as $\mu_A = Z\,\mu_\mathrm{p} + N\,\mu_\mathrm{n}$. The internal structure and the size of the nucleus is taken into account by adding a quantum-mechanical correction factor, $\langle C_A \rangle (p_A)$.

For this derivation, we consider only central collisions which are azimutally symmetric with respect to the beam axis. Thus, cylindrical coordinate, with $\rho = \sqrt{x^2 + y^2}$ and an azimuthal angle ϕ, are an appropriate choice. In addition, we use the longitudinal proper time $\tau = \sqrt{t^2 - z^2}$ and the longitudinal space-time rapidity $\eta = \mathrm{artanh}(z/t)$. After the integration of Equation 2.17 using the saddle point approximation [126] for the azimuthal component, the yields are given by

$$E_A \frac{\mathrm{d}^3 N_A}{\mathrm{d}p_A^3} \approx \frac{2J_A + 1}{(2\pi)^3} M_\mathrm{T} \langle C_A \rangle (p_A)\, V_\mathrm{eff}(A, M_\mathrm{T}) f(\mu_A, M, M_\mathrm{T})$$

$$\text{with } f(\mu_A, M, M_\mathrm{T}) = \exp\left(\frac{\mu_A - M}{T}\right) \exp\left(-\frac{M_\mathrm{T} - M}{T^*} - \frac{AY^2}{2(\Delta\eta)^2}\right) \tag{2.19}$$

$$\text{and } V_\mathrm{eff}(A, M_\mathrm{T}) = \frac{2\pi^{\frac{3}{2}} (\Delta\rho)^2 (\Delta\eta)\tau_0}{\left(\frac{M_\mathrm{T}}{T}\eta_f^2 + A\right)\sqrt{\frac{M_\mathrm{T}}{T}(\Delta\eta)^2 + A}}, \tag{2.20}$$

where Y is the rapidity of the nucleus and τ_0 is the fixed longitudinal proper time at which the freeze-out takes place. $\Delta\eta$ and $\Delta\rho$ are the widths of the Gaussian shape of the density profile $H(R)$ in the longitudinal and transverse direction, respectively. $T^* = T + \frac{M}{A}\eta_f^2$ is the effective temperature which is modified depending on the strength of the transverse flow η_f. $V_\mathrm{eff}(A, M_\mathrm{T})$ is the effective volume contributing to the emission of a particle with mass number A and a transverse mass $M_\mathrm{T} \approx A\, m_\mathrm{T}$ where m_T is the transverse mass of the coalescing nucleons. Thus, it can be expressed via the effective volume for the nucleons as

$$V_\mathrm{eff}(A, M_\mathrm{T}) \approx \frac{V_\mathrm{eff}(1, M_\mathrm{T})}{A^{\frac{3}{2}}}. \tag{2.21}$$

For the nucleons, the formula simplifies to

$$E_\mathrm{p} \frac{\mathrm{d}^3 N_\mathrm{p}}{\mathrm{d}p_\mathrm{p}^3} \approx \frac{2}{(2\pi)^3} M_\mathrm{T} V_\mathrm{eff}(1, M_\mathrm{T}) f(\mu, m, M_\mathrm{T}). \tag{2.22}$$

By inserting Equation 2.20 and Equation 2.22 into Equation 2.10, the coalescence parameter can be identified as

$$B_A = \frac{2J_A + 1}{2^A} A \langle C_A \rangle \frac{V_\mathrm{eff}(A, M_\mathrm{T})}{V_\mathrm{eff}(1, M_\mathrm{T})} \left(\frac{(2\pi)^3}{M_\mathrm{T} V_\mathrm{eff}(1, M_\mathrm{T})}\right)^{A-1}. \tag{2.23}$$

The effective volume can be linked to the homogeneity volume which is experimentally measurable via Hanbury Brown-Twiss (HBT) interferometry. In the Yano-Koonin-Podgoretskii (YKP) parametrization [127], the homogeneity volume is expressed in terms of the length $R_\perp$, R_0, and $R_\parallel$. The effective volume is given by

$$V_{\text{eff}}(1, M_{\text{T}}) = (2\pi)^{\frac{3}{2}} R_\parallel R_\perp^2 \tag{2.24}$$

The homogeneity volume is the space-time region inside which the particles show quantum statistical correlations because their momentum distributions vary sufficiently little [128]. Assuming $R_\parallel \approx R_\perp \approx R$, the coalescence parameter is thus given by

$$B_A = \frac{2J_A + 1}{2^A} \frac{1}{\sqrt{A}} \langle C_A \rangle \left(\frac{(2\pi)^{\frac{3}{2}}}{M_{\text{T}} R^3} \right)^{A-1} . \tag{2.25}$$

According to [106], the quantum-mechanical correction factor leads to a significant suppression in the production of nuclei with large radii compared to the source radius and can be expressed in the following way:

$$\langle C_A \rangle = \left(1 + \frac{r_A^2}{4R^2} \right)^{-\frac{3}{2}(A-1)} . \tag{2.26}$$

Therefore, the final result for the coalescence parameter taking the size of the nuclei r_A and the emitting source R into account is given by

$$B_A = \frac{2J_A + 1}{2^A} \frac{1}{\sqrt{A}} \frac{1}{m_{\text{T}}^{A-1}} \left(\frac{2\pi}{R^2 + (\frac{r_A}{2})^2} \right)^{\frac{3}{2}(A-1)} . \tag{2.27}$$

Thus, the coalescence parameter dependence not only on the size of the nuclei produced and the emitting medium but also directly and indirectly on the transverse momentum. The direct dependence is obviously due to the explicit m_{T}-dependence in Equation 2.27. Due to this, B_A would decrease with increasing p_{T} which is in contrast to the observation. In addition, the coalescence depends on the transverse momentum via the radius of the emitting source. The size of the source is found to be decreasing with p_{T} [92] and, thus, leads to an increasing trend for B_A with p_{T}.

2.3. Nuclei production via spallation

As already mentioned at the beginning of this section, secondary nuclei are produced via spallation reactions of particles produced in the collision and the detector material. These secondary nuclei are an important background for the study of nuclei production in collisions. The techniques to estimate and subtract this contribution from the measured abundances will be discussed in chapter 4, while in the following paragraphs, the theoretical description of the spallation process is described.

Even though the production of nuclei via spallation plays an important role in many different fields of physics, like cosmic ray and nuclear physics, it is not fully understood. In spallation reactions, a light projectile causes the emission of a large number of hadrons or fragments from a heavy nucleus in a complex process of particle interactions and deexcitations. The investigations performed in many years of spallation experiments have shown that the process can be separated into three parts, the intra-nuclear cascade, the pre-equilibrium particle emission and the evaporation or fission [129].

Intra-nuclear cascade

The first stage of the spallation process is the intra-nuclear cascade (INC) which is a fast process ($\approx 10^{-22}$ s). The incident particle, called projectile, is sharing its kinetic energy via elastic collisions and a series of nucleon–nucleon collisions. This process is often simulated based on either the Liège [130] or the Bertini/Isabel model [131]. In the Liège model, all particles are propagated freely until two of them reach the minimum relative distance d_{min}. If $d_{\mathrm{min}} \leq \sqrt{\sigma/\pi}$ with σ denoting the total cross section, the two particles are forced to scatter. The particles continue moving on straight lines after the interaction. In contrast, the Bertini/Isabel model treats the target as a continuous medium which provides a mean free path $\lambda = (\rho\sigma_{\mathrm{tot}})^{-1}$, which is proportional to the nuclear density ρ and the total interaction cross section of the projectile and the target. The projectile scatters after a path whose length is chosen randomly from an exponential distribution characterized by λ.

Pre-equilibrium particle emission

The pre-equilibrium particle emission stage is the least understood part of the spallation process. It takes place almost in parallel to the intra-nuclear cascade and gives rise to the emission of highly energetic nucleons or composite objects in the direction of the projectile. There are several models employed to describe this phase, like the exciton model [132, 133] or the surface-coalescence model [134]. The exciton model starts from the configuration at the

final stage of the intra-nuclear cascade and the system passes through sequence of single-particle excitation configurations, called excitons. The occurrence of configurations with a high enough level of excitation to escape from the nucleus is estimated in a statistical way. Following this original approach of the exciton model, the strongly forward peaked angular distribution measured in proton-induced spallation reactions cannot be reproduced [129]. In addition, the emission of light nuclei has to be treated either via exciton coalescence or pre-formed particles. The pre-equilibrium emissions in the surface-coalescence model can take place at any time during the intra-nuclear cascade. When a nucleon with sufficient energy hits the surface and is not reflected, a cluster can be emitted if the nucleon belongs to a set of nucleons which are sufficiently close in phase space. The condition when two nucleons are close enough is one of the model parameters. Another model parameter is linked to technical considerations due to the intra-nuclear cascade implementation. This is the distance at which the cluster condition is checked for fast nucleons in the outer fringes of the nucleus. The emission conditions are checked starting from the largest to the smallest cluster, e.g ^{4}He before ^{3}He or ^{3}H before the deuteron. Only clusters with a positive total energy, including the potential energy, the binding energy of the cluster and a positive kinetic energy, can be emitted if they are able to tunnel through the Coulomb barrier. The particles emitted in this stage of the spallation reaction can collide with other nuclei in the target and cause a hadronic cascade.

Evaporation or fission

In the last stage of the spallation process, the system has thermalized and the dissipated energy is released via evaporation of neutrons and light fragments at low energies, the fission of the excited nucleus and gamma ray emission. The emission from the last stage of the spallation reaction is isotropic. The evaporation is described as sequential particle emission based on statistical models either via the Hauser-Feshbach [135] or the Weisskopf-Ewing [136] formalism. The former strictly conserves the angular momentum and is thus computationally more expensive than the Weisskopf-Ewing formalism, which uses a treatment based on phase-space arguments. The evaporation process stops if the remaining energy is too low to allow for further evaporation or if fission is happening. The resulting fission products can undergo further evaporation processes depending on the initial excitation energy. The description of the nuclear fission process is based on the model developed by Niels Bohr and John Archibald Wheeler in 1939 [137] which makes use of the analogy to the division of a liquid drop into two smaller droplets as the result of a deformation caused by an external disturbance. The remaining energy is dissipated via gamma ray de-excitation.

2.4. Summary of the motivation

The production of light (anti-)nuclei in high-energy ion collisions is not yet fully understood. These processes cannot be calculated from first principles because they involve QCD interactions at non-perturbative scales. Therefore, phenomenological models are employed to predict the resulting light-nuclei yields, which usually belong to either the category of the statistical hadronization models (SHM) or models based on the coalescence approach. In these models, the nuclei are produced at different stages of the collision but no detailed (microscopic) descriptions of the underlying processes are given. A detailed discussion on the production of light nuclei in ultra-relativistic ion collisions can be found in chapter 2.

Studies of the production yields of light (anti-)nuclei in high-energy collisions, e.g. as a function of the size of the produced medium, and the transverse momentum of the nuclei, can provide information on the formation processes. The ALICE collaboration provided already numerous measurements of the production yields of deuterons in pp, p–Pb and Pb–Pb collisions at the LHC. As shown in Figure 2.3, these studies indicate a smooth evolution of the ratio of the production yields of deuterons and protons with the size of the system expressed via the mean charged-particle multiplicity density, $\langle \mathrm{d}N_{\mathrm{ch}}/\mathrm{d}\eta_{\mathrm{lab}} \rangle$, which is a related quantity as discussed in section 1.2.3. In addition, the experimental result are compared to the expectations from the coalescence [121] and the canonical statistical model [101] which are both in good agreement with the measurements. To gain further insight, the experimental results must be extended to other light (anti-)nuclei species.

The production of light nuclei is a rare process, especially in pp and p–Pb collisions. As a consequence only nuclei with mass number $A = 3$ are within reach using the data samples collected by the ALICE collaboration up to now. The ALICE collaboration has published results for the production of (anti-)^{3}He in pp and Pb–Pb collisions [111] as well as of (anti-)^{3}H in pp collisions [110]. To complement this picture, the corresponding production yields in p–Pb collisions are essential which would provide information about the system size region between pp and Pb–Pb collisions. This is clearly indicated in Figure 2.5 which summarizes the available measurements of the ^{3}He-to-proton yield ratio as a function of the charged-particle multiplicity density at midrapidity. These are compared to the expectations from the canonical statistical [101] and two different implementations of the coalescence model [121]. The latter take the size of the nuclei and the emitting medium into account. It is shown for the assumption of three- and two-body coalescence. In the former case, ^{3}He and ^{3}H are directly produced from protons and neutron which are close-by in phase space, while for two-body coalescence an intermediate formation of deuterons is needed. For both coalescence approaches, the the-

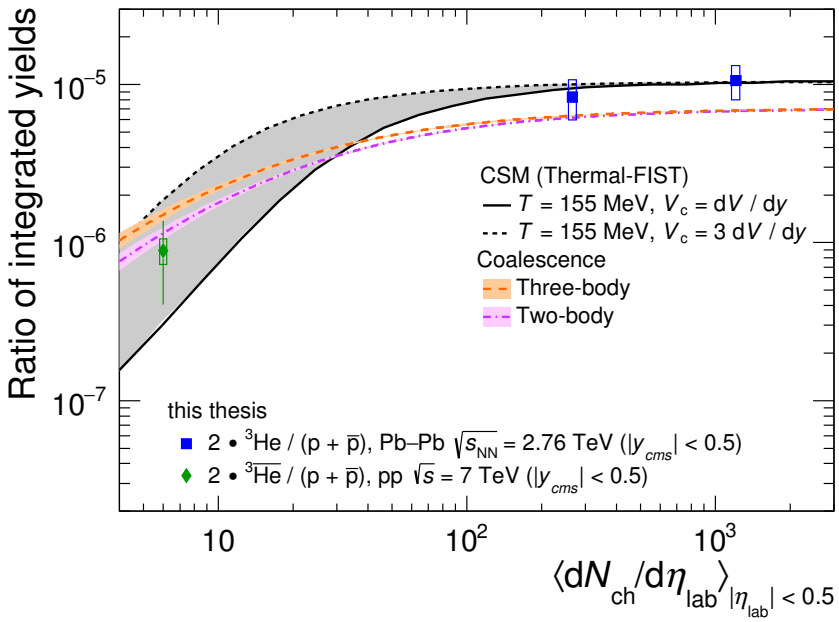

Figure 2.5: The ^{3}He-to-proton yield ratio in pp and Pb–Pb collisions [110, 111] are shown as a function of the mean charged-particle multiplicity density at midrapidity. Statistical and systematic uncertainties are indicated by vertical bars and boxes, respectively. Expectations from the canonical statistical hadronization model, Thermal-FIST [101], and the coalescence approach [121] are shown. For the thermal model, calculations with two different values of the correlation volume are displayed. The uncertainties of the coalescence calculations, which are due to the theoretical uncertainties on the emission source radius, are denoted as shaded bands.

oretical uncertainties are given by the uncertainty on the emission source radius. In addition, recent theoretical predictions show that these results could also provide the possibility to discriminate between the coalescence and the SHM descriptions as indicated in Figure 2.6 in which the coalescencce parameter B_3 is shown as a function of $\langle \mathrm{d}N_{\mathrm{ch}}/\mathrm{d}\eta_{\mathrm{lab}} \rangle$ for $p_{\mathrm{T}}/A = 0.73$ GeV/c. Two versions of the statistical hadronization model are shown, a grand canonical [97, 46] and a canonical implementation [101]. Since these models only predict the total yield, for both versions of the SHM an assumption for the transverse-momentum shape has to be made. In this case, a Blast-Wave parametrisation obtained from simultaneous fits to pion, kaon, and proton spectra measured in Pb–Pb collisions [138] is used. The resulting expectation for the coalescence parameter is compared to the available measurements in pp and Pb–Pb collisions published by ALICE. Even though the CSM curve is shown down to the range accessible in pp collisions, one has to be careful with direct comparisons because the corresponding (anti-)^{3}He

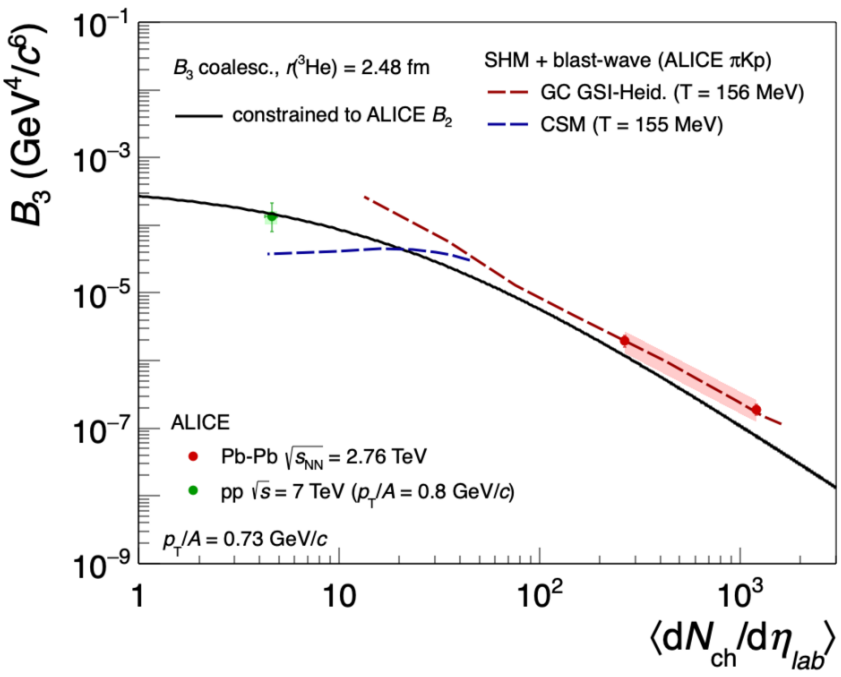

Figure 2.6: The expectations for the coalescence parameters for ^{3}He from the coalescence approach and a combination of two versions of the statistical hadronization model with the Blast-Wave model are shown as a function of the mean charged-particle multiplicity density. In addition, the available measurements in pp and Pb–Pb collisions by ALICE are added for comparison. This figure is taken from [108].

spectra are not very well compatible with the Blast-Wave parametrisation used for the theory curve.

Recent coalescence calculations have shown that the ratio of the coalescence parameters calculated with the yields of (anti-)^{3}H and (anti-)^{3}He, which they denotes as ρ, can provide a clear argument to support either the coalescence or the SHM description. This ratio is equal to the yield ratio of (anti-)^{3}H to (anti-)^{3}He assuming that the neutron spectrum is equal to the proton spectrum which is expected to be the case at LHC energies. As presented in Figure 2.7, the predictions for ρ from the coalescence and the statistical hadronization model increasingly differ with decreasing charged-particle multiplicity density. Since the size of the data set of p–Pb collisions collected by ALICE also allows for the measurement of the production yield of (anti-)^{3}H as a function of the transverse momentum, the yield ratio of (anti-)^{3}H to (anti-)^{3}He can be calculated for the first time with results obtained at the LHC.

The analysis strategy employed to obtain the p_{T}-differential production yields of (anti-)^{3}He and (anti-)^{3}H in p–Pb collisions at a center-of-mass energy per nucleon pair of 5.02 TeV are described in chapter 4 and the results are discussed in chapter 5.

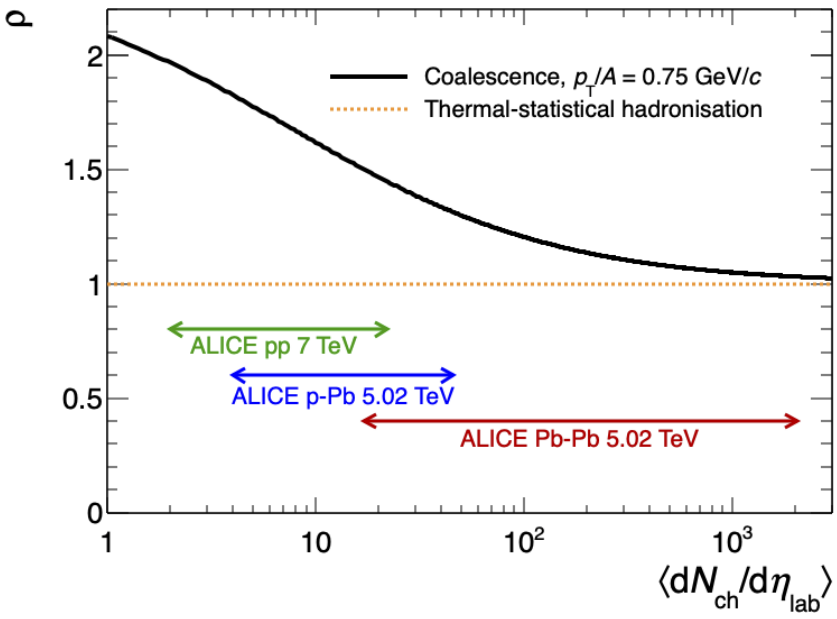

Figure 2.7: The expectations for the ratio of the (anti-)^{3}H to the (anti-)^{3}He production yield from the coalescence approach and the statistical hadronization model are shown as a function of the mean charged-particle multiplicity density. The colored arrows indicate the regions which can be accessed via measurements in pp, p–Pb and Pb–Pb collisions with ALICE at the LHC. This figure is taken from [106].

3. A Large Ion Collider Experiment at the Large Hadron Collider

3.1. The Large Hadron Collider

The Large Hadron Collider (LHC) [31] at CERN, the European Organisation for Nuclear Research close to Geneva, is currently the world's most powerful accelerator in terms of energy and luminosity[1]. It is a two-ring system with superconducting magnets which was installed in the existing tunnel with a circumference of 27 km constructed for the CERN Large Electron-Positron collider (LEP). The LHC was designed to provide proton-proton (pp) collisions with a centre-of-mass energy ($\sqrt{s}$) up to 14 TeV with a maximum luminosity, of $10^{34}\text{cm}^{-2}\text{s}^{-1}$. For ions, the center-of-mass energy, given per nucleon-nucleon pair ($\sqrt{s_{\text{NN}}}$), is reduced compared to protons due to the different ratio of the charge to the mass. It can be calculated as

$$\sqrt{s_{\text{NN}}} = \sqrt{Z_i/A_i}\sqrt{Z_k/A_k}\sqrt{s}, \tag{3.1}$$

where $\sqrt{s}$ is the centre-of-mass energy in the case of pp collisions and $\sqrt{Z_{i,k}/A_{i,k}}$ is the correction for the ions of type i and k contained in each of the beams. Thus, the top centre-of-mass energy for lead-lead (Pb–Pb) collisions is $\sqrt{s_{\text{NN}}} = 5.52$ TeV, while it is $\sqrt{s_{\text{NN}}} = 8.79$ TeV for proton-lead (p–Pb) collisions[2]. The maximum energy reached until now is $\sqrt{s} = 13$ TeV for pp collisions, $\sqrt{s_{\text{NN}}} = 8.16$ TeV, and $\sqrt{s_{\text{NN}}} = 5.02$ TeV for p–Pb and Pb–Pb, respectively. To reach these high energies, the protons and ions have to be accelerated to increasingly higher energies by a chain of pre-accelerators before being injected into the LHC. The full accelerator complex is sketched in Figure 3.1. The pre-accelerator chain for the LHC is composed of the Linear Accelerator 2 (LINAC2) plus the Proton Synchrotron Booster (BOOSTER) for protons and the Linear Accelerator 3 (LINAC3) plus the Low Energy Ion Ring (LEIR) for

[1] The luminosity ($\mathscr{L}$) is a measure of how many particles are sent through a given transverse area in a given time. It is thus linked to the interaction rate R via the cross section (σ) which quantifies the probability that a given process, here a collision, is taking place: $R = \mathscr{L}\sigma$

[2] For lead, the charge number is $Z = 82$ and mass number is $A = 208$.

ions. Afterwards both protons and ions are fed into the Proton Synchrotron (PS) and the Super Proton Synchrotron (SPS) before being injected into the LHC. The ions injected into the LHC are fully stripped, i.e. all electrons have been removed. The ions are emitted from the ion source in an only partially stripped status. During the pre-acceleration process, the remaining electrons are removed via two stripping stages, after the LINAC3 and the PS. A detailed description of the different stages of the acceleration can be found in [139].

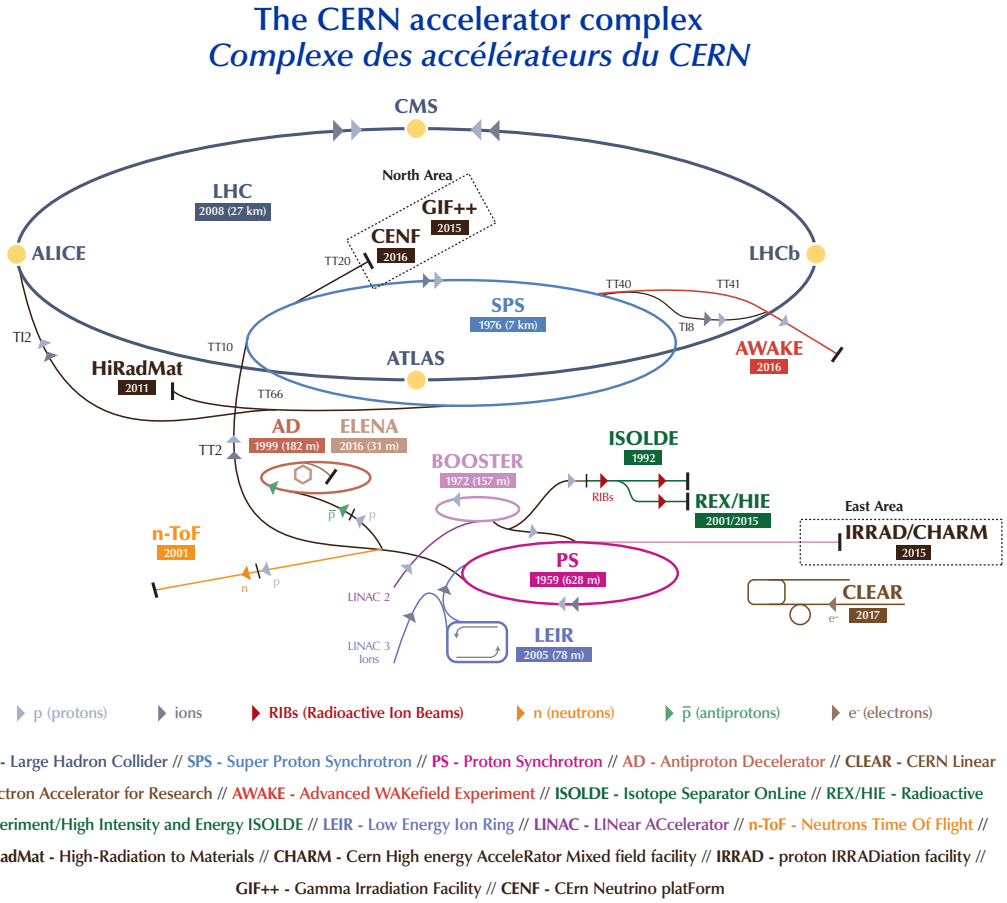

Figure 3.1: The CERN accelerator complex with all accelerators and experimental facilities is shown as published in 2018 [140]. The parts in which protons or ions are accelerated or transferred are indicated by the light and dark gray arrows, respectively.

Most of the LHC running time is dedicated to proton-proton (pp) collisions. Nevertheless, about one month per year of the physics program at the LHC is dedicated to the study of heavy-ion collisions.

The LHC ring contains eight straight sections in which either the experiments are placed or the beams are accelerated or tuned. These sections are named in a numerical fashion, Point

1-8. There are four large experiments (ALICE, ATLAS, CMS, LHCb) and three smaller ones (LHCf, TOTEM, MoEDAL) at the LHC.

A Toroidal LHC Apparatus (ATLAS) [141] and the Compact Muon Solenoid (CMS) [142] experiments are located at Point 1 and Point 5, respectively, where the highest luminosity can be delivered. Both experiments were designed to search for the Higgs boson and physics beyond the Standard Model as well as to perform high precision tests of QCD, electroweak interactions, and flavour physics in pp collisions. The total proton-proton cross section is measured by the Total Elastic and diffractive cross section Measurement (TOTEM) [143] collaboration with a luminosity-independent method. In addition, TOTEM studies the proton structure via elastic scattering with large momentum transfers. Even though TOTEM is technically integrated into the CMS apparatus, it is an independent experiment. The LHC-forward (LHCf) experiment [144] focuses on the measurement of the neutral particles emitted in the very forward region of the LHC collisions to calibrate the hadron interaction models used in extremely high energy cosmic-ray physics. Consequently, the LHCf detectors are located $\pm$140 m from interaction point 1.

The LHC-beauty (LHCb) experiment [145] is located at Point 8 and was optimized for precision measurements of CP violation and rare decays of hadrons containing charm and beauty quarks. At the same place, the Monopole and Exotics Detector at the LHC (MoEDAL) [146] is installed which searches for highly-ionizing avatars of new physics such as magnetic monopoles or massive (pseudo-)stable charged particles.

The only experiment designed primarily for the heavy-ion program at the LHC is A Large Ion Collider Experiment (ALICE) [147] which is located at Point 2. The main goal was to investigate the physics of strongly interacting matter and the quark-gluon plasma at extreme values of the energy density and temperature. Meanwhile, all four large experiments at the LHC have joined the heavy-ion program which indicates the growing interest in studies of heavy-ion collisions at the high energy frontier.

3.2. The ALICE detector

ALICE is a general-purpose heavy-ion detector with excellent tracking and particle-identification (PID) capabilities over a broad momentum range. It is designed to cope with the extreme charged-particle multiplicity density produced at midrapidity in central Pb–Pb collisions[3].

[3]The ALICE detector is optimized for a charged-particle multiplicity density at mid-rapidity of $\mathrm{d}N/\mathrm{d}\eta = 4000$ which was chosen based on extrapolations of measurements at RHIC. The ALICE collaboration has measured a mean charged-particle multiplicity density of 2035 ± 52 in 0–2.5% central Pb–Pb collisions at $\sqrt{s_{\mathrm{NN}}} = 5.02$ TeV [52]

Due to its low material budget, it is ideally suited for the measurement of light (anti-)nuclei production.

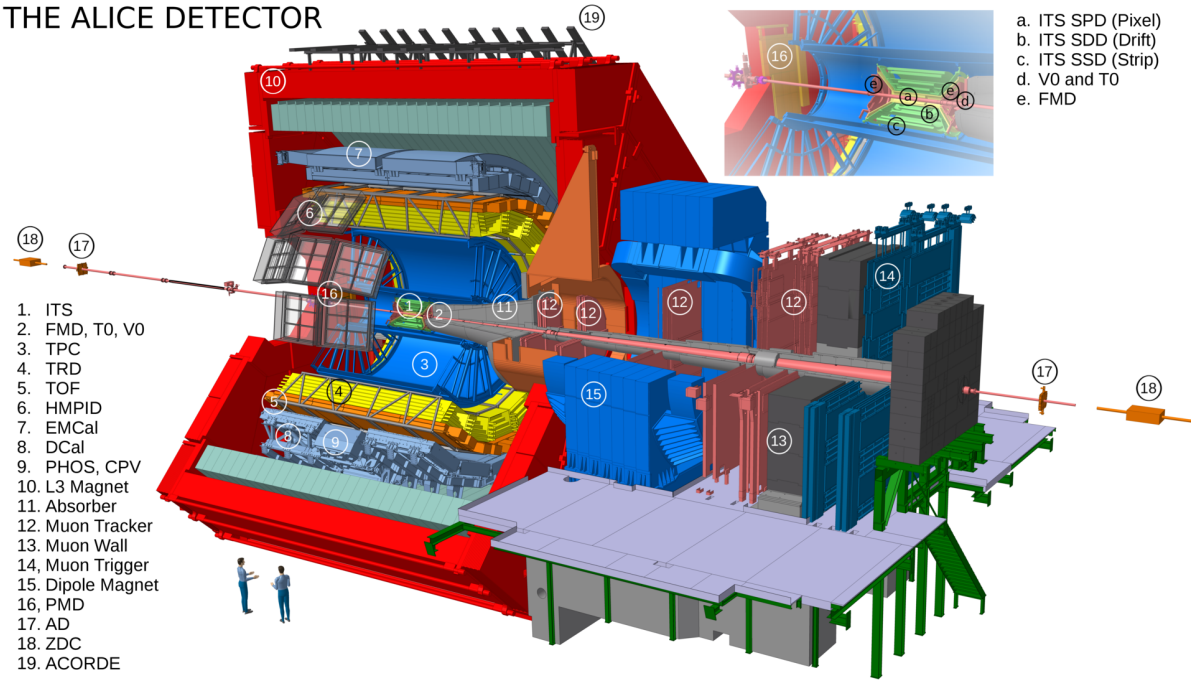

Figure 3.2: The ALICE apparatus [148] is composed of 18 different detectors which are indicated by their acronyms. The central barrel detectors (left side) are mounted inside the large solenoid magnet which had already been part of the L3 detector at LEP. The Muon spectrometer with its dipole magnet is placed in forward direction (right side). The innermost region, consisting of the Inner Tracking System, the forward trigger and the multiplicity detectors, is shown in more details on the top right position. This picture is taken from [149].

The standard coordinate system in ALICE is a right-handed Cartesian coordinate system where the origin is fixed to the interaction point. The x axis points to the centre of the LHC ring and the y axis is approximately vertical and points upwards. Consequently, the z axis is aligned to the beam direction and points in the direction opposite to the muon spectrometer. φ is the azimuthal angle and θ is the polar angle with respect to the beam axis. The polar angle is often expressed in terms of pseudorapidity η. The two quantities are linked via Equation 3.2.

$$\eta = \frac{1}{2}\ln\left(\frac{p+p_z}{p-p_z}\right) \equiv -\ln\left[\tan\left(\frac{\theta}{2}\right)\right] \tag{3.2}$$

The ALICE detector has an overall size of $16 \times 16 \times 26$ m^3 and a total weight of about 10 000 t and was optimized to cope with the high particle densities expected for heavy-ion collisions. It

can be divided into two parts: the central-barrel detectors and the forward muon spectrometer. In addition, an array of scintillators, ALICE Cosmic Ray Detector (ACORDE), in mounted on top of the L3 magnet to trigger on cosmic rays. For the global event characterization and for triggering five detectors (ZDC, PMD, FMD, T0, V0) are placed at large pseudorapidities. Within their limited acceptance, the Forward Multiplicity Detector (FMD), V0, and T0 are used to determine the number of particles produced in the collision and their spatial distribution. T0 is also used to measure the time when the collision has taken place very precisely[4]. The Zero Degree calorimeter (ZDC) consists of two hadronic calorimeters which are located 116 m away from the interaction point in beam direction. In addition, two electromagnetic calorimeters are placed on each side of the beam pipe at a distance of about 7 m from the interaction point on the side opposite to the muon arm. The ZDC is used to measure the non-interacting nucleons of the colliding nuclei (spectators) which provide information about the centrality of the collision. In addition, the ZDC measurements can be used to estimate the reaction plane.

The muon spectrometer covers the range of $-4 < \eta < -2.5$ to provide good acceptance down to zero transverse momentum together with a manageable background from hadron decays. It was primarily designed to measure the production of quarkonia well separable within the mass resolution.

The very heart of ALICE are the central-barrel detectors which are covering the midrapidity region ($|\eta| < 0.9$). They are embedded in the L3 solenoid magnet providing a uniform magnetic field of maximum 0.5 T along the beam direction. These detectors are the Inner Tracking System (ITS), the Time Projection Chamber (TPC), the Transition Radiation Detector (TRD), the Time Of Flight detector (TOF), the Photon Spectrometer (PHOS), the Electromagnetic Calorimeter (EMCal), and the High Momentum Particle Identification Detector (HMPID). The ALICE detector is described in full details in [147, 150]. In the following subsections, more detailed information about the sub-detectors relevant for the analyses presented in chapter 4 is given.

3.2.1. V0 detector

The V0 detector [151, 147] consists of two arrays of scintillator counters covering the pseudorapidity regions $-3.7 < \eta < -1.7$ (V0C) and $2.8 < \eta < 5.1$ (V0A). It helps to separates beam–beam interactions from background events, such as beam–gas interactions, and is used to measure the beam luminosity, charged-particle multiplicity, and azimuthal distributions.

[4]The T0 collision time resolution depends on the charged-particle multiplicity and is about 25 ps and 50 ps in Pb–Pb and pp collisions, respectively.

Especially in p–Pb collisions, the V0A signal is used to estimate the mean charged-particle multiplicity density of the events in the direction of the Pb beam. In addition, the V0 provides triggers, namely centrality triggers in Pb–Pb collisions and the minimum bias trigger. The latter requires a coincident signal in V0A and V0C to reduce the contamination from single diffractive and asymmetric electromagnetic interactions.

3.2.2. Inner Tracking System

The Inner Tracking System is the innermost detector system of the central barrel and is composed of six cylindrical layers with three different types of silicon detectors. It surrounds the 800 µm thick beryllium beam pipe which has an outer diameter of 6 cm. The average material budget of the ITS, including the thermal shielding and support, traversed by a straight track perpendicular to the detector surface is $\approx 7.66\%$ of the radiation length X_0 [152]. The ITS provides tracking information for charged particles near the beam pipe and contributes to the excellent momentum and angular resolution of the particle trajectories. It is used in the reconstruction of the interaction vertex (primary vertex) and separated vertices where particle decays took place (secondary vertices). In addition, the ITS allows to measure the distance of closest approach (DCA) of a track to the primary vertex with a resolution below 75 µm for tracks with $p_{\mathrm{T}} > 1$ GeV/c [56, 152].

At radii of 3.9 cm and 7.6 cm from the beam axis, the two innermost layers are mounted, the Silicon Pixel Detectors (SPD). These provide a very good spatial resolution in the transverse plane (12 µm) and in the beam direction (100 µm) [147]. The SPD layers are of central importance for the reconstruction of primary and secondary vertices and for determining the distance of closest approach to the primary vertex. They are designed to deal with high track densities and radiation levels. The SPD provides a trigger signal if at least one pixel of the readout chip indicates a hit. The intermediate and outer layers consist of Silicon Drift Detectors (SDD) and double-sided Silicon Strip Detectors (SSD) at radii between 15 cm and 43 cm. Thanks to the analogue readout of the SDD and SSD, they are capable of providing particle identification information via specific ionisation energy loss of particles passing through the detector. The respective $\mathrm{d}E/\mathrm{d}x$ values are calculated from the deposited charge normalized to the path length. For each track the truncated mean is used to deal with the Landau tail of the energy loss. As an example, the resulting distribution of the average energy loss in the ITS as a function of the momentum in pp collisions at a center-of-mass energy of $\sqrt{s} = 13$ TeV is shown in Figure 3.3. For relativistic particles, where the momentum is high compared to the

mass ($p/m = \beta\gamma$)[5], the expected mean energy loss is given by the Bethe formula which will be discussed in more details in the following paragraph. Below $\beta\gamma = 0.7$, a polynomial shape is used as parametrization to account for the non-linear detector response.

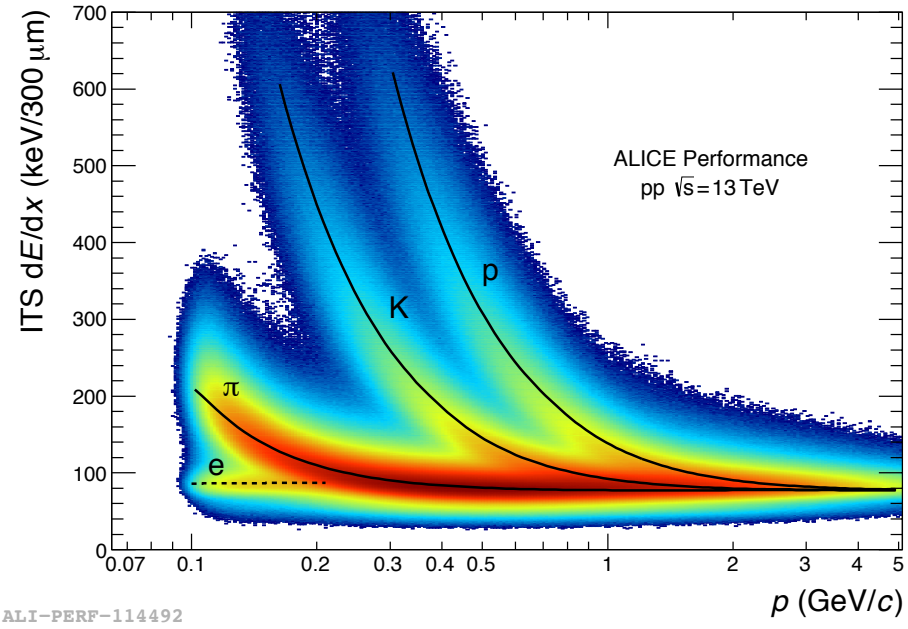

Figure 3.3: The average $\mathrm{d}E/\mathrm{d}x$ of charged particles versus their momentum in the ITS in pp collisions at $\sqrt{s} = 13$ TeV. The expected detector signal for the different particle species are indicated by black lines.

3.2.3. Time Projection Chamber

The main tracking detector of ALICE is the Time Projection Chamber. It provides momentum and particle identification information. The active volume of the TPC ranges from a radius of 85 to 250 cm with respect to the beam axis with a length of 5 m covering a pseudorapidity range of $|\eta| < 0.9$. During the LHC run 1, it was filled with a gas mixture contaning Ne ($\approx 85.7\%$), CO_2 ($\approx 9.5\%$) and N_2 ($\approx 4.8\%$) at atmospheric pressure, while the gas mixture was changed to 90% Ar and 10% CO_2 for LHC run 2. This change has been necessary to avoid the numerous high voltage trips in the TPC readout chambers observed during run 1. The change to a gas mixture containing mostly argon results in stronger primary ionization due to the lower ionization energies of argon compared to neon. This allows to lower the gain in the readout chambers and, thereby, improve the stability of the TPC operation. The TPC is divided

[5] β is the ratio of the particle velocity to the speed of light and the Lorentz factor γ is given by $1/\sqrt{1-\beta^2}$.

into two drift regions by a central high-voltage electrode. Each of the 18 azimuthal sectors of the detector end plates is equipped with two multi-wire proportional chambers (MWPCs). The cathode of the MWPCs is segmented into readout pads. The wire geometry of the readout chambers is adapted to the three different pad sizes used at different radii. Thus, it is different for the outer readout chambers (OROCs) compared to the inner readout chambers (IROCs). The readout is divided into 159 pad rows in radial direction [147]. The current TPC including the gas accounts for only about 3.5% X_0 at $\eta \approx 0$.

Charged particles, passing through the TPC, ionize the gas molecules and, thereby, free electrons. Due to the electrical field, these electrons drift towards the end plates of the TPC. Inside the readout chambers, the electrons are accelerated due to high electrical fields and, thus, ionize more gas molecules which leads to an amplification of the signal. The cloud of ions created by this process induces a mirror charge on the pad plane which is proportional to the energy loss of the initial particle. In the direction transverse to the beam axis, the coordinates of the clusters produced inside the TPC are given by the signal position at the end-cap. The third dimension is reconstructed via the drift time of the electrons. Due to the possibility to measure the energy loss of the particle and the corresponding path length, the TPC provides information about the specific energy loss per unit length ($\mathrm{d}E/\mathrm{d}x$). The relative $\mathrm{d}E/\mathrm{d}x$ resolution in pp and Pb–Pb collisions is about 5% and 7% respectively.

For relativistic charged particles, i.e. $0.1 \lesssim \beta\gamma \lesssim 1000$, and intermediate-Z materials, the mean specific energy loss is given by the Bethe formula [1]

$$-\left\langle \frac{\mathrm{d}E}{\mathrm{d}x} \right\rangle = Kz^2 \frac{Z}{A} \frac{1}{\beta^2} \left[\frac{1}{2} \log \frac{2m_\mathrm{e}\beta^2\gamma^2 W_\mathrm{max}}{I^2} - \beta^2 - \frac{\delta(\beta\gamma)}{2} \right]. \tag{3.3}$$

Here, K denotes the normalization, which is proportional to the Avogadro number, the mass of the electron m_e and the square of the classical electron radius. The charge number of the incident particle is expressed as z while Z and A are the atomic number and mass of the detector material. W_max denotes the maximum energy transfer possible in a single collision and I is the mean excitation energy. The density effect correction to the ionization energy loss $\delta(\beta\gamma)$ due to the polarization of the material effectively truncates the logarithmic increase caused by the increasing extension of the electric field of the incident particle with increasing energy. The probability distribution of the energy loss inside the detector is given by a highly-skewed Landau distribution and, thus, the mean value is not well defined and cannot be measured experimentally. To resolve this problem, the most probably energy loss obtained from a truncated energy loss distribution is used instead of the mean. The behaviour of the most probably energy loss value with $\beta\gamma$ is obtained from a fit to the measured distributions

using a parametrized version of the Bethe formula [150]. As an example, the dE/dx distribution in the TPC as a function of the particle momentum at the inner radius of the TPC taken from the analysis described in chapter 4 is shown.

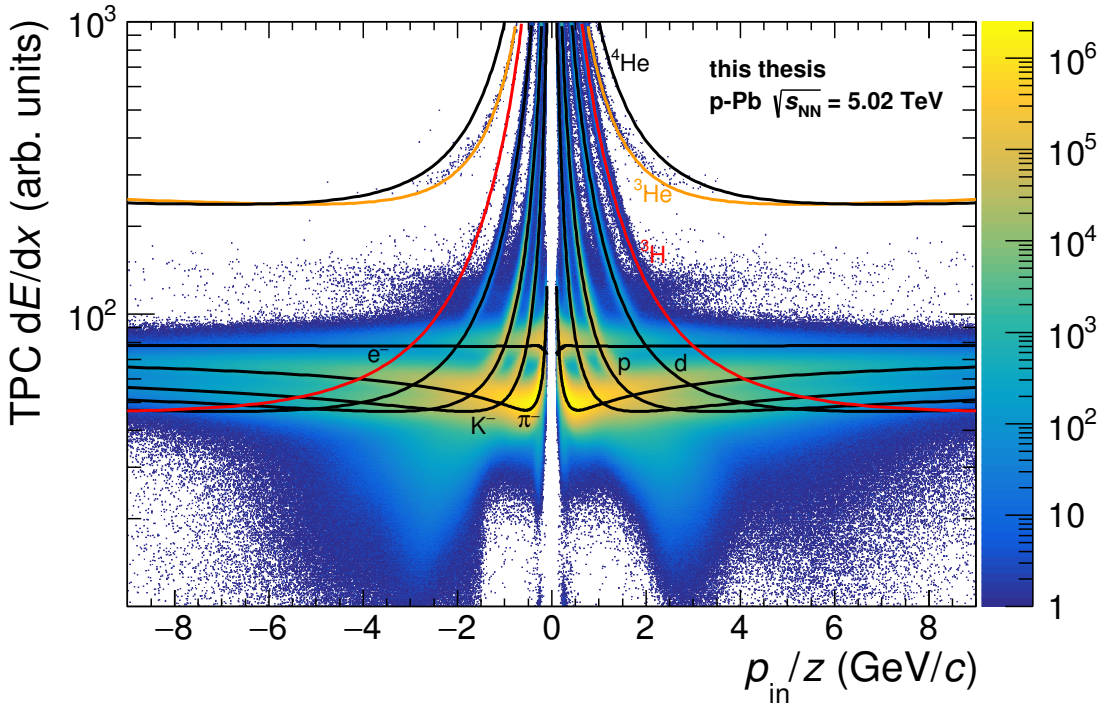

Figure 3.4: The specific energy loss dE/dx in the TPC as a function of the particle rigidity at the TPC inner radius is shown for p–Pb collisions at $\sqrt{s_{\mathrm{NN}}}$ = 5.02 TeV. The parametrisation of the most probably energy loss for the different (anti-)particle species are drawn as lines and labeled for the particles. The curves for (anti-)^{3}H and (anti-)^{3}He, which are analysed in chapter 4, are highlighted in red and orange, respectively.

The ions produced in the readout cambers during the signal amplification drift back to the TPC main volume and disturb the homogeneous drift field. To minimize the effect of the ion back flow into the drift region, the TPC is equipped with a gating grid to close the readout chambers for the ions created in the amplification region and the electrons from the drift region. The gating grid is only opened for one drift-time interval by the trigger and has to be closed in between two events long enough to collect the ions produced in the amplification region. This limits the opening frequency of the gating grid and, hereby, restricts the readout rate of the TPC to 3.5 kHz for pp collisions [153]. The readout rate in central Pb–Pb collisions is limited by the TPC readout system to about 500 Hz [154]. For the coming LHC run 3 and run 4, the readout electronics and the readout chambers of the TPC will be upgraded going

from MWPCs to gas electron multipliers [155]. The upgraded TPC will allow continuous data taking and thus the readout rates are restricted by the expected collision rates. At the moment, a collision rate of 200 kHz is planned for pp and p–Pb collisions as well as 50 kHz for Pb–Pb collisions [154].

3.2.4. Time Of Flight detector

The TOF consists of Multigap Resistive Plate Chamber (MRPCs), a type of detector developed to meet the requirements of a time resolution better than 100 ps and a large number of readout channels [148]. It contains more than 150 000 individual cells with an area of 2.5×3.5 cm^2 each at a radius of 3.7 m from the beam axis covering $|\eta| = 0.9$ and the full azimuth [147]. The TOF detector accounts for about 29.5% X_0. The TOF array provides additional information for particle identification by measuring the flight time of the individual particles between the collision point and the place where the TOF detector is mounted. The collision time is determined by the T0 detectors, which are arrays of quartz Cherenkov counters positioned at $+370$ cm and -70 cm along the beam axis. The T0 covers $4.61 \leq \eta \leq 4.92$ and $-3.28 \leq \eta \leq -2.97$ and provides a collision trigger as well as feedback about the instantaneous luminosity to the LHC accelerator operators. The coincidence of the T0 signals is achieved by adjusting the length of the cables and additional digital delay lines [156]. The event collision time is given by the average collision time measured by the two parts of the T0. If a measurement from only one part of the T0 is available, the time has to be corrected for the primary vertex z position obtained using the SPD. Another option to estimate the collision time is to use a χ^2-minimization procedure based on the arrival time of all the particles at the TOF detector. Using one of three possible mass hypothesis (pion, kaon or proton mass) for each track, different collision times can be calculated as the weighted average of the differences between the measured arrival times of all the particles and the expected times of flight for the chosen mass hypothesis. The final collision time is obtained as the value which minimizes the weighted sum of the squared differences between the expected time of flight for a chosen mass hypothesis and the arrival time in TOF corrected by the collision time corresponding to the set of mass hypothesis chosen. In both cases, the weights are given by the inverse of the sum of the time resolution of the TOF detector and the uncertainty on the expected time of flight for the chosen mass hypothesis. The last option is to use the bunch crossing time from the LHC. A detailed description of the determination of the event collision time can be found in [157]. The resolution of the overall time-of-flight measurement is about 80 ps [158]. Using the time of flight and the total length of the track, the velocity of the particle can be calculated and compared to the expected one for a given particle species. The distribution of

the particle velocities compared to the speed of light (β) as a function of the particle momentum obtained in p–Pb collisions at $\sqrt{s_{\mathrm{NN}}} = 5.02$ TeV is reported in Figure 3.5. Despite the

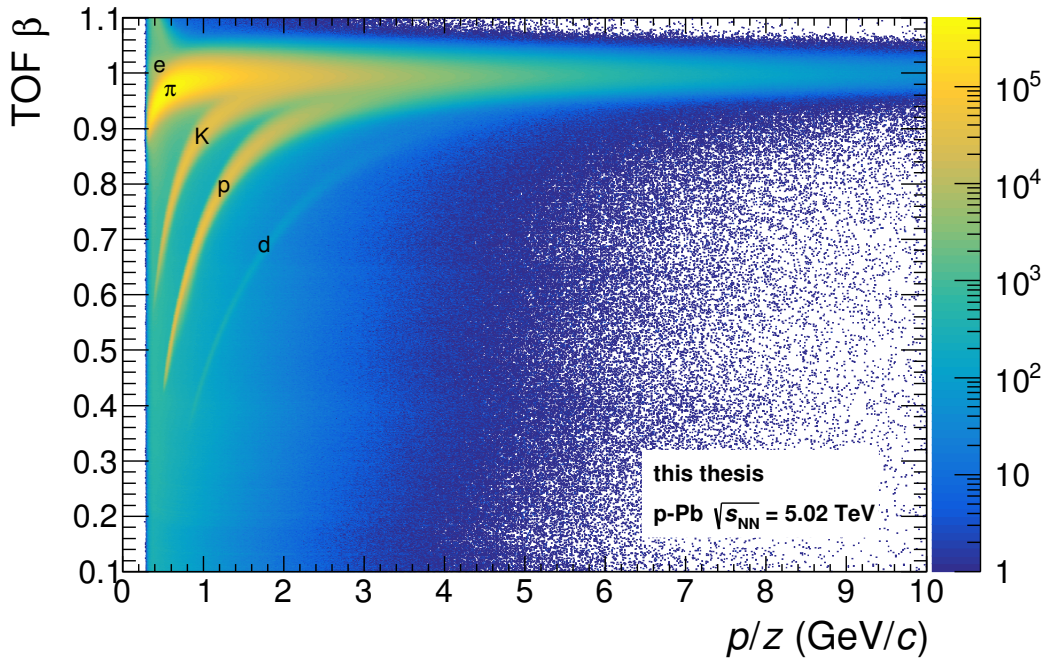

Figure 3.5: The distribution of the velocity, expressed as a fraction β of the speed of light, measured by the TOF detector is shown as a function of the particle rigidity measured in p–Pb collisions at $\sqrt{s_{\mathrm{NN}}}$ = 5.02 TeV. The bands belonging to the different particle species are labeled with the particle names. The background is coming from mismatched hits in the TOF detector.

background coming from incorrect assignment of TOF clusters to a track, this method allows to distinguish different particle species. The mismatch background is strongly dependent on the track density in the event. The particle identification information provided by the TOF detector complements the particle identification capability of the TPC.

3.3. Event reconstruction

For reconstruction of an event in the central barrel, the raw data from all detectors has to be first reconstructed locally for each detector. The resulting information about the spatial coordinates, the signal times and amplitudes as well as associated uncertainties of the place where the particle was crossing the active area of the detector is summarized in the ”clusters”. For the PID detectors, the clusters also includes the information about the corresponding PID

variable, e.g. time of flight or specific energy loss. The subsequent event reconstruction flow is summarized in Figure 3.6 and described in more details in [150].

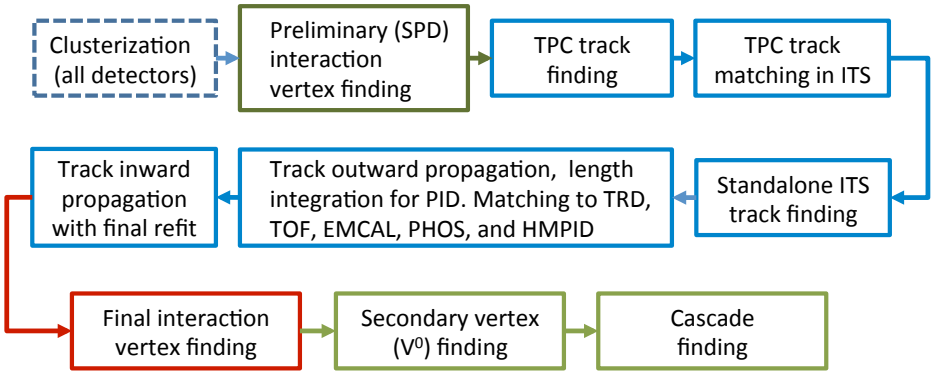

Figure 3.6: The flow chart summarizing the ALICE event reconstruction taken from [150].

The first step of the global event reconstruction is the preliminary determination of the interaction vertex. It is defined as the point where most of the SPD tracklets, which are straight lines constructed using pairs of clusters in both SPD layers, meet. An inward-outward-inward scheme is used for the track finding and fitting which starts with the reconstruction of tracks in the TPC. Track seeds are created at the outer radius of the TPC using either two TPC clusters and the interaction vertex or three TPC clusters without the vertex information. The tracks seeds are propagated inwards and their parameters are updated by the nearest cluster fulfilling a proximity selection at each step. Since the same TPC clusters can be added to different seeds, this procedure can lead to multiple reconstructed tracks for the same particle. Thus, a search for tracks with a high number of shared clusters is performed and the worse track version is rejected. The quality of the track version is determined based on the number of clusters, the cluster density and the momentum. Only tracks which have at least 20 out of 159 possible clusters and which miss at maximum 50% of the geometrically possible clusters (findable clusters) are accepted and propagated to the TPC inner radius. Based on the specific energy loss in the TPC a preliminary particle identification is performed and a mass hypothesis is chosen. These tracks are propagated to the outer layer of the ITS and are used as track seeds for the track finding in the ITS. These seeds are propagated inwards and updated with ITS clusters in their proximity. Again a rejection of worse versions of the same physical track is applied. Since the TPC efficiency drops at low transverse momenta due to the energy loss and multiple Coulomb scattering in the detector material, an ITS standalone track finding using the remaining ITS clusters is performed in addition. The seeds for this reconstruction step are defined by three clusters in the innermost ITS layers and the interaction point. These

seeds are propagated towards the outer radius of the ITS and updated with clusters fulfilling the proximity requirement. The ITS standalone reconstruction allows to reconstruct tracks down to a momentum of about $p = 80$ MeV/c [150]. All reconstructed tracks are propagated to the point where they are closest to the interaction vertex. From this position the outward propagation starts. The tracks are refitted using the Kalman-filter approach[6] [159]. During this stage the clusters from the TRD, TOF, EMCal, PHOS, and HMPID are added. In the final stage of the track reconstruction the tracks are propagated inwards again and refitted. The final track properties, e.g. position and curvature at the point closest to the interaction vertex and the covariance matrix, are determined. The curvature is used to calculate the momentum of the particle. The tracks reconstructed with the TPC and ITS, so called global tracks, are used to determine the primary interaction vertex more precisely.

At the end, a search for photon conversions and secondary vertices from particle decays is performed which is sketched in Figure 3.7 for the decay of K^0_s and Ξ^-. The reconstruction

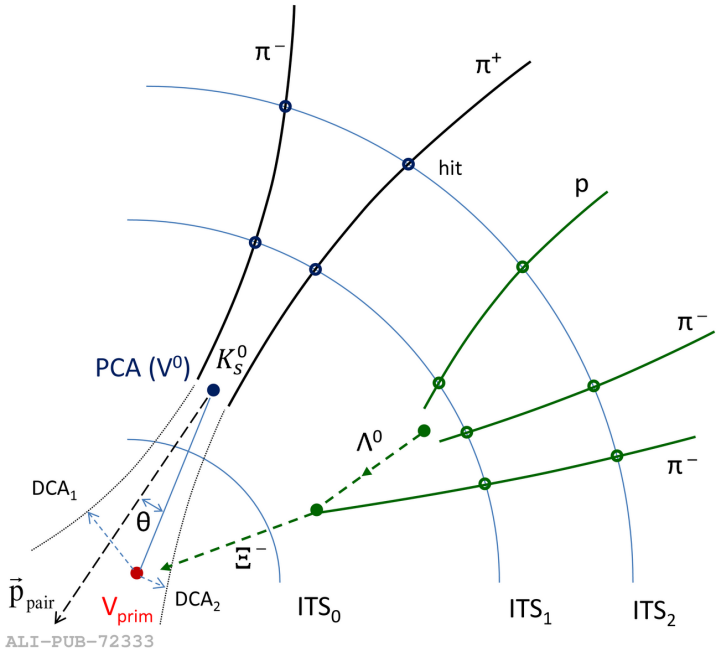

Figure 3.7: The procedure of the reconstruction of secondary vertices is shown using the decay of K^0_s and Ξ^- as an example. The reconstructed charged-particle tracks are shown as solid lines, while auxiliary vectors and the extrapolations to the primary vertex are indicated by dashed lines [150].

of secondary vertices is based on tracks with a distance-of-closest approach to the primary vertex larger than 0.5 mm in pp and 1 mm in Pb–Pb collisions. Pair of track with opposite

[6] A linear Kalman filter is the optimal recursive estimator of the state vector of a linear dynamic system.

charge sign, called V^0 candidates, are reconstructed and basic selections based on the distance between the tracks at the point of closest approach or the cosine of the pointing angle of the resulting mother particle are applied. The pointing angle is the angle θ between the total momentum vector of the pair $\vec{p}_{\text{pair}}$ and the straight line connecting the primary and secondary vertices. The last step of the event reconstruction is the search for cascade (Ξ) decays by combining V^0 candidates with a mass close to the mass of the lambda particle with secondary tracks. If the point of closest approach of the V^0 and the secondary track is separated from the primary vertex by more than 0.2 cm and the mutual distance is small enough, the resulting mother is stored as cascade candidate.

3.4. Monte Carlo simulations

Detailed simulations of the collisions are needed to correct the measurements for the reconstruction efficiency and the acceptance selection during the data analysis as well as for modeling purposes. The creation of these simulations employ Monte Carlo techniques and can be separated into two stages. The first one is the event generation, in which all primary stable or weakly decaying particles are produced. The strong decays of unstable particles is typically treated by the event generators. In this stage of the simulation, all processes starting from the interaction of the beam particles in the interaction region up to the hadronization and strong decay of unstable hadrons has to be described. As a consequence, the event generators have to deal with very short distance physics, which can be calculated from first principles, e.g. via perturbative approaches, up to soft hadronic phenomena described in QCD-inspired models. Typical event generators are PYTHIA [160] or HERWIG [161] for pp collisions, EPOS LHC [162], HIJING [163] and DPMJET [164] for heavy-ion collisions. A more detailed discussion of Monte Carlo event generators can be found in [1].

The particles produced in the first stage of the simulation have to be transported through a precise description of the experiment using dedicated transport codes, e.g. GEANT3 [165] and GEANT4 [166]. These codes provide the information about the energy loss of the particle in the detector and the production of secondary particles due to the interaction with the material. In addition, they handle further particle decays. The space point and the energy deposited in the active areas of the detector is calculated and stored as a ”hit”. By simulating the response of each detector, the hits are converted into the corresponding signal in the readout electronics which is stored in the same format as for real raw data. The resulting output of the simulation is reconstructed using the same algorithm as for the measurements done with the physical detector setup.

4. Data analysis

In this chapter, the analysis techniques used to measure the production of ^{3}H, ^{3}He and their antinuclei in p–Pb collisions at a centre-of-mass energy per nucleon pair $\sqrt{s_{\mathrm{NN}}}$ = 5.02 TeV with the ALICE detector are described. The analysed data set was recorded during a short data taking campaign at the beginning of November 2016. To maximize the amount of collected data, about 50% of the recorded events were collected without the information from the silicon drift detector (SDD), which had been still busy with processing a previous event due to it long readout time[1]. To ensure a common track reconstruction for all events and increase the size of the analysed data sample, the SDD information is omitted for all events independent of its availability. The events were collected applying a minimum-bias trigger which requires coincident signals in the V0A and V0C detectors to suppress events from single diffractive and asymmetric electromagnetic interactions. The criteria used for the event and track selection, the particle identification and signal extraction techniques are explained in the following sections. The resulting raw yields of (anti-)^{3}H and (anti-)^{3}He are corrected for the detector acceptance, the reconstruction efficiency, and for contributions from secondary nuclei. These secondary nuclei are produced either in spallation reactions in the beam pipe and the detector material or via weak decays of (anti-)$^3_\Lambda$H. The aforementioned corrections are calculated using Monte Carlo simulations. Finally, the evaluation of the systematic uncertainties is illustrated and discussed.

The production of (anti-)^{4}He is expected to be suppressed by about a factor of 600 compared to (anti-)^{3}He [167] which indicates that the current data set is not yet sufficiently large to study the production of $^4\overline{\mathrm{He}}$. Nevertheless, the evaluation of an upper limit based on the non-observation of $^4\overline{\mathrm{He}}$ is reported at the end of this chapter.

The analyses described in this chapter are also published in a recent paper by the ALICE collaboration [168] which was mostly written by the same author as this thesis.

[1] The readout time of the SDD is of the order of 1 ms which is about twice as long as the one of the TPC [150]

4.1. Event and track selection

Event selection

The recorded events can be superimposed by additional collisions occurring in the same bunch crossing ("same-bunch-crossing pile-up") or a bunch crossing different from the one triggering the data acquisition ("out-of-bunch pile-up") which are recognized as only one single event. These pile-up events can be due to e.g. beam-gas interactions or collisions with debunched protons (ions). Such events are not the type of events of interest and lead to a bias in the charged-particle multiplicity density estimation of the event and the observables of interest. Out-of-bunch pile-up has a different effect on each of the sub-detectors of the ALICE apparatus because of the different readout times. Thus, tracks from these pile-up events can be rejected by correlating the information of different detectors. The number of same-bunch and out-of-bunch pile-up within the SPD readout time can be reduced to a negligible level by rejecting events with multiple vertices. These vertices, which are identified with the SPD, have to be separated along the beam direction by more than 0.8 cm. A minimum number of contributors to the reconstructed pile-up vertices is required which depends on the number of SPD track segments (tracklets) in the event. The pile-up vertices have to be compatible with the expected collision region given by the overlap region of the LHC beams. In addition, the pile-up events can be tagged as events with multiple vertices reconstructed using tracks not only employing the SPD but taking also information from the TPC and TOF detectors into account. For these pile-up vertex candidates, a minimum of 5 contributing tracks and a maximum χ^2 per contributor of 5 for the vertex fit is required to reject fake pile-up vertices. Events are rejected if the additional vertices are separated from the primary vertex by more than 15 times the distance along the beam direction normalized to the combined uncertainty, which is calculated as the sum in quadrature of the vertex uncertainties. In order to reject residual background collisions, to keep the conditions of the detectors as uniform as possible, and to avoid edge effects, the coordinate of the primary vertex along the beam axis is required to be within ± 10 cm from the nominal interaction point in ALICE. Primary vertices can be reconstructed from tracks using the information from SPD, TPC, and TOF or hits in the SPD only. Primary vertex candidates which are found with both methods are required to be separated by less than 0.5 cm. The pile-up rejection excludes less than 1% of the recorded events, while the reconstruction of the primary vertex and the quality requirements on it removes about 1.5%. The largest fraction of events, about 13.3%, is rejected by the requirements on the vertex position. The total number of events that fulfill the event selection criteria is 5.4×10^8, which corresponds to about 85% of all recorded events.

The system size dependence of the production of (anti-)^{3}He is studied by splitting the sample of events in four charged-particle multiplicity classes. These are defined as percentiles of the V0A signal. The V0A detector is the part of the V0 detector mounted in the direction of the movement of the center-of-mass system. The multiplicity classes are summarized in Table 4.1 together with the corresponding mean charged-particle multiplicity densities at midrapidity, $\langle \mathrm{d}N_{\mathrm{ch}}/\mathrm{d}\eta_{\mathrm{lab}} \rangle_{|\eta_{\mathrm{lab}}|<0.5}$. The values of $\langle \mathrm{d}N_{\mathrm{ch}}/\mathrm{d}\eta_{\mathrm{lab}} \rangle_{|\eta_{\mathrm{lab}}|<0.5}$ are obtained from a separate study of the distribution of tracklets, defined by the primary vertex and one hit in each of the SPD layers. The measured distribution is corrected for the contamination from tracklets reconstructed from hits not produced by the same primary particle, the acceptance, and the efficiency for a primary particle to produce a tracklet. These corrections are obtained from a MC simulations using DPMJET [164] and GEANT3 [165]. A detailed description of this study and the procedure to estimate the corresponding uncertainties is given in [169].

V0A Classes	$\langle \mathrm{d}N_{\mathrm{ch}}/\mathrm{d}\eta_{\mathrm{lab}} \rangle_{\lvert\eta_{\mathrm{lab}}\rvert<0.5}$
0–10%	40.6 ± 0.9
10–20%	30.5 ± 0.7
20–40%	23.2 ± 0.4
40–100%	10.1 ± 0.2

Table 4.1: Summary of the V0A multiplicity classes and their corresponding mean charged-particle multiplicity densities at midrapidity. The values and their uncertainties are taken from [170].

Track selection

Due to the different magnetic rigidity of the beam particles and the 2-in-1 magnet design of the LHC, the momenta of the beam particles are different for asymmetric systems such as p–Pb. As a consequence, the nucleon-nucleon center-of-mass system (CMS) moves with a rapidity of $\Delta y = 0.465$ in the direction of the proton beam with respect to the laboratory frame. Thus, the rapidity of a particle measured perpendicular to the beam direction is not $y_{\mathrm{CMS}} = 0$, as for pp and Pb–Pb collisions, but $y_{\mathrm{CMS}} = -0.465$.

For the reported analyses, primary track candidates with transverse momentum $p_{\mathrm{T}} > 1.5$ GeV/c, pseudorapidity $|\eta_{\mathrm{lab}}| \leq 0.9$ and rapidity $-1 \leq y_{\mathrm{CMS}} < 0$ are selected. To ensure a good resolution of the track momentum and specific energy loss $\mathrm{d}E/\mathrm{d}x$ in the TPC, additional quality criteria are imposed on the tracks. They are required to have a minimum number of reconstructed space points in the TPC, $N_{\mathrm{cls}}^{\mathrm{TPC}}$, of 70 for (anti-)^{3}He and 120 for (anti-)^{3}H out of a maximum of 159 clusters, respectively. For ^{3}H candidates, a stronger selection is used in order

to reduce the contamination from other particle species. This improvement is demonstrated in Figure 4.1, in which the TPC $\mathrm{d}E/\mathrm{d}x$ signal for ^{3}H candidate tracks in $1.5 \leq p_\mathrm{T} < 2.0$ GeV/c is shown. In addition, at least two hits in the ITS ($N_\mathrm{cls}^\mathrm{ITS} \geq 2$), with at least one in the SPD, are

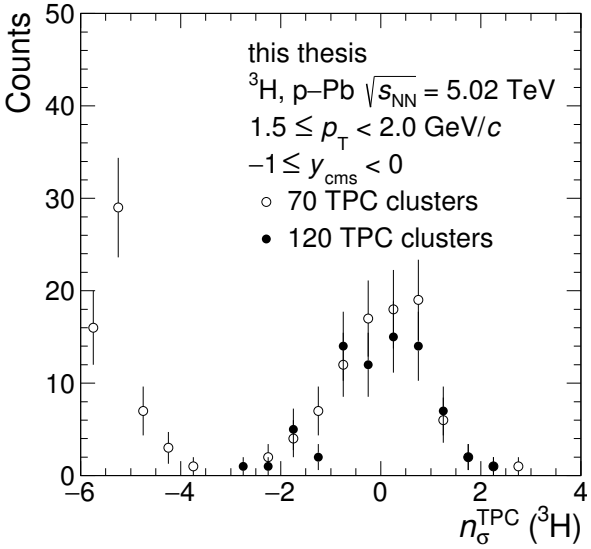

Figure 4.1: The distribution of the specific ionization energy loss in the TPC of ^{3}H candidate tracks compared to the expected value normalized by the TPC $\mathrm{d}E/\mathrm{d}x$ resolution in $1.5 \leq p_\mathrm{T} < 2.0$ GeV/c is shown for two different TPC cluster selections.

required. The latter requirement significantly suppresses the contribution of secondary tracks. During the data taking, the SDD was only read out for about half of the events recorded in order to maximize the data acquisition rate. To maximize the size of the data set and to unify the reconstruction of the events, the information from the SDD is not used for the current analyses, which reduces the maximum number of hits in the ITS to 4. The quality of the track fit within the TPC is quantified by the value of $\chi^2/N_\mathrm{cls}^\mathrm{TPC}$ which is required to be less than 4. In addition, the ratio of the number of reconstructed TPC clusters to the number of findable TPC clusters is required to be larger than 80%. The number of findable clusters is the maximum number of geometrically possible clusters which can be assigned to a track. The contribution from secondary tracks that are produced, e.g. by spallation in the detector material or the beam pipe, is further suppressed by restricting the distance of closest approach (DCA) to the primary vertex. The absolute value of the DCA in the transverse plane ($\mathrm{DCA_{xy}}$) and in the beam direction ($\mathrm{DCA_z}$) are required to be smaller than 0.1 cm and 1 cm, respectively.

4.2. Particle identification

The identification of (anti-)^{3}He and (anti-)^{3}H is based on the specific ionization energy loss $\mathrm{d}E/\mathrm{d}x$ measured by the TPC which is shown as a function of the particle rigidity in Figure 4.2. For (anti-)^{3}He, this particle identification (PID) information is enough to ensure a sufficiently pure sample of candidates while it has to be combined with the time of flight measured with the TOF detector for (anti-)^{3}H.

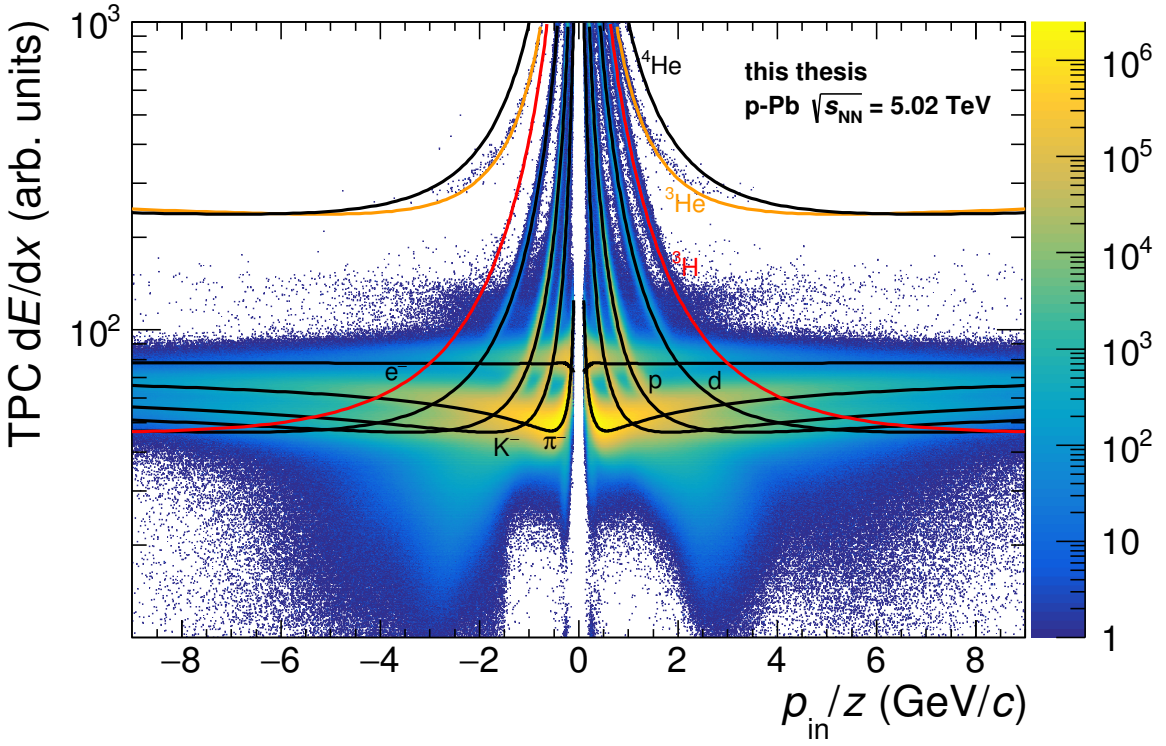

Figure 4.2: The specific energy loss $\mathrm{d}E/\mathrm{d}x$ in the TPC as a function of the particle rigidity at the TPC inner radius is shown for p–Pb collisions at $\sqrt{s_{\mathrm{NN}}}$ = 5.02 TeV. The parametrisation of the most probably energy loss for the different (anti-)particle species are drawn as lines and labeled for the particles. The curves for (anti-)^{3}H and (anti-)^{3}He are highlighted in red and orange, respectively.

PID for ^{3}He

For ^{3}He, the TPC $\mathrm{d}E/\mathrm{d}x$ provides excellent separation from other particle species over a large range of momentum due its charge $z = 2e$. This can be understood remembering that the specific energy loss in the TPC depends quadratically on the charge of the particle and can be described by the Bethe formula as discussed in section 3.2.3. Even though the energy

loss of (anti-)^{4}He becomes similar to that of (anti-)^{3}He above a rigidity $p/z = 4$ GeV/c, the identification of (anti-)^{3}He in the TPC is not affected because the production of (anti-)^{4}He is expected to be suppressed by about factor of 600 compared to (anti-)^{3}He [167]. Thus, the contamination by ^{4}He is neglected in this analysis.

Even though the TPC dE/dx calibration is done as a function of momentum, the particle identification is performed in transverse momentum intervals to be able to directly subtract the contamination from other particle species for each p_{T} interval. The ^{3}He and ^{3}H candidates are selected using the difference between the measured specific energy loss, $(\mathrm{d}E/\mathrm{d}x)^{\mathrm{meas}}$, and the expected value, $\langle \mathrm{d}E/\mathrm{d}x \rangle^{\mathrm{exp}}$, for ^{3}He or ^{3}H in units of the energy loss resolution of the TPC ($\sigma^{\mathrm{TPC}}_{\mathrm{d}E/\mathrm{d}x}$),

$$n_{\sigma}^{\mathrm{TPC}} = \frac{(\mathrm{d}E/\mathrm{d}x)^{\mathrm{meas}} - \langle \mathrm{d}E/\mathrm{d}x \rangle^{\mathrm{exp}}}{\sigma^{\mathrm{TPC}}_{\mathrm{d}E/\mathrm{d}x}}. \tag{4.1}$$

The specific energy loss of ^{3}H is similar to the one of ^{3}He for $p_{\mathrm{T}} < 2.5$ GeV/c which leads to

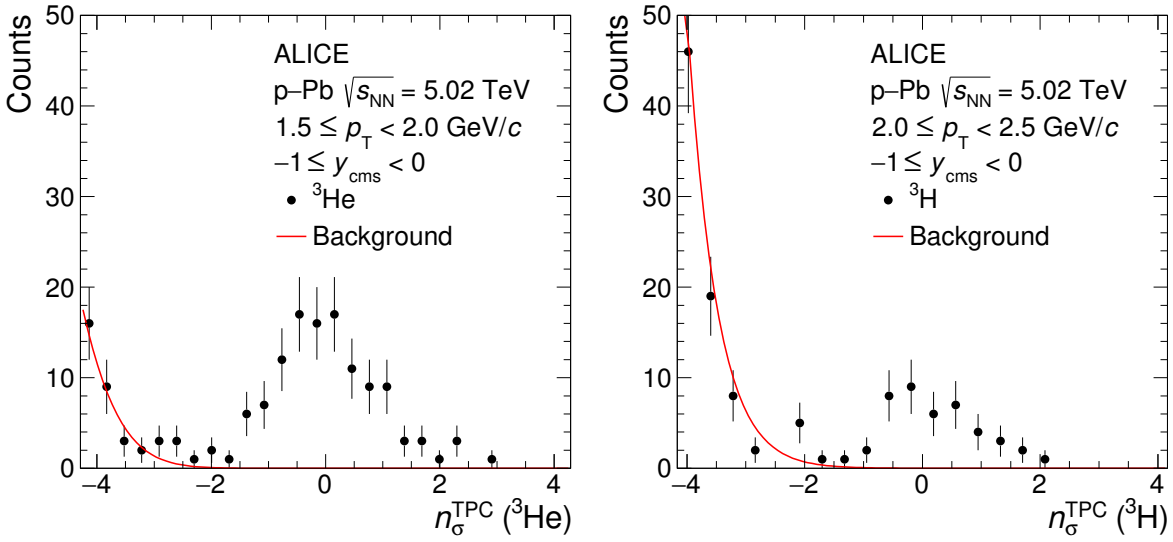

Figure 4.3: The distribution of the specific ionization energy loss (dE/dx) in the TPC of the candidate tracks compared to the expected value for ^{3}He or ^{3}H ($n_{\sigma}^{\mathrm{TPC}}$) in the p_{T} range of $1.5 \leq p_{\mathrm{T}} < 2.0$ GeV/c and 2.0 GeV/c $\leq p_{\mathrm{T}} < 2.5$ GeV/c for ^{3}He (left panel) and ^{3}H (right panel), respectively. The background, which is visible on the left side of the signal, is fitted with a Gaussian function, which is indicated by the red line to estimate the contamination.

the background contribution by ^{3}H shown in the left panel of Figure 4.3. This background is not observed for anti-^{3}He which indicates that it is mostly due to secondary ^{3}H from spallation

reactions with a measured $\mathrm{d}E/\mathrm{d}x$ value inside the higher $\mathrm{d}E/\mathrm{d}x$ tail of the distribution. This background causes a contamination of the extracted ^{3}He signal which is found to be below 0.5%. The fraction of contamination is estimated from data by fitting the background on the left side of the ^{3}He peak in the $\mathrm{d}E/\mathrm{d}x$ distribution with a Gaussian function. The signal is extracted by subtracting the contamination and counting the number of candidates inside the signal region, defined as $[-3,3]$. The signal extraction of $^3\overline{\mathrm{He}}$ is not affected because the abundance of $^3\overline{\mathrm{H}}$ is much lower due to the fact that it cannot be produced via spallation. The production of a nucleus-antinucleus-pair in the detector material or the beam pipe is highly suppressed due to the large amount of energy needed for this process.

PID for ^{3}H

For ^{3}H, the PID signal in the TPC contains a large background from more abundant particle species, i.e. mostly electrons and pions, because ^{3}H carries only one elementary charge. This background is largely suppressed by a preselection based on the measured time of flight, which is required to be within $\pm 3\sigma_{\mathrm{TOF}}$ from the expected value, where σ_{TOF} is the resolution in the time-of-flight measurement. At $p_{\mathrm{T}} > 2.0$ GeV/c, the TOF preselection is not sufficient

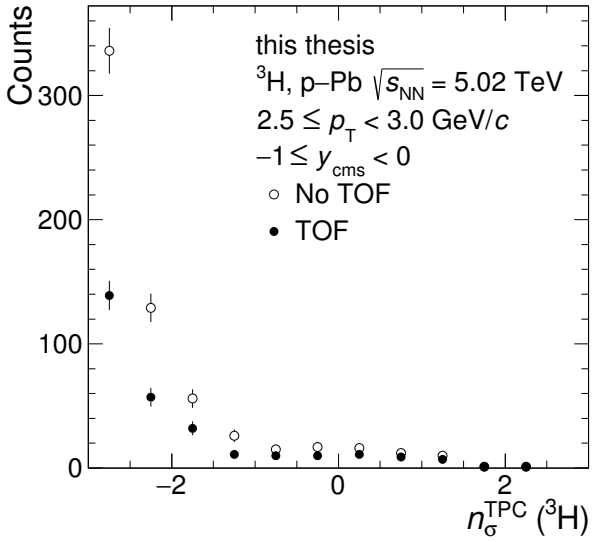

Figure 4.4: The distribution of the specific ionization energy loss in the TPC of ^{3}H candidate tracks compared to the expected value normalized by the TPC $\mathrm{d}E/\mathrm{d}x$ resolution in $2.5 \leq p_{\mathrm{T}} < 3.0$ GeV/c is shown with and without applying a preselections with the TOF detector.

anymore to completely suppress the contamination by other particles which leads to an increasingly large contamination for higher p_{T}. The reduction of the contamination due to the

TOF preselection, as well as, the remaining background is indicated in Figure 4.4 which shows the distribution of $n_{\sigma}^{\mathrm{TPC}}$ for $2.5 \leq p_{\mathrm{T}} < 3.0$ GeV/c. As shown in the right panel of Figure 4.3, the contamination of the signal for ^{3}H ($^3\overline{\mathrm{H}}$) is extracted following the same strategy as for ^{3}He. It is $\sim 7(9)\%$ and $\sim 34(21)\%$ in $2 \leq p_{\mathrm{T}} < 2.5$ GeV/c and $2.5 \leq p_{\mathrm{T}} < 3$ GeV/c, respectively.

4.3. Raw yields

The analysis is restricted to the transverse momentum range $1.5 \leq p_{\mathrm{T}} < 5$ GeV/c for (anti-)^{3}He and $1.5 \leq p_{\mathrm{T}} < 3$ GeV/c for (anti-)^{3}H. The latter transverse momentum interval is smaller because the additional requirement on the TOF signal reduces the reconstruction efficiency as discussed in more detail in section 4.4.3 which leads to a smaller number of observed (anti-)^{3}H candidates. In addition, the selection of a clean sample of (anti-)^{3}H candidates becomes extremely difficult above 3 GeV/c. The raw yields of ^{3}He and $^3\overline{\mathrm{He}}$ as well as ^{3}H and $^3\overline{\mathrm{H}}$

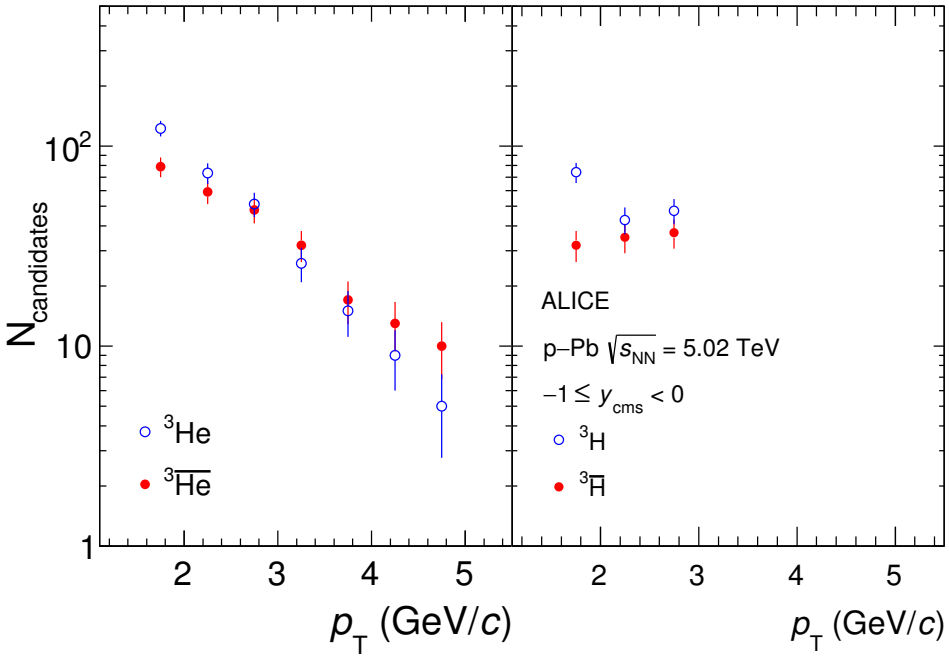

Figure 4.5: The raw yields of (anti-)^{3}He and (anti-)^{3}H obtained from INEL > 0 p–Pb collisions at $\sqrt{s_{\mathrm{NN}}} = 5.02$ TeV are shown as a function of p_{T} in the left and the right panel, respectively. Statistical uncertainties are indicated by vertical bars.

are presented as a function of the transverse momentum in Figure 4.5. Here, the transverse momentum is already corrected for effects caused by the track reconstruction. These effects and the correction procedure will be explained in section 4.4.1. The difference between the

number of nuclei and antinuclei candidates at low p_{T} is predominantly caused by the contribution from secondary nuclei produced in spallation reactions of primary particles with the beam pipe or the detector material. The methods to estimate and correct for these contributions are discussed in section 4.4.2.

4.4. Corrections based on Monte Carlo simulations

The reconstruction efficiencies of (anti-)^{3}H and (anti-)^{3}He, the estimate of the contribution from secondary nuclei produced by spallation in the detector material, and the subtraction of the feed-down from weak decays of hypertriton are obtained using Monte Carlo (MC) simulations. Events produced using the EPOS LHC generator [162] are enriched by an additional sample of injected (anti-)nuclei. These are generated with a flat distribution in transverse momentum and rapidity within $0 < p_{\mathrm{T}} < 8$ GeV/c and $-1 \leq y_{\mathrm{cms}} \leq 1$, respectively. Ten deuterons, ^{3}H, ^{3}He, ^{4}He, and twenty hypertritons as well as their antinuclei are injected into each p–Pb collision. Here, EPOS LHC is employed to ensure a realistic charged-particle multiplicity distribution of the underlying events. Due to technical reasons the injection of nuclei is not possible for event generated with DPMJET [164] which is the generator used for the general purpose MC sample. In the following analyses, the estimation of the amount of secondary nuclei from material is based on the distributions taken from the general purpose MC sample to avoid any bias due to the injection of nuclei. For the particle propagation and simulation of the detector response, GEANT3 [165] is used for both MC simulations.

4.4.1. Transverse momentum shift

During the track reconstruction, a mass hypothesis for the particle has to be made, which in ALICE is based on the specific energy loss in the TPC. Due to ambiguities between ^{3}He and ^{3}H candidates at low p/z, the wrong mass hypothesis is used for a sizable fraction of ^{3}He candidates below $p_{\mathrm{T}} = 2$ GeV/c. Due to the wrong mass assumption, the charge is assumed to be one elementary charge instead of two. The wrong values for the charge and the mass lead to a wrong energy loss correction during the track reconstruction. Thus, the reconstructed p_{T} deviates from the true one. This effect is quantified by comparing the difference of the reconstructed and the true p_{T} in MC as a function of the reconstructed p_{T} as shown in Figure 4.6. The obtained distribution is fitted with a phenomenological motivated function which

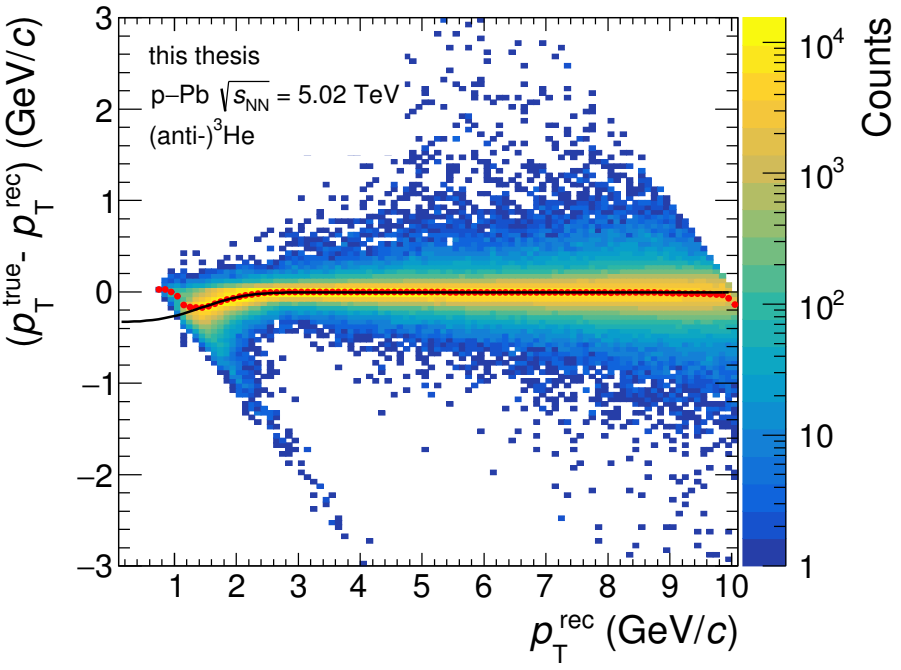

Figure 4.6: The difference between the reconstructed and the true transverse momentum of ^{3}He in the MC simulation as a function of the reconstructed p_T is shown together with the mean for each p_T^{rec} interval (red dots). The black line represents the fit to this distribution.

is used to correct for the p_T shift during the analysis and the evaluation of the reconstruction efficiency:

$$f(p_T^{rec}) = A + B \cdot \exp(C \cdot (p_T^{rec})^3) \tag{4.2}$$

The fit parameters are found to be $A = (6.8 \pm 0.4) \cdot 10^{-4}$ GeV/c, $B = -0.3641 \pm 0.0009$ GeV/c and $C = -0.2386 \pm 0.0005$ (GeV/c)$^{-3}$. In the following, p_T denotes the transverse momentum corrected applying this parametrisation to recover the true transverse momentum also in data. The deviations of the parametrisation from the mean of the distribution at $p_T^{rec} < 1.5$ GeV/c and $p_T^{rec} > 9.8$ GeV/C are not within the transverse momentum interval used for this analysis and, thus, have no effect on the result.

4.4.2. Secondary nuclei from material

Secondary nuclei are produced as spallation fragments in the interactions between primary particles and nuclei in the detector material or in the beam pipe. The contribution of secondary

nuclei can experimentally be separated from that of primary nuclei using the distance of closest approach (DCA) to the primary vertex.

The DCA_{xy} distribution of primary nuclei peaks at zero, while the one of secondary nuclei is flat over most of the DCA_{xy} range and has a small peak around $DCA_{xy} = 0$ cm for low p_T, as shown in Figure 4.7. This structure is artificially created by the tracking algorithm due to incorrect cluster associations in the first ITS layer. As discussed in section 2.3, the particles produced in the pre-equilibrium particle emission phase of the spallation process are emitted in the direction of the projectile, i.e. a primary particle. Thus, these particles point back to the primary vertex. Nevertheless, the resulting DCA distribution is expected to be broader that the observed peak at zero. The DCA_{xy} distribution of ^{3}He in data is obtained by applying stricter

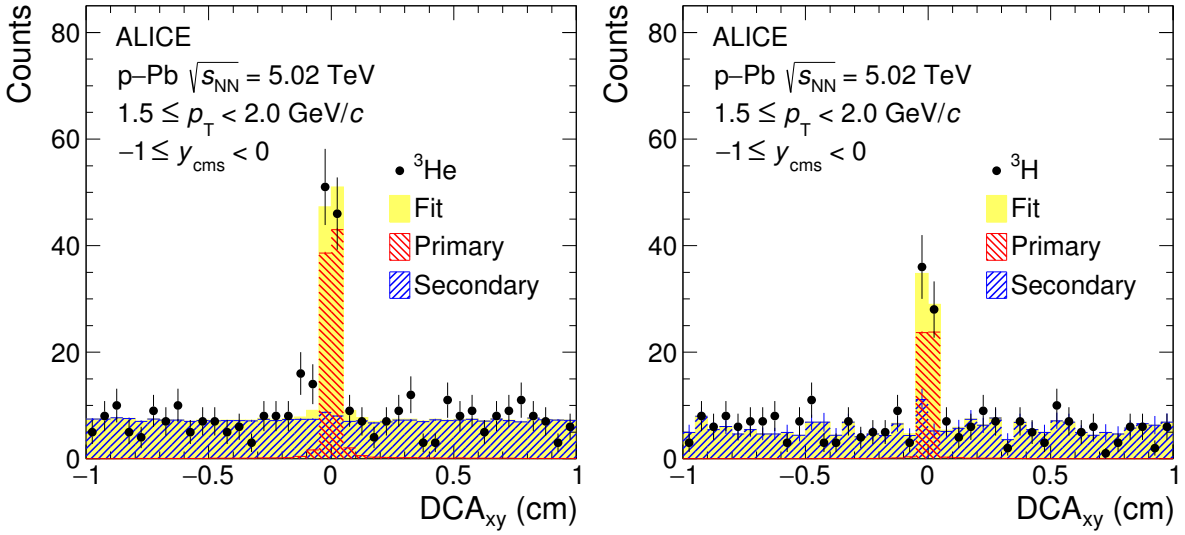

Figure 4.7: The DCA_{xy} distribution within $1.5 \leq p_T < 2.0$ GeV/c is shown together with the MC template fit for ^{3}He (left panel) and ^{3}H (right panel). The corresponding primary and secondary contributions are also indicated.

PID requirements compared to those described in section 4.2 to ensure a pure ^{3}He sample. In particular, the difference between the measured dE/dx and the expected average for ^{3}He is required to be in the range [-2σ, 3σ] for $p_T < 2$ GeV/c and in the range [-2.5σ, 3σ] for $2 < p_T < 2.5$ GeV/c. The remaining contamination is at maximum 0.1% for ^{3}He and 1.2% for ^{3}H for $p_T < 2.5$ GeV/c.

The fraction of primary nuclei is obtained by a two-component fit to the measured DCA_{xy} distribution, one for the signal and the other for the secondaries. The distribution of both components is obtained from Monte Carlo simulations. Due to the lack of secondary ^{3}He in the MC simulation, the distributions of secondary deuterons are used as a proxy. For a given p_T,

the template of deuterons at half the p_{T} is used to compensate for the charge difference. The

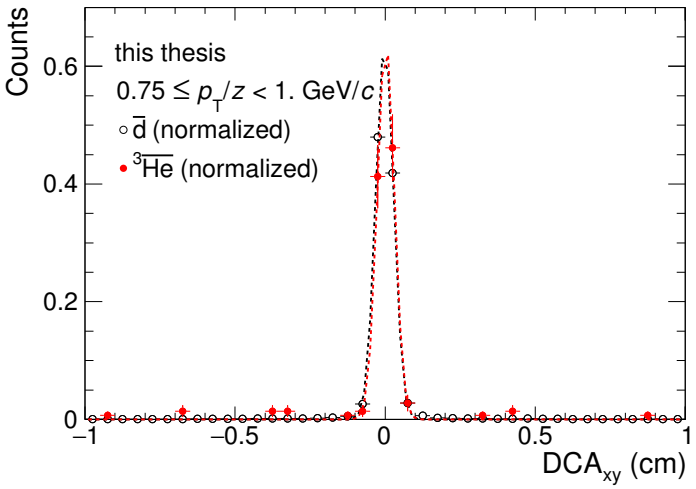

Figure 4.8: The $\mathrm{DCA_{xy}}$ distribution of $\bar{\mathrm{d}}$ and $^3\overline{\mathrm{He}}$ is shown within $0.75 \leq p_{\mathrm{T}}/z < 1.0$ GeV/c. Both distributions are normalized by their integral and fitted with a Gaussian function which highlights that the distributions have the same width.

difference between the multiple Coulomb scattering for deuterons and ^{3}He has a negligible impact on the compatibility of the $\mathrm{DCA_{xy}}$ distributions. This is confirmed by the fact that the width of the $\mathrm{DCA_{xy}}$ distributions of antideuterons and $^3\overline{\mathrm{He}}$ are identical within uncertainties in the same transverse rigidity interval in data, as reported for $0.75 \leq p_{\mathrm{T}}/z < 1$ GeV/c in Figure 4.8. The two distributions are normalized by their integral and fitted with a Gaussian function to highlight their identical width which is dominated by the effect of multiple Coulomb scattering.

For $p_{\mathrm{T}} > 2.5$ GeV/c, the $\mathrm{DCA_{xy}}$ distribution of ^{3}He and ^{3}H are well reproduced using only the template for primary nuclei, which implies that the fractions of secondary ^{3}He and ^{3}H are negligible or below the sensitivity of this measurement. The fraction of primary nuclei is calculated in the range $|\mathrm{DCA_{xy}}| < 0.1$ cm and summarized in Table 4.2. The fractions of

p_{T} (GeV/c)	^{3}He	^{3}H
$1.5-2.0$	$(73\pm1)\%$	$(65\pm1)\%$
$2.0-2.5$	$(94.5\pm0.2)\%$	$(97\pm1)\%$
above 2.5	100%	100%

Table 4.2: The primary fraction calculated for ^{3}He and ^{3}H with its uncertainty.

primary nuclei calculated in different multiplicity intervals are consistent with that calculated for the minimum-bias data sample within uncertainties. Due to the limited number of ^{3}He

candidates, the fit is highly unstable for the lowest multiplicity interval. Therefore, the primary fraction calculated using the minimum-bias data sample is used to correct the spectra in all multiplicity intervals.

4.4.3. Acceptance and efficiency

The product of the acceptance and the efficiency is calculated as the ratio between reconstructed and generated primary nuclei in the simulation with $|\eta_{\mathrm{lab}}| \leq 0.9$, $-1 \leq y_{\mathrm{cms}} < 0$ and $1.5 \leq p_{\mathrm{T}} < 5$ GeV/c for (anti-)^{3}He or $1.5 \leq p_{\mathrm{T}} < 3$ GeV/c for (anti-)^{3}H, respectively. The same track selection criteria that are used for data are applied to the reconstructed particles in the simulation. The acceptance $\times$ efficiency of (anti-)^{3}H and (anti-)^{3}He are shown in Figure 4.9 as a function of p_{T}.

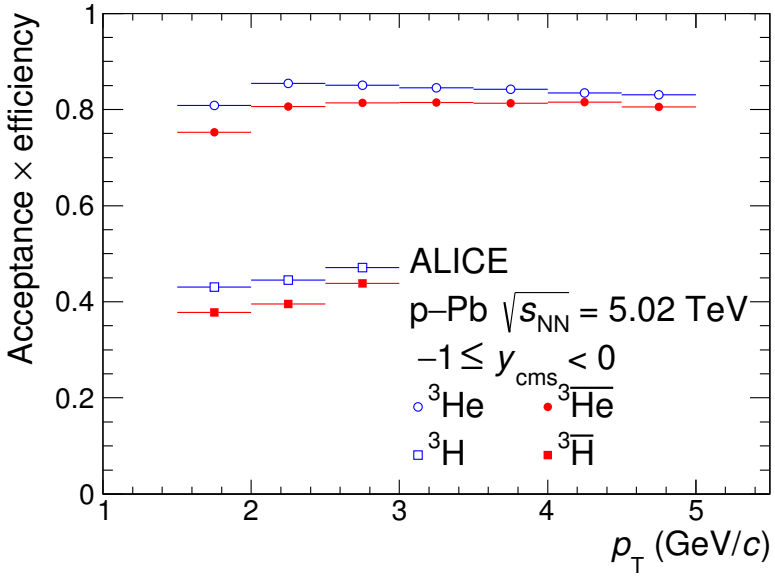

Figure 4.9: The acceptance $\times$ efficiency as a function of p_{T} is shown for $^3\overline{\mathrm{He}}$ and ^{3}He as well as for $^3\overline{\mathrm{H}}$ and ^{3}H.

The efficiency for ^{3}H is lower compared to that of ^{3}He due to the higher number of TPC clusters requested and the additional requirement of a hit in the TOF detector. The latter implies the crossing of additional detector material, i.e. the transition radiation detector (TRD), that is installed between the TPC and the TOF detector. Thus, additional nuclear absorption and multiple Coulomb scattering reduce the TPC–TOF matching efficiency and lead to a lower reconstruction efficiency for ^{3}H. Furthermore, the efficiency and acceptance of the TOF detector has to be taken into account. The efficiency for the antinuclei is reduced compared to the one for the nuclei due to annihilation processes with the beam pipe and the detector material.

4.4.4. Feed-down from hypertriton

The transverse-momentum distribution of (anti-)^{3}He and (anti-)^{3}H contains a contribution from weak decays of the (anti-)hypertriton, ${}^3_\Lambda\mathrm{H} \rightarrow {}^3\mathrm{He} + \pi^-$ and ${}^3_\Lambda\mathrm{H} \rightarrow {}^3\mathrm{H} + \pi^0$ and charged conjugates. This represents the only relevant source of feed-down to (anti-)^{3}He and (anti-)^{3}H at LHC energies. The goal of the analyses described in this thesis is the measurement of primary ^{3}He and ^{3}H, produced at the hadronization stage. For this reason, the feed-down contributions have to be subtracted from the inclusive p_T spectra.

For the estimate of the feed-down, the Monte Carlo sample with injected nuclei is used. Due to the injection, the efficiencies for primary and feed-down nuclei can be evaluated to a good precision but the abundances of the (hyper-)nuclei are not the one realized in nature. Therefore, the ratio of hypertriton-to-helium has to be adjusted by measurements. The fraction of secondary (anti-)^{3}He from decays of (anti-)hypertriton is given by:

$$f_{\text{feed-down}}(p_\mathrm{T}) = \frac{\varepsilon_{\text{feed-down}}(p_\mathrm{T})}{\varepsilon_{^3\mathrm{He}}(p_\mathrm{T})} \cdot \mathrm{BR} \cdot \frac{(\mathrm{d}N/\mathrm{d}y)_{^3_\Lambda\mathrm{H}}}{(\mathrm{d}N/\mathrm{d}y)_{^3\mathrm{He}}} \tag{4.3}$$

where $\varepsilon_{\text{feed-down}}$ and $\varepsilon_{^3\mathrm{He}}$ are the reconstruction efficiency of secondary (anti-)^{3}He from (anti-)hypertriton decays and primary (anti-)^{3}He, respectively. BR denotes the branching ratio of the decay of ${}^3_\Lambda$H into ^{3}He which is about 25% [171]. The (anti-)${}^3_\Lambda$H-to-(anti-)^{3}He yield ratio is obtained by extrapolation of the measurements of this ratio as a function of $\langle \mathrm{d}N_\mathrm{ch}/\mathrm{d}\eta_\mathrm{lab} \rangle$ in Pb–Pb collisions at $\sqrt{s_\mathrm{NN}}$ = 2.76 TeV [172] to the mean charged-particle multiplicity density in p–Pb collisions. The extrapolation is based on the assumption of a linear trend with the charged-particle multiplicity. The (anti-)${}^3_\Lambda$H-to-(anti-)^{3}He yield ratio is found to be about 26% which is compatible with the expectation from Thermal-FIST [101].

For ^{3}H, the feed-down contribution could not be evaluated in the same way because the MC simulation did not contain any ^{3}H from weak decays of hypertriton. Therefore, an upper limit for this contribution is evaluated as half of the feed-down for ^{3}He because the branching ratio of the two-body decay with neutral daughters is half of the one with charged daughters [171]. The ratio of the reconstruction efficiencies for feed-down ^{3}H and primary ^{3}H is assumed to be identical to the corresponding ratio for ^{3}He. The measured p_T spectra of (anti-)^{3}He and (anti-)^{3}H are corrected for the fraction of feed-down from (anti-)hypertriton decays, which is about 3.7% and 1.9%, respectively.

4.5. Systematic uncertainties

The main sources of systematic uncertainties on the (anti-)^{3}He and (anti-)^{3}H yields are summarized in Table 4.3 and discussed in the following. The procedures used for the evaluation of the systematic uncertainties quantify effects due to residual discrepancies between the distributions of the involved track variables in data and MC, as well as due to the limited knowledge about involved quantities, like the hadronic interaction cross section of (anti-)^{3}He and (anti-)^{3}H. The total systematic uncertainty is calculated as the sum in quadrature of the single contributions.

Particle	^{3}He ($^3\overline{\text{He}}$)		^{3}H ($^3\overline{\text{H}}$)	
p_{T} interval (GeV/c)	1.5–2.0	4.5–5.0	1.5–2.0	2.5–3.0
Tracking	4%	5%	5%	5%
PID & contamination	3% (1%)	1%	3% (5%)	20% (30%)
Primary fraction estimation	9% (negl.)	negl.	6% (negl.)	3% (negl.)
Material budget	0.3% (0.5%)	0.2% (0.5%)	2.0% (3.4%)	0.7% (1.3%)
Hadronic cross section	9% (6%)	1% (2%)	2% (8%)	negl. (11%)
Feed-down	1.5%	1.5%	0.8%	0.8%
Total systematic uncertainty	13% (7%)	5% (6%)	9% (12%)	20% (32%)

Table 4.3: Summary of the individual contributions to the total systematic uncertainty in the lowest and highest p_{T} interval measured for ^{3}He and ^{3}H. The values for the antinuclei are shown in parentheses if they differ from the value obtained for the nuclei.

Tracking and PID & contamination uncertainty

The systematic uncertainty related to the track reconstruction contains a contribution coming from the difference of the matching efficiencies between ITS and TPC [for (anti-)^{3}He and (anti-)^{3}H], and between TPC and TOF [for (anti-)^{3}H] in data and MC, as well as a contribution due to the track selection criteria used in the analysis. The latter is estimated by varying the track selection criteria, both in data and for the efficiency calculation. For each transverse momentum interval, the systematic uncertainty is given by the root mean square (RMS) of the distribution of data points obtained from the different track selection variations. The uncertainties due to ITS–TPC and TPC–TOF matching efficiencies are about 1%. The latter is evaluated comparing the TPC–TOF matching efficiencies for charged particles in data and MC. The matching efficiency is defined as the ratio of the number of tracks registered in TOF divided by the number of all tracks. The ITS–TPC matching efficiency is provided centrally by the ALICE data preparation group following a similar strategy. The total tracking system-

atic uncertainty is obtained as the sum in quadrature of each contribution and is about 4-5% for both (anti-)^{3}He and (anti-)^{3}H, independent of p_{T}.

Similarly, the uncertainty from the particle identification is estimated by varying the fitting ranges in the TPC and TOF for the signal extraction as well as for the evaluation of the contamination. The latter has only a minor effect on the uncertainty for (anti-)^{3}He because of the clear separation from other charged particles. In contrast, the effect of the contamination on (anti-)^{3}H is much larger because the separation to other charged particles, which are much more abundant, decreases with increasing p_{T}. The systematic uncertainty on the PID and the contamination is found to be at maximum 3% for ^{3}He and 30% for $^3\overline{\mathrm{H}}$.

The variations of the data points corresponding to different track selection criteria and PID requirements with respect to the default choice are found to be rather independent from one p_{T} interval to another. According to the discussion in [173], Barlow's criterion for the significance of variations is used to ensure that the systematic uncertainties are not governed by the statistical precision. The bin-by-bin independent variations persist after rejecting in each bin the results from variations which differ from the measurement by less than three times the statistical uncertainty on this difference. This uncertainty is calculated by subtracting the statistical uncertainties in quadrature because the two results are obtained from nearly the same data set. This indicates that the degree of correlation with transverse momentum of the tracking and PID uncertainties is to a good approximation negligible. The other uncertainties are instead correlated with transverse momentum.

Primary fraction estimation uncertainty

The systematic uncertainty associated to the fraction of primary nuclei contains three sources: the uncertainty of the template fit, the stability against including more secondaries and the possible bias of the templates used. To estimate the latter contribution, a Gaussian function is used to describe the shape of secondary nuclei while the $\mathrm{DCA_{xy}}$ distribution of antinuclei is used as template for primary nuclei. The parameters of the Gaussian function are obtained by fitting the $\mathrm{DCA_{xy}}$ distribution excluding the signal region ($|\mathrm{DCA_{xy}}| \leq 0.1$ cm). The fraction of primary nuclei is calculated using two methods: in one case, these data-driven templates are used to calculated the fraction in the same way as for the MC templates. In the other case only the Gaussian function is used to calculate the primary fraction $f_{\mathrm{prim}} = 1 - n_{\mathrm{sec}}/n_{\mathrm{total}}$, where n_{sec} is the integral of the Gaussian function and n_{total} is the total number of nuclei measured inside the signal region. For ^{3}He, the primary fraction is calculated in addition using MC templates from secondary ^{3}H scaled in the same way as the deuteron templates. The resulting values for the fraction of primary nuclei obtained from these methods are assumed to follow

a uniform distribution, thus, the uncertainty is calculated as the maximum difference between these values divided by $\sqrt{12}$. The stability of the primary fraction correction against changing the amount of secondary nuclei is tested by varying the DCA selection and, thus, varying the number of secondary nuclei taken into account. The primary fraction should adjust accordingly. This uncertainty is evaluated using an RMS approach. The total uncertainty linked to the primary fraction estimate is given by the sum in quadrature of the three components and is found to be at maximum 9% for ^{3}He and 6% for ^{3}H following an decreasing trend with p_{T}.

Material budget uncertainty

The material budget of the ALICE detector, i.e. the thickness up to the middle of the TPC expressed in units of the radiation length, is known with a relative uncertainty of 4.5% [150] which leads an uncertainty on the reconstruction efficiencies. The impact of this uncertainty on the results is studied by evaluating the relative uncertainty on the reconstruction efficiency using a dedicated MC production with 4.5% higher or lower material budget. These MC productions are anchored to peripheral Pb–Pb collisions due to the unavailability of MC simulations anchored to the p–Pb data. This estimate is reliable assuming that any interference with multiplicity–related (occupancy) effects is negligible. The relative uncertainty $\sigma_{\text{material budget}}$ is calculated via

$$\sigma_{\text{material budget}}(p_{\mathrm{T}}) = \frac{\varepsilon_{\text{max}}(p_{\mathrm{T}}) - \varepsilon_{\text{min}}(p_{\mathrm{T}})}{2 \cdot \varepsilon_{\text{default}}(p_{\mathrm{T}})}, \tag{4.4}$$

where ε_{max} and ε_{min} are the largest and the smallest efficiency obtained in a given p_{T} interval and $\varepsilon_{\text{default}}$ is the efficiency calculated with the default material budget. The uncertainty on the material budget is already chosen such that the values obtained by repeating the material budget determination would be expected to follow a normal distribution with a width given by the uncertainty. Thus, for the uncertainty linked to the material budget, the difference of the efficiencies cannot be divided by $\sqrt{12}$ because this would lead to an underestimation of the uncertainty. The effect is larger for (anti-)^{3}H than for (anti-)^{3}He because of the additional detector material which has to be taken into account due to the TOF requirement. The systematic uncertainty due to the uncertainty on the material budget is small compared to the other contributions to the total uncertainty and accounts for less than 1% for (anti-)^{3}He and at maximum 3.4% for (anti-)^{3}H.

Hadronic interaction cross section uncertainty

In the Monte Carlo simulation used to evaluate the reconstruction efficiency, the propagation of the particles through the ALICE detectors is performed using GEANT3 which does not taken elastic scattering processes into account. In this model, an empirical parametrization of the antideuteron absorption cross section, based on the measurements carried out at the U-70 Serpukhov accelerator [174, 175], is used. In contrast, a Glauber model based on the well-measured total and elastic $\mathrm{p\overline{p}}$ cross section is implemented [176] in GEANT4 [166]. These different implementations allows to estimate the systematic effect due to the incomplete knowledge about hadronic interaction cross section of nuclei as half of the relative difference between the reconstruction efficiency evaluated with GEANT3 and GEANT4. This contribution is found to be smaller than 12% for (anti-)^{3}He and (anti-)^{3}H.

Uncertainty due to the feed-down from weak decays

The last contribution to the systematic uncertainties is the feed-down from weak decays of hypertriton. In section 4.4.4, this contribution is estimated using an extrapolation of the measured ${}^3_\Lambda$H-to-^{3}He yield ratio assuming a linear trend with the charged-particle multiplicity. This extrapolation is repeated after shifting the measured data point at the higher charged-particle multiplicity up and the one at the lower $\langle \mathrm{d}N_{\mathrm{ch}}/\mathrm{d}\eta_{\mathrm{lab}} \rangle$ down by their uncertainties and vice versa. The resulting maximal or minimal ${}^3_\Lambda$H-to-^{3}He yield ratios are used to calculate the relative uncertainty on the feed-down contribution given by the difference of the maximum (6.3%) and the minimum (1.1%) feed-down contribution divided by $\sqrt{12}$. The corresponding contributions to the total systematic uncertainty are 1.5% for ^{3}He and 0.75% for ^{3}H.

4.6. Upper limit on the production of $^4\overline{\mathrm{He}}$

Since $^4\overline{\mathrm{He}}$ nuclei are not produced in spallation reactions of primary particles with the beam pipe or the detector material, an upper limit on the total production yield can be extracted without being affected by the observation of secondary nuclei from these processes. The limit is based on the non-observation of $^4\overline{\mathrm{He}}$ candidates using the same track selection criteria as for $^3\overline{\mathrm{He}}$, except for the maximum distance of closest approach to the primary vertex which have been released to $\mathrm{DCA_{xy}} < 2.4$ cm and $\mathrm{DCA_z} < 3.2$ cm to maximize the reconstruction efficiency. The identification of $^4\overline{\mathrm{He}}$ is based on the time of flight, measured by the TOF detector, and the specific energy loss $\mathrm{d}E/\mathrm{d}x$ in the TPC. These measurements are required to be within $\pm 5\sigma_{\mathrm{TOF}}$ and $\pm 3\sigma_{\mathrm{TPC}}$ around the expected values to ensure a clean sample of candi-

date tracks. The TOF requirement ensures that no $^3\overline{\mathrm{He}}$ tracks are misidentified as $^4\overline{\mathrm{He}}$ above $p/z = 4$ GeV/c where the expected $\mathrm{d}E/\mathrm{d}x$ in the TPC is similar for the two particle species which can be seen in Figure 4.2. The analysis is performed in the transverse momentum interval $2 \leq p_{\mathrm{T}} < 10$ GeV/c. The left panel of Figure 4.10 shows the distribution of the specific

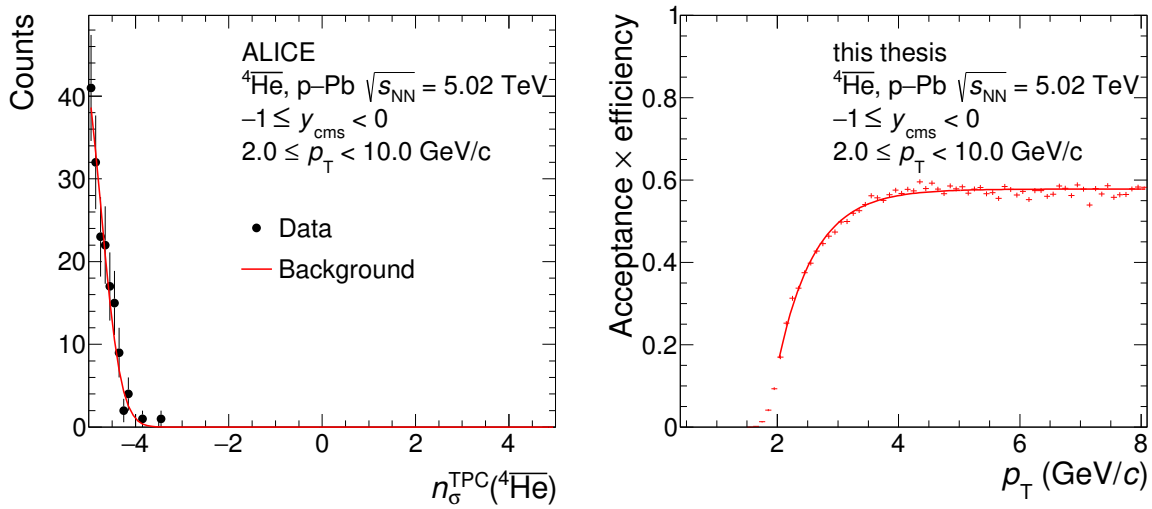

Figure 4.10: The left panel shows the distribution of the specific ionization energy loss ($\mathrm{d}E/\mathrm{d}x$) in the TPC for candidate tracks compared to the expected one for $^4\overline{\mathrm{He}}$, n_σ^{TPC}, in the p_{T} range from 2 to 10 GeV/c. The background is fitted with a Gaussian function (red line). In the right panel, the acceptance × efficiency as a function of p_{T} evaluated using the MC sample with injected nuclei is presented together with the parametrisation used to calculate the efficiency for the full p_{T} interval, 2 to 10 GeV/c.

energy loss compared to the expected one for ^{4}He (n_σ^{TPC}) after the preselection employing the TOF detector. The distribution at $n_\sigma^{\mathrm{TPC}} < -3$, corresponding to $^3\overline{\mathrm{He}}$ candidates, is fitted with a Gaussian function and extrapolated to the signal region, defined as $[-3,3]$. The expected background in the signal region is $1 \cdot 10^{-5}$. The expected background and the non-observation of candidates in the signal region are used to calculate the upper limit at 90% confidence level using the Feldmann-Cousins approach [177]. This procedure allows to construct classical confidence limits in a unified way for upper limits based on a non-observation and two-sided intervals for other cases. It avoids the appearance of unphysical or empty confidence intervals. This behaviour is achieved by employing the ratio of two likelihoods, i.e. the likelihood to observe a value n for a given mean μ of the underlying distribution and the likelihood for the best-fit physically allowed mean μ_{best}, as the order parameter for constructing the confidence intervals. A systematic uncertainty of 20%, similar to the one obtained in Pb–Pb collisions at

$\sqrt{s_{\mathrm{NN}}}$ = 2.76 TeV [178], is assumed. It is taken into account by integrating over a probability density function which parametrizes the knowledge about the uncertainty when calculating the numerator of the likelihood ratio following the procedure described in [179, 180]. For this analysis, a Gaussian function centered at one with a width given by the uncertainty is used.
The resulting upper limit on the raw $^4\overline{\mathrm{He}}$ yield ($N^{\mathrm{upperlimit}}_{2-10\,\mathrm{GeV}/c}$) is corrected for the rapidity interval (Δy) and the number of events selected (N_{events}) as well as the acceptance $\times$ efficiency ($\varepsilon_{^4\mathrm{He}}$). The latter is calculated in p_{T} intervals of 0.1 GeV/c using the MC simulation with injected nuclei. To calculated the average value for $2 \leq p_{\mathrm{T}} < 10$ GeV/c, the acceptance $\times$ efficiency, which is fitted with an ad hoc function, $f(p_{\mathrm{T}}) = a + b\exp(c \cdot p_{\mathrm{T}})$ with $a = 0.5779$, $b = -11.8$ and $c = -1.65$ (GeV/c)$^{-1}$, has to be weighted with the expected shape of the $^4\overline{\mathrm{He}}$ p_{T} distribution. For the latter, a m_{T}-exponential parametrization of the $^4\overline{\mathrm{He}}$ p_{T} spectrum is used,

$$S_{m_{\mathrm{T}}} := \frac{\mathrm{d}N}{\mathrm{d}p_{\mathrm{T}}\,\mathrm{d}y} = N \cdot p_{\mathrm{T}} \cdot \exp\left(-\frac{\sqrt{(p_{\mathrm{T}} \cdot c)^2 + (m \cdot c^2)^2}}{B}\right). \tag{4.5}$$

The parameter values found for (anti-)^{3}He are used, i.e. $N = 5.4 \cdot 10^{-5}$ (GeV/c)$^{-2}$ and $B = 0.595$ GeV. The mass is set equal to the mass of ^{4}He, $m_{^4\mathrm{He}} = 3.73$ GeV/c^2. Since the normalization cancels out when calculating the weighted average, the normalization parameter N is not adjusted to reflect the expected suppression of $^4\overline{\mathrm{He}}$. The weighted average is evaluated using the parametrizations of the spectral shape and the acceptance $\times$ efficiency. The average efficiency is found to be 43.8%.
The obtained value for the upper limit is extrapolated to the full p_{T} range using the m_{T}-exponential parametrization of the $^4\overline{\mathrm{He}}$ p_{T} spectrum via dividing by the following correction factor

$$f = \frac{\int_2^{10} S_{m_{\mathrm{T}}} \mathrm{d}p_{\mathrm{T}}}{\int_0^{10} S_{m_{\mathrm{T}}} \mathrm{d}p_{\mathrm{T}}} = 48.0\%.$$

Thus, the upper limit is given by

$$\frac{\mathrm{d}N}{\mathrm{d}y}^{\mathrm{upperlimit}} = \frac{N^{\mathrm{upperlimit}}_{2-10\,\mathrm{GeV}/c}}{\Delta y \cdot N_{\mathrm{events}} \cdot \varepsilon_{^4\mathrm{He}} \cdot f} = 2.3 \cdot 10^{-8} \tag{4.6}$$

5. Results

The results discussed in this chapter are also published in a recent paper by the ALICE collaboration [168] which was mostly written by the same author as this thesis.

5.1. Transverse-momentum spectra

Final corrections

The production yields of (anti-)^{3}He and (anti-)^{3}H as a function of p_{T} are obtained by correcting the observed number of nuclei candidates after the statistical subtraction of the contamination (N_{obs}) for the fraction of primary nuclei (f_{prim}) and the acceptance times the reconstruction efficiency ($\mathscr{A} \times \varepsilon$) in each p_{T} interval. Afterwards, the feed-down from hypertriton decays is subtracted. The resulting p_{T}-differential yield of produced primary nuclei is divided by the number of selected events (N_{events}), the width of the transverse momentum bins (Δp_{T}) and the rapidity interval (Δy):

$$\frac{\mathrm{d}^2N}{\mathrm{d}y\,\mathrm{d}p_{\mathrm{T}}}(p_{\mathrm{T}}) = \frac{1}{N_{\mathrm{events}}\,\Delta y\,\Delta p_{\mathrm{T}}}\frac{f_{\mathrm{prim}}(p_{\mathrm{T}})\,N_{\mathrm{obs}}(p_{\mathrm{T}})}{(\mathscr{A}\times\varepsilon)(p_{\mathrm{T}})}(1-f_{\text{feed-down}}(p_{\mathrm{T}})) \tag{5.1}$$

To obtain an experiment independent yield, the result has to be corrected for the event and signal loss due to the trigger and the event selection. The procedure for this correction consists of two steps, the track-by-track reweighting with the signal survival efficiency $\varepsilon_{\mathrm{signal}}$ and the recovery of the number of events. The latter can be achieved by reweighting the events with the trigger and event selection efficiency. In this analysis, the trigger and event selection efficiency is evaluated with respect to INEL > 0 events, in which the colliding ions interact via inelastic collisions and at least one charged particle could be measured in $|\eta| < 1$. The efficiency is defined as the ratio of the number of triggered and selected events N_{selected} and the number of events in the event class of interest ($N_{\mathrm{INEL}>0}$)

$$\varepsilon_{\mathrm{INEL}>0} = \frac{N_{\mathrm{selected}}}{N_{\mathrm{INEL}>0}}. \tag{5.2}$$

It is evaluated using the general purpose Monte Carlo simulation described in section 4.4.

Using the same Monte Carlo sample the expected signal survival efficiency after the trigger and event selection is evaluated for protons because the statistical precision of the nuclei signal is not sufficient to perform this investigation. To evaluate the signal survival efficiency, the ratio of the number of generated primary protons before and after the trigger and event selection is calculated.

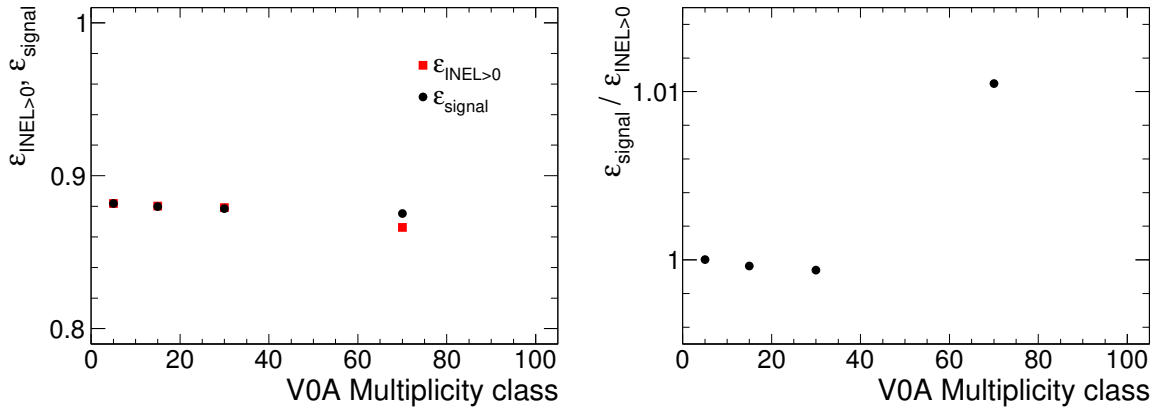

Figure 5.1: In the left panel, the trigger and event selection efficiency is shown as a function of the multiplicity percentile together with the signal survival efficiency. The ratio of the two efficiency is shown in the right panel.

Both, the signal survival efficiency and the trigger and event selection efficiency, as a function of the multiplicity class are summarized in Figure 5.1. About 88% of the signal and events expected for the INEL > 0 event class are selected. In addition, no dependence of the signal survival efficiency on the transverse momentum was found. Since the multiplicity dependence of both efficiencies is very similar and not very pronounced, no track-by-track and event-by-event correction has to be done. Instead, the total observed number of events and the number of analysed events can be corrected by dividing by the corresponding efficiency. This is identical to divide the p_{T}-invariant yields by the ratio of the signal survival efficiency to the trigger and event selection efficiency instead. This ratio is reported in the right panel of Figure 5.1 and deviates from unity at maximum by 1% which is negligible compared to the uncertainties of the reported results. Therefore, no correction has been applied and the reported multiplicity integrated results is the one for the class of INEL > 0 p–Pb collisions at $\sqrt{s_{\mathrm{NN}}} = 5.02$ TeV. The p_{T}-differential yields of (anti-)^{3}He and (anti-)^{3}H measured in INEL > 0 p–Pb collisions at $\sqrt{s_{\mathrm{NN}}} = 5.02$ TeV and the corresponding antiparticle-to-particle ratios are shown in Figure 5.2. The ALICE collaboration has already published the p_{T}-differential yields of (anti-)^{3}He measured in a p–Pb data set collected in 2013 [167] which is smaller and allows for

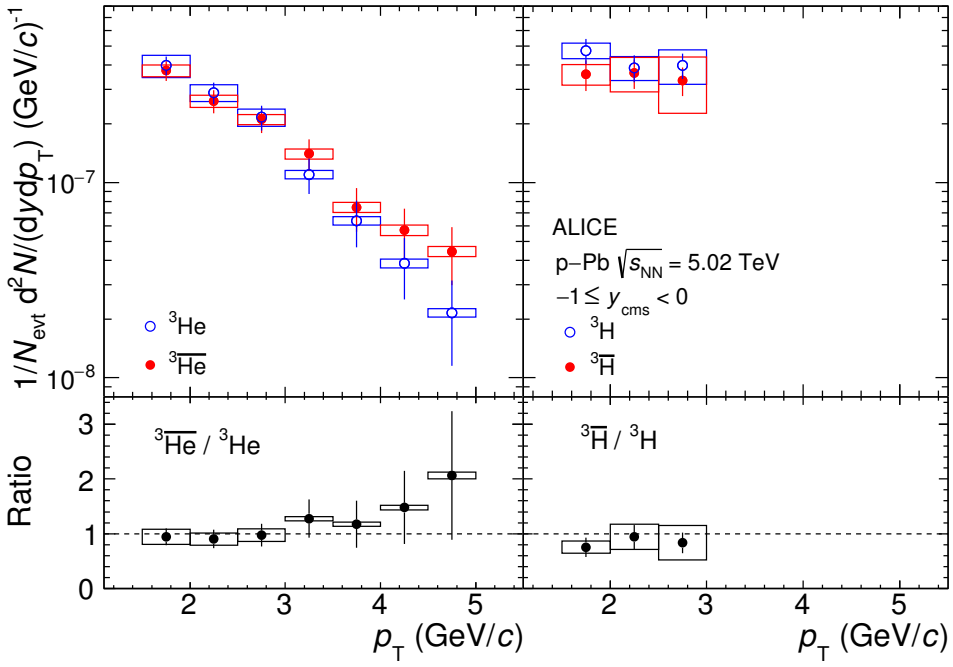

Figure 5.2: The p_T spectra of (anti-)^{3}He and (anti-)^{3}H measured in INEL > 0 p–Pb collisions at $\sqrt{s_{NN}} = 5.02$ TeV are shown in the left and right upper panels, respectively. The bottom panels show the corresponding antiparticle-to-particle yield ratios as a function of p_T. Statistical and systematic uncertainties are indicated by vertical bars and boxes, respectively.

a less precise measurement and no study of the multiplicity dependence. The general analysis strategy in [167] was the same as in the analysis presented in chapter 4 but no correction for the feed-down from weak decays of (anti)$^3_\Lambda$H was performed. In addition, the correction for secondary nuclei from weak decays was not based on template fits but a DCA interval counting procedure. The evaluation of the systematic uncertainties had been refined in the presented analysis compared to the result obtained from the 2013 data set. For the comparison shown in Figure 5.3, the p_T intervals of result presented in this thesis (2016 data set) are adjusted to match the one of the old publication. The two results are compatible within uncertainties. This is clearly visible in the lower panel of Figure 5.3, in which the ratio of the result obtained from the two data sets is shown. To calculate the relative uncertainties on the ratio, the relative statistical and systematic uncertainties of the results are summed in quadrature.

Antiparticle-to-particle yield ratio

For the calculation of the systematic uncertainty on the antiparticle-to-particle yield ratio, the part of the systematic uncertainties correlated between antiparticles and particles, i.e. the

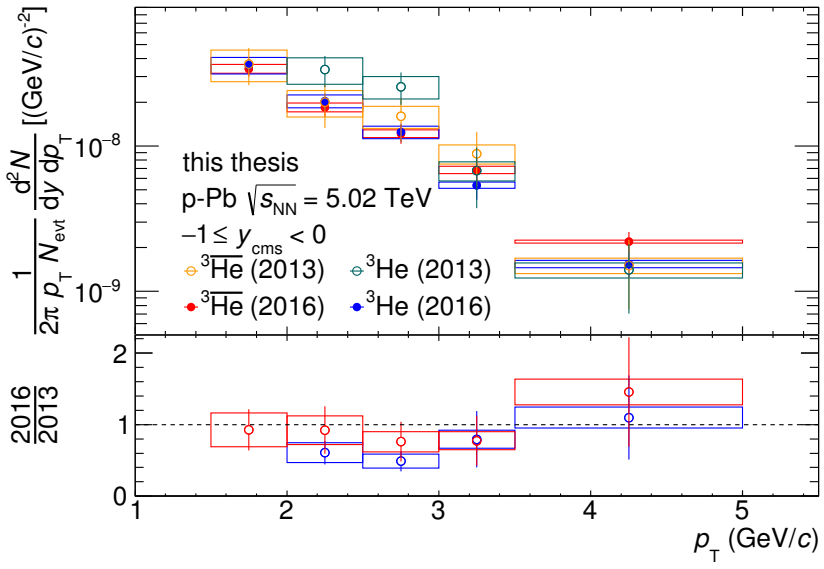

Figure 5.3: The p_T spectra of (anti-)^{3}He obtained from the 2013 [167] and 2016 data set of p–Pb collisions at $\sqrt{s_{NN}} = 5.02$ TeV are shown in the top panel. The ratio of the two results is presented in the bottom panel. Statistical and systematic uncertainties are indicated by vertical bars and boxes, respectively.

uncertainty linked to the tracking, the material budget, and the feed-down, is propagated separately from the remaining systematic uncertainty. The tracking uncertainties and the variations of the spectra corresponding to different track selection criteria are observed to be the very similar for ^{3}He and $^3\overline{\text{He}}$ as well as ^{3}H and $^3\overline{\text{H}}$. Thus, this contribution to the systematic uncertainty is treated as correlated in the calculation of the antiparticle-to-particle yield ratio. The systematic uncertainty related to the material budget is also treated as correlated between particle and antiparticle. This can be explained by the fact that the acceptance $\times$ efficiency for both particles and antiparticles increases for a decreased material budget in the simulation, and vice versa. This can be clearly seen in Figure 5.4, which shows the acceptance $\times$ efficiency for (anti-)^{3}H as a function of p_T obtained from MC simulations of peripheral Pb–Pb collisions with modified material budget as discussed in section 4.5. Since no significant difference between the feed-down contribution for $^3\overline{\text{He}}$ and ^{3}He is observed, the corresponding correction and uncertainty are applied independent of the charge. Hence, this uncertainty is fully correlated between antinuclei and nuclei. The production of secondary particle via spallation affects only the yield of nuclei. Therefore, the corresponding uncertainty is treated as uncorrelated between antiparticle and particle. The uncertainty related to the contamination from other particle species is larger for nuclei compared to antinuclei due to the production of nuclei in spallation reactions. In the case of ^{3}He at low p_T, for example, the ^{3}H contribution

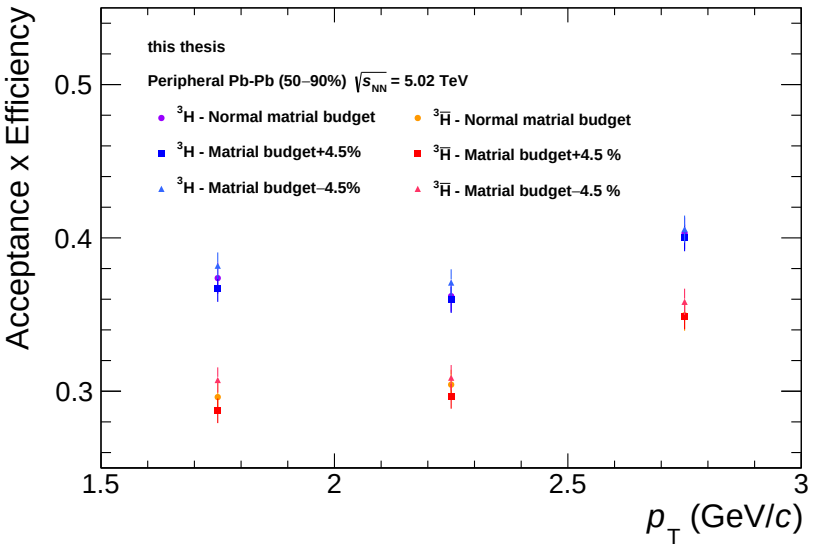

Figure 5.4: The acceptance $\times$ efficiency for (anti-)^{3}H is shown as a function of p_{T} for the nominal material budget of the ALICE detector and for a material budget modified by its uncertainty. These efficiencies obtained from MC simulations of peripheral Pb–Pb (50–90%) collisions at $\sqrt{s_{\text{NN}}} = 5.02$ TeV are used to calculated the uncertainty linked to the material budget uncertainty. The efficiency is observed to decrease with increased material budget in all p_{T} intervals and for ^{3}H and $^3\overline{\text{H}}$. The statistical uncertainties are shown as vertical lines.

is mostly coming from these processes, while the contamination on the anti-^{3}He is negligible. A conservative approach is used and the PID uncertainty is treated as fully uncorrelated in the calculation of the antinuclei-to-nuclei ratio. The hadronic interaction cross section of antinuclei includes contributions from annihilation processes which are not present for nuclei and known only with a larger uncertainty. As a consequence the uncertainty due to the hadronic interaction cross section is at least partially uncorrelated. To avoid to underestimate the impact of this uncertainty on the antinuclei-to-nuclei ratio, it is treated as fully uncorrelated. The full calculation of the systematic uncertainty is summarized in Equation 5.3.

$$\frac{\Delta_{\text{Ratio}}}{\text{Ratio}} = \sqrt{\left(\frac{\Delta_{\text{Antinuclei}}}{\text{Antinuclei}}\right)^2_{\text{uncor}} + \left(\frac{\Delta_{\text{Nuclei}}}{\text{Nuclei}}\right)^2_{\text{uncor}} + \left(\frac{\Delta_{\text{Antinuclei}}}{\text{Antinuclei}} - \frac{\Delta_{\text{Nuclei}}}{\text{Nuclei}}\right)^2_{\text{cor}}} \tag{5.3}$$

The antiparticle-to-particle ratio is consistent with unity within uncertainties which indicates that matter and antimatter are produced in equal amounts in p–Pb collisions at $\sqrt{s_{\text{NN}}} = 5.02$ TeV. This is also observed for deuterons, ^{3}H, and ^{3}He in pp collisions [110, 111], as well as deuterons and ^{3}He in p–Pb and Pb–Pb at different center-of-mass energies at the LHC [167,

111]. This supports a baryochemical potential close to zero included in the grand canonical version of the statistical hadronization models at LHC energies.

In the following, the results are shown for the average of the nuclei and the antinuclei spectra to reduce the effect of statistical fluctuations, if not stated differently.

Multiplicity dependence of the (anti-)^{3}He yield

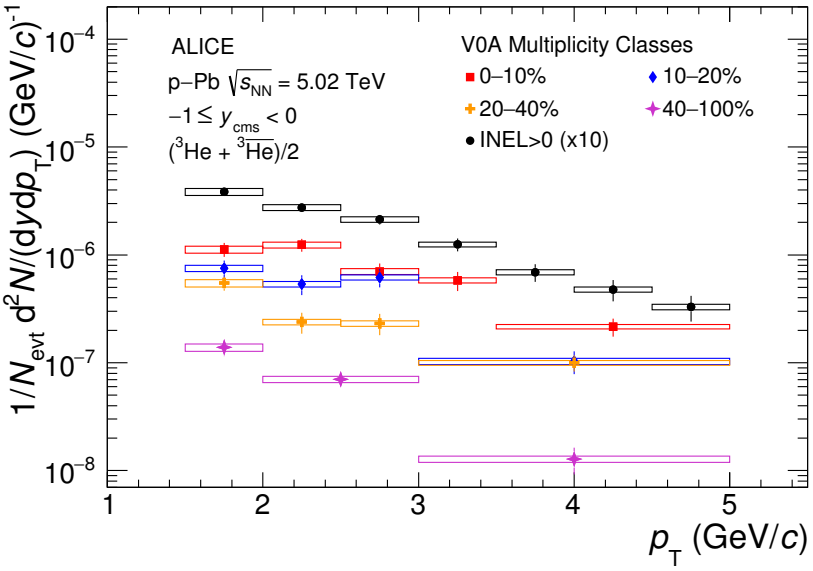

Figure 5.5: The transverse-momentum spectra obtained from the average of ^{3}He and $^3\overline{\text{He}}$ for four different multiplicity classes and INEL > 0 events in p–Pb collisions at $\sqrt{s_{\text{NN}}} = 5.02$ TeV. The p_{T} spectrum obtained in INEL > 0 p–Pb collisions is scaled by a factor of ten for better visibility. Statistical and systematic uncertainties are indicated by vertical bars and boxes, respectively.

The p_{T} spectra of (anti-)^{3}He for different multiplicity classes are summarized in Figure 5.5. The yield of (anti-)^{3}He is observed to increase with the charged-particle multiplicity density $\langle \mathrm{d}N_{\text{ch}}/\mathrm{d}\eta_{\text{lab}} \rangle$. Since the radius of the medium produced in the collision is proportional to $\langle \mathrm{d}N_{\text{ch}}/\mathrm{d}\eta_{\text{lab}} \rangle^{1/3}$, as discussed in section 1.2.3, this increase indicates a dependence of the production mechanism on the size of the medium.

5.2. Total production yield

The p_{T} spectra of (anti-)^{3}He and (anti-)^{3}H have to be extrapolated to the unmeasured p_{T} regions in order to obtain the total production yield ($\mathrm{d}N/\mathrm{d}y$). For the extrapolation, the measured

p_{T} spectra are fitted with the following functional forms: p_{T}-exponential, m_{T}-exponential, Boltzmann, Bose–Einstein, and Fermi–Dirac function. The proper choice of the functional forms used for the fits of hadronic spectra is a difficult topic but in the last decades a set of commonly used functions has been established within the field of research on light nuclei production, in the corresponding Physics Working Group in ALICE and in high-energy physics [111, 167, 170, 181]. The functional forms listed above are the ones of this set of commonly used functions with matched the measured data in the full p_{T} range without going to unphysical parameter values. The extrapolated part of the yield is calculated as the average value obtained by integrating each of these functions outside the measured p_{T} range. The result is added to the integral of the measured spectrum to obtain the total p_{T}-integrated yield. The extrapolated fraction of the integrated yield below and above the measured p_{T} interval is summarized in Table 5.1.

^{3}He	Event class	$p_{\mathrm{T}} < 1.5$ GeV/c	$p_{\mathrm{T}} > 5$ GeV/c
	0–10%	$(39 \pm 5)\%$	$(2.4 \pm 0.8)\%$
	10–20%	$(46 \pm 7)\%$	$(0.8 \pm 0.4)\%$
	20–40%	$(38 \pm 7)\%$	$(2.0 \pm 1.0)\%$
	40–100%	$(55 \pm 8)\%$	$(0.3 \pm 0.2)\%$
	INEL > 0	$(43 \pm 5)\%$	$(1.4 \pm 0.4)\%$
^{3}H	Event class	$p_{\mathrm{T}} < 1.5$ GeV/c	$p_{\mathrm{T}} > 3$ GeV/c
	INEL > 0	$(24 \pm 13)\%$	$(38 \pm 16)\%$

Table 5.1: Fraction of extrapolated yields below and above the measured p_{T} interval relative to the total yield.

For the calculation of the statistical uncertainty on $\mathrm{d}N/\mathrm{d}y$, the transverse-momentum spectra are modified by shifting the data points for different transverse momentum intervals independently to random values distributed following a Gaussian function centered around the measured values and with a width given by the statistical uncertainties. To reduce the computational effort and to avoid issues due to instabilities of repeated fits, the resulting shifted spectra are not fit again to extract the extrapolated yield. Instead, the extrapolated yields at p_{T} below and above the measured range are varied according to a Gaussian distribution centered at the default value with a width given by the uncertainty on the extrapolated yield. This Gaussian sampling procedure for the data points and the extrapolation is repeated 1000 times. The standard deviation of the distribution of the measured total yields determines the statistical uncertainty for each functional form fitted.

For the systematic uncertainty of the total yield, for each of the functional forms the part correlated in p_{T}, i.e. the material budget, the hadronic cross section, feed-down uncertainty, and the uncertainty linked to the estimation of the primary fraction, is treated separately from the remaining uncertainty. The material budget uncertainty is treated as correlated with p_{T} because the efficiency calculated using the MC productions with increased and decreased material budget is observed to shift coherently from one p_{T} interval to another, as reported in Figure 5.4 for (anti-)^{3}H. A similar behaviour is observed for the uncertainty due to the incom-

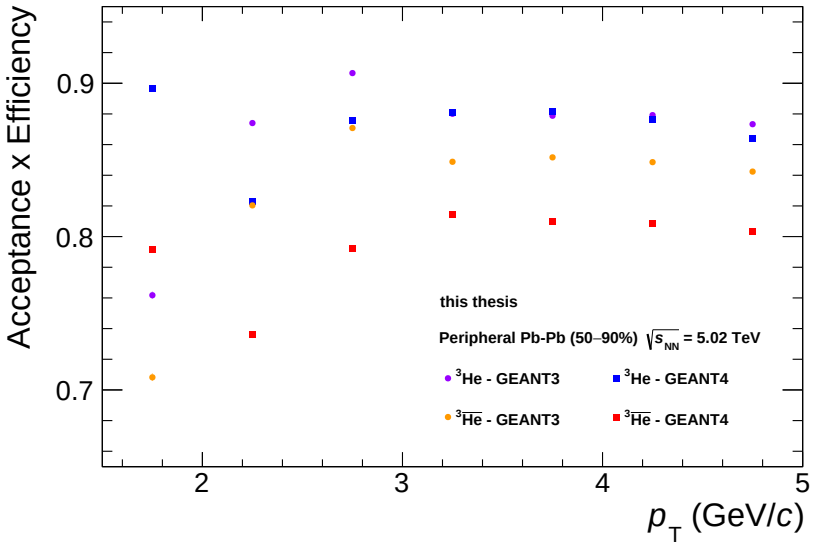

Figure 5.6: The acceptance $\times$ efficiency for (anti-)^{3}He is shown as a function of p_{T} for MC simulations of peripheral Pb–Pb (50–90%) collisions at $\sqrt{s_{\mathrm{NN}}} = 5.02$ TeV with two different transport codes, GEANT3 and GEANT4. These are used to calculated the uncertainty due to the limited knowledge about hadronic interaction cross section of these nuclei. The statistical uncertainties are not visible because they are smaller than the marker size.

plete knowledge about the hadronic interaction cross section for (anti-)^{3}He and (anti-)^{3}H. This can be seen in Figure 5.6, where the acceptance $\times$ efficiency is shown calculated employing MC simulations with GEANT3 and GEANT4. The variation of the DCA window used for the primary fraction estimation is the dominating contribution to the corresponding systematic uncertainty. The yield of (anti-)^{3}He and (anti-)^{3}H are found to vary in the same way in neighboring p_{T} intervals for the same DCA selection. Thus, the systematic uncertainty linked primary fraction estimation is treated as correlated with p_{T}. Since no significant difference between the feed-down contribution from one p_{T} interval to another is observed for (anti-)^{3}He and (anti-)^{3}H, the corresponding uncertainty is considered to be correlated with p_{T}. The correlated part of the systematic uncertainty is evaluated as the average difference between the

default value and the yield obtained by shifting the measured points up or down by the correlated part of the systematic uncertainties. The remaining part of the systematic uncertainty, i.e. the uncertainty linked to the tracking as well as the PID and contamination, is treated as fully uncorrelated considering the negligible degree of correlation, as discussed in section 4.5. Therefore, the Gaussian sampling procedure is also used to evaluate the contribution of these sources to the systematic uncertainty on the total p_{T}-integrated yield. The systematic uncertainty on $\mathrm{d}N/\mathrm{d}y$ for each functional form is given by the sum in quadrature of the uncorrelated and the correlated uncertainty. To obtain the total systematic uncertainty, the average of the contributions from the different functional forms is calculated and added in quadrature to the uncertainty given by the spread of the values obtained with the different functional forms. The latter is calculated as the difference of the maximum and the minimum yield divided by $\sqrt{12}$. To cross-check the stability of the systematic uncertainty on the integrated yield, the calculation is repeating assuming that all sources of uncertainty are either uncorrelated or correlated. Since the uncertainty linked to the spread of the functional forms causes about 50% of the total uncertainty, no significant differences between the uncertainties obtained from the three assumptions are found.

5.3. Mean transverse momentum

Based on the extrapolation, the mean transverse momentum $\langle p_{\mathrm{T}} \rangle$ of (anti-)^{3}He is calculated for the different multiplicity classes. The statistical and systematic uncertainties on $\langle p_{\mathrm{T}} \rangle$ are calculated in the same way as for the integrated yield. The results are shown in Figure 5.7 and compared with the $\langle p_{\mathrm{T}} \rangle$ measured in pp collisions at $\sqrt{s} = 7$ TeV [110] and in Pb–Pb collisions at $\sqrt{s_{\mathrm{NN}}} = 2.76$ [111]. As for pions, kaons and protons [76], no big change of $\langle p_{\mathrm{T}} \rangle$ with increasing collision energy within the LHC energies is expected. The $\langle p_{\mathrm{T}} \rangle$ measured in p–Pb collisions increases with the mean charged-particle multiplicity density, connecting the measured results in pp and Pb–Pb collisions in a smooth way. This indicates a hardening of the p_{T} spectra with increasing mean charged-particle multiplicity density, which might be caused by production in jets [182] or by collective expansion effects [170]. The latter would also result in a shift of the maximum of the p_{T} distribution, which cannot be observed in the present measurements due to the limited statistical precision.

If the system evolves hydrodynamically, the mean transverse momentum of different particle species should follow a mass ordering, as a result of the radial flow. In Figure 5.8, the $\langle p_{\mathrm{T}} \rangle$ as a function of the particle mass is shown for different mean charged-particle multiplicity densities. For similar $\langle \mathrm{d}N_{\mathrm{ch}}/\mathrm{d}\eta_{\mathrm{lab}} \rangle$, a clear mass ordering is observed separately for the

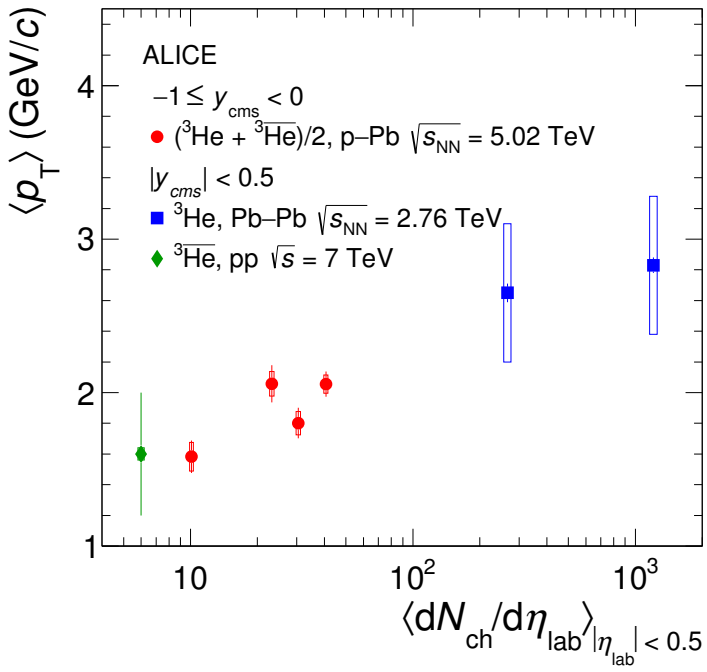

Figure 5.7: The mean transverse momentum of (anti-)^{3}He is shown as a function of the mean charged-particle multiplicity density in p–Pb collisions at $\sqrt{s_{\mathrm{NN}}} = 5.02$ TeV. The published results from pp [110] and Pb–Pb [111] collisions are shown with diamonds and rectangles, respectively. Statistical and systematic uncertainties are indicated by vertical bars and boxes, respectively.

different particle species up to Ω and for the nuclei. The measurements for the nuclei prefer a scaling which does not follow the same linear trend as the results for π, K, p, Λ [170], Ξ, and Ω [183].

5.4. Ratio to protons

The ratio of the integrated yields of (anti-)^{3}He to those of (anti-)protons (^{3}He/p) is calculated for the four multiplicity classes used in this analysis, while the yield ratio of (anti-)^{3}H to (anti-)protons (^{3}H/p) is calculated for INEL > 0 events. The p_{T}-integrated average yields of antiprotons and protons are taken from [170]. The relative statistical and systematic uncertainties on the yield ratio are calculated by adding the the corresponding relative uncertainties on the yields in quadrature.

The ^{3}He/p yield ratios are shown as a function of the charged-particle multiplicity density in Figure 5.9 together with the corresponding results from pp collisions at $\sqrt{s} = 7$ TeV [110] and from Pb–Pb collisions at $\sqrt{s_{\mathrm{NN}}} = 2.76$ TeV [111]. The yield ratios at the same charged-

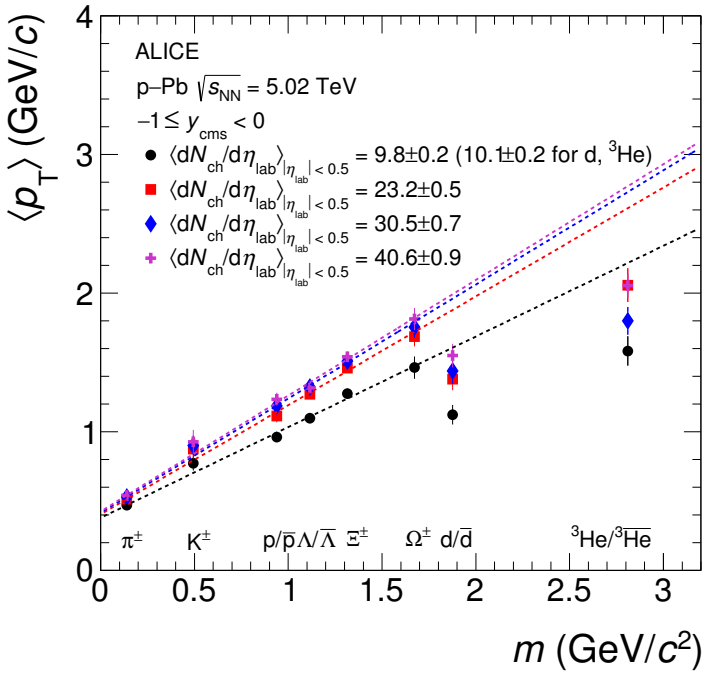

Figure 5.8: The mean transverse momentum measured in p–Pb collisions at $\sqrt{s_{\mathrm{NN}}} = 5.02$ TeV is shown as a function of the particle mass for different mean charged-particle multiplicity densities. The linear scaling with the mass observed for π, K, p, Λ [170], Ξ, and Ω [183] is indicated by dashed lines. The deuteron $\langle p_{\mathrm{T}} \rangle$ is taken from [167]. Statistical and systematic uncertainties are indicated by vertical bars and boxes, respectively.

particle multiplicity are expected to be constant as a function of the collision energy within the range of typical LHC energies as observed for the d/p ratio. For Pb–Pb collisions, this can be understood from the SHM because the yield ratios are proportional to $\exp(\mu_B/T_{\mathrm{chem}})$ which is constant for LHC energies [46]. The data are compared to the expectation from the Canonical Statistical Model (CSM), called Thermal-FIST [101], and two coalescence calculations [121]. The trend observed in the data can be qualitatively reproduced over the full multiplicity range using the CSM approach, which is based on the exact conservation of charges, i.e. electrical charge, baryon and strangeness number, across the correlation volume V_{c} [101]. The predictions were calculated using a chemical freeze-out temperature $T = 155$ MeV and a correlation volume extending across one unit ($V_{\mathrm{c}} = \mathrm{d}V/\mathrm{d}y$) or three units ($V_{\mathrm{c}} = 3\,\mathrm{d}V/\mathrm{d}y$) of rapidity. The temperature value is constrained by the ^{3}He/p yield ratio measured in Pb–Pb collisions [111]. It is very close to the temperature which was found for the grand canonical SHM [46] fit of the integrated yields of different particle species measured in most central Pb–Pb collisions by ALICE. For the mean charged-particle multiplicity density region covered by the results

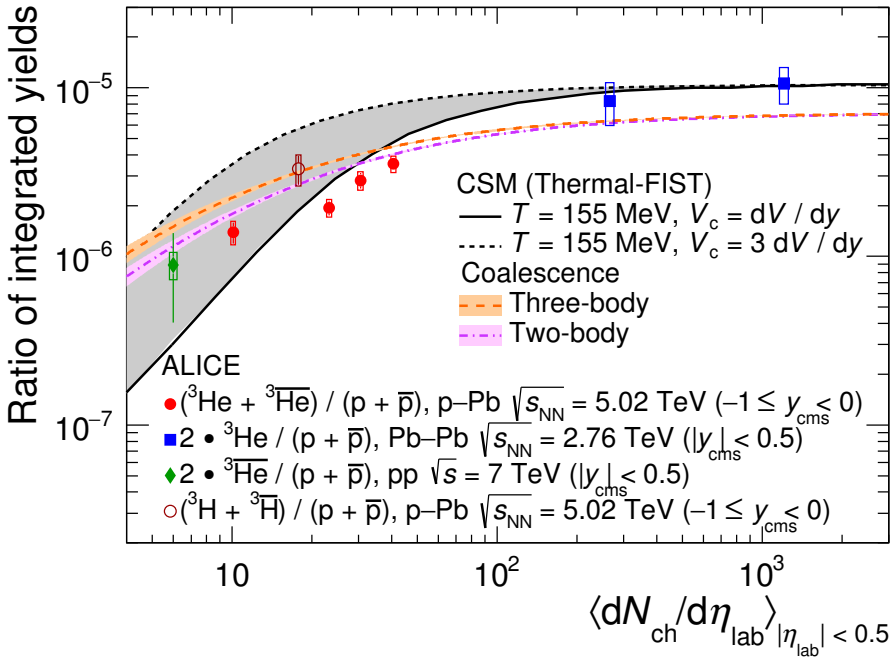

Figure 5.9: ^{3}He/p yield ratio in pp, p–Pb, and Pb–Pb collisions [110, 111] as a function of the mean charged-particle multiplicity density, together with the ^{3}H/p yield ratio. Statistical and systematic uncertainties are indicated by vertical bars and boxes, respectively. The expectations for the canonical statistical hadronization model (Thermal-FIST [101]) and two coalescence approaches [121] are shown. For the thermal model, calculations with two different values of the correlation volume are displayed. The uncertainties of the coalescence calculations, which are due to the theoretical uncertainties on the emission source radius, are denoted as shaded bands.

obtained in Pb–Pb collisions, the CSM reaches the grand canonical limit and, thus, matches the version of the SHM using the grand canonical ensemble.

The ^{3}He/p and ^{3}H/p yield ratios measured in p–Pb collisions, which cover the gap in multiplicity between the existing measurements in pp and Pb–Pb collisions, favour a small correlation volume $V_c = \text{d}V/\text{d}y$, while the ratios of the deuteron to the proton yield measured in pp collisions are more compatible with a larger correlation volume [101]. The ^{3}He/p yield ratio as a function of the mean charged-particle multiplicity density has a similar trend as the d/p ratio shown in Figure 2.3. However, the increase between the pp and the Pb–Pb results is about a factor of 3–4 larger for ^{3}He/p than for d/p [167]. The simplified version of the CSM presented in this paper, which assumes a constant freeze-out temperature as a function of the system size, shows some tensions with data for the p/π and K/π yield ratios and fails to describe the measured ϕ/π yield ratio [123].

With increasing charged-particle multiplicity density, the number of protons and neutrons produced in the collision is also increasing. The more protons and neutrons are available, the more likely nucleons can be close enough in phase space to form a nucleus. Therefore, an increasing trend for the ^{3}He/p yield ratio as a function of the charged-particle multiplicity density is expected in the coalescence approach. The measured ratio is compared to coalescence predictions [121] which take the radii of the source and the emitted nucleus into account. The expectations for three-body coalescence, where the nuclei are directly produced from protons and neutrons, as well as for two-body coalescence, where an intermediate formation of a deuteron is needed, are shown. For both coalescence approaches, the theoretical uncertainties are given by the uncertainty on the emission source radius. Both calculations are in overall agreement with the data at low and intermediate multiplicities while they are systematically below the experimental results for higher multiplicities. The measured ^{3}He/p yield ratio shows a slight preference for the two-body coalescence approach, even though this is not yet conclusive due to the uncertainties on both the data and the theoretical description.

5.5. Coalescence parameter

The coalescence parameter B_3 is calculated as

$$B_3 = \frac{S_{^3\mathrm{He}/^3\mathrm{H}}}{S_\mathrm{p}^3}, \tag{5.4}$$

where $S_i = 1/(2\pi p_\mathrm{T})\,\mathrm{d}^2N_i/(\mathrm{d}y\mathrm{d}p_\mathrm{T})$ is the invariant yield of the particle $i = {}^3$He, ^{3}H or protons. The statistical and systematic uncertainties of B_3 are calculated following the usual propagation of uncertainties assuming that statistical and systematic uncertainties of the invariant yields of protons and ^{3}He or ^{3}H are uncorrelated,

$$\frac{\Delta B_3}{B_3} = \sqrt{\left(\frac{\Delta S_{^3\mathrm{He}/^3\mathrm{H}}}{S_{^3\mathrm{He}/^3\mathrm{H}}}\right)^2 + \left(\frac{3\Delta S_\mathrm{p}^3}{S_\mathrm{p}^3}\right)^2}. \tag{5.5}$$

The resulting coalescence parameter values are shown in Figure 5.10 as a function of the transverse momentum per nucleon.

^{3}H-to-^{3}He yield ratio

The proton spectrum cancels out in the calculation of ratio between the coalescence parameter obtained from the production yields of (anti-)^{3}H and (anti-)^{3}He if the neutron production

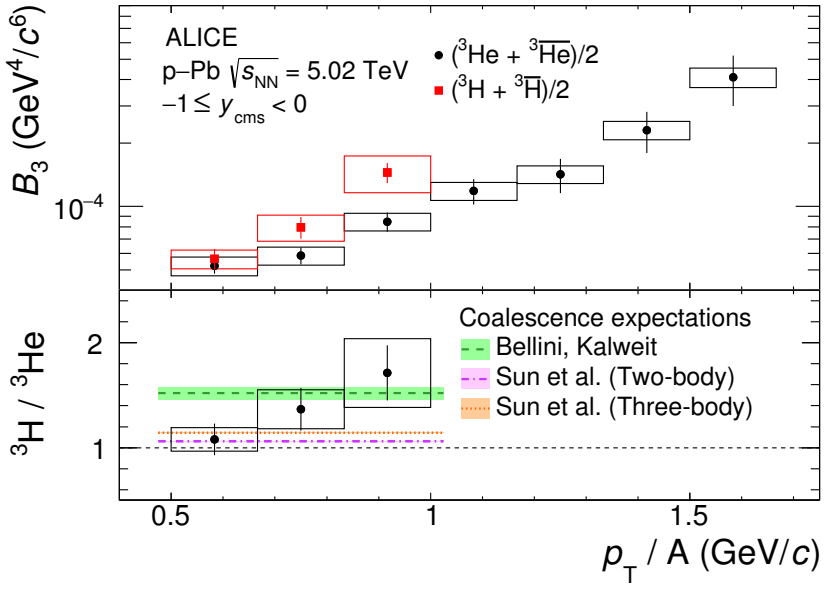

Figure 5.10: In the top panel, the coalescence parameter B_3 calculated for the average of INEL > 0 ^{3}He and $^3\overline{\text{He}}$ yields is shown together with the corresponding result (anti-)^{3}H. The bottom panel shows the ^{3}H/^{3}He yield ratio together with the expectation values from three coalescence approaches [106, 121]. The uncertainties of the coalescence calculations, which are due to the theoretical uncertainties on the emission source radius, are denoted as shaded bands. Statistical and systematic uncertainties are indicated by vertical bars and boxes, respectively.

yields are equal to the corresponding proton yields. Thus, the B_3 ratio is equal to the ratio of the yields of (anti-)^{3}H and (anti-)^{3}He (^{3}H/^{3}He) which is shown in the bottom panel of Figure 5.10. Its systematic uncertainty is calculated as the sum in quadrature of the uncertainties of the yields ignoring possible correlations of the uncertainties. The ^{3}H/^{3}He yield ratio is expected to be consistent with unity according to a simple coalescence approach. In more advanced coalescence calculations, that take into account the size of the emitting source and the nucleus, this ratio is expected to be above unity [106, 121]. The difference in the coalescence expectations is mainly due to a different parametrization of the source radius as a function of the mean charged-particle multiplicity density which is reported in Figure 5.11. Sun, Ko and Dönigus use a $\langle \mathrm{d}N_{\mathrm{ch}}/\mathrm{d}\eta_{\mathrm{lab}} \rangle$ dependence of the source size which is calculated based on the dependence of the number of protons measured in pp and p–Pb collisions at different collision energies and the kinetic freeze-out temperature obtained from Blast-Wave fits to the charged-particle spectra in Pb–Pb collisions at $\sqrt{s_{\mathrm{NN}}} = 2.76$ TeV reported by the ALICE collaboration. The obtained parametrization is compatible with the Hanbury Brown-Twiss (HBT) radius for a pair transverse momentum, k_{T}, between 0.2 and 0.3 GeV/c measured in p–Pb collisions at

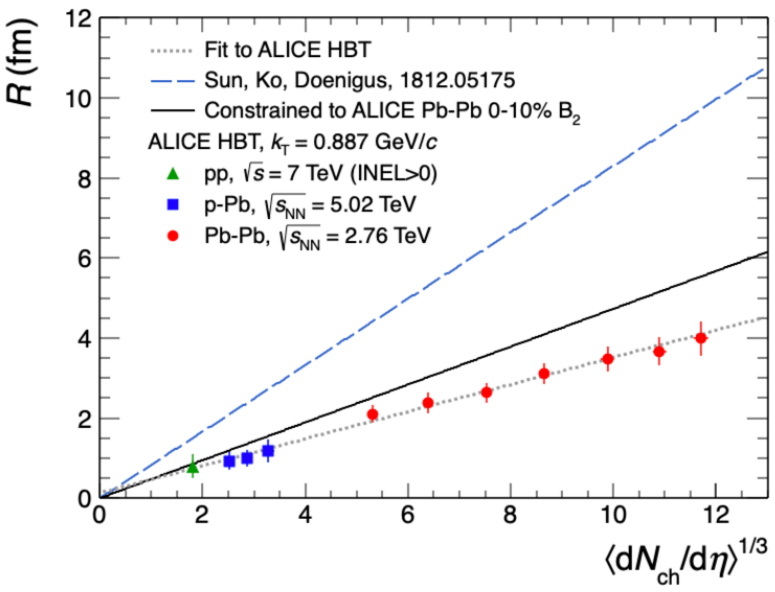

Figure 5.11: The comparison of the parametrizations of the source size R as a function of $\langle \mathrm{d}N_{\mathrm{ch}}/\mathrm{d}\eta_{\mathrm{lab}} \rangle^{1/3}$ used in [121] (blue dashed line) and [106] (black and black dotted lines) is shown together with the HBT results provided by the ALICE collaboration. This picture is taken from [106].

$\sqrt{s_{\mathrm{NN}}} = 5.02$ TeV by the ATLAS collaboration. The other theoretical calculation by Bellini and Kalweit makes use of two different parametrisations. On the one hand, the HBT radius at $k_{\mathrm{T}} = 0.887$ GeV/c in pp, p–Pb and Pb–Pb collisions measured by the ALICE collaboration is used. On the other hand, a parametrisation is obtained from the coalescence parameter B_2, calculated from the measured deuteron and proton yields, provided by the ALICE collaboration. The difference between these two parametrizations causes the larger uncertainty for the corresponding theoretical prediction. Another source of differences between the two coalescence approaches is the use of slightly different values for the radius of ^{3}H. In [121], the matter radius $r_{^3\mathrm{H}} = 1.59$ fm is used, while the corresponding value in [106] is

$$r_{^3\mathrm{H}} = \sqrt{3/4 \cdot (A-1)/A} \cdot r_A^{^3\mathrm{H}} = \sqrt{1/2} \cdot r_A^{^3\mathrm{H}} = 1.52 \text{ fm}, \tag{5.6}$$

where $r_A^{^3\mathrm{H}}$ denotes the characteristic-size parameter of the ground-state wave-function.

A fit to the measured ^{3}H/^{3}He yield ratio with a constant function results in 1.27 ± 0.11 which deviates from unity by 2.5σ but from the coalescence calculations only by $1.15 - 2\sigma$. Thus, the ratio is found to be in slightly better agreement with the coalescence expectations than with unity. In the SHM approach, the ^{3}H/^{3}He yield ratio is expected to be consistent with unity. Therefore, this observable is potentially useful not only to discriminate between

different implementations of the coalescence approach but also with respect to SHMs. Since all the theoretical calculations are based on p_{T} independent source radii, the increase of the ^{3}H/^{3}He yield ratio with p_{T}/A observed in data is not described. A possible extension of these theoretical description would be to incorporate the transverse-momentum dependence observed for the HBT radii [94].

Transverse momentum dependence of B_3

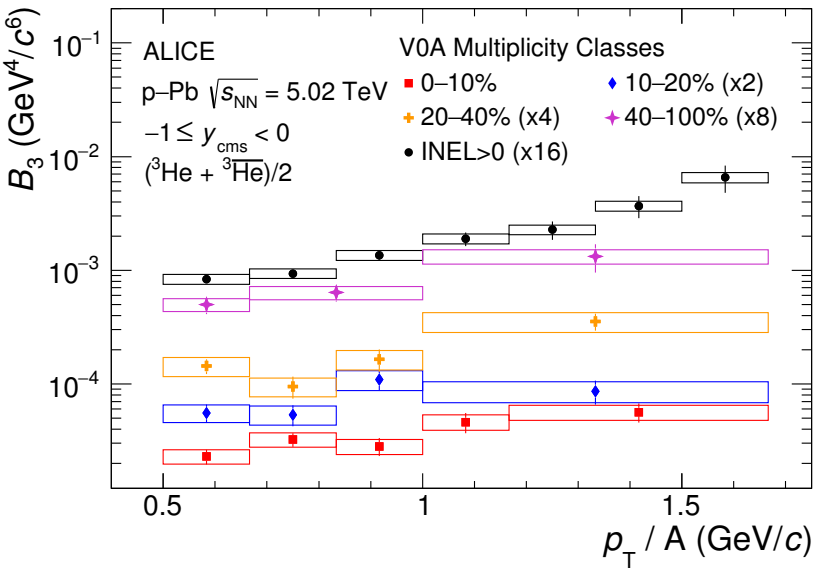

Figure 5.12: The coalescence parameter B_3 calculated with the average of ^{3}He and $^3\overline{\mathrm{He}}$ is shown for four multiplicity classes together with the INEL > 0 result. For better visibility, the distributions are scaled by different factors. Statistical and systematic uncertainties are indicated by vertical bars and boxes, respectively.

The coalescence parameter B_3 for ^{3}He calculated for the four multiplicity classes analyzed is shown in Figure 5.12 as a function of the transverse momentum per nucleon. A rising trend with p_{T}/A is observed in all multiplicity classes, which is in contrast to the expectations of the simple coalescence approach which predicts a constant B_3. The coalescence parameter is found to be increasing with p_{T} by a factor of 2 to 3 for the different multiplicity intervals. The INEL > 0 result shows an even more pronounced increase with the transverse momentum, i.e. about a factor of 8. This behaviour can be partially understood as the effect coming from the hardening of the proton spectra with increasing mean charged-particle multiplicity density as discussed in [184]. According to this, the coalescence parameter obtained in a wide charged-particle multiplicity interval exhibits an increasing trend with p_{T}/A even though the

coalescence parameter is constant in each of its small subintervals. As discussed in section 2.2, the coalescence parameter is defined as

$$B_A = \frac{S_A}{S_{\mathrm{p}}^A}, \tag{5.7}$$

where $S_{A/\mathrm{p}} = 1/(2\pi p_{\mathrm{T}})\,\mathrm{d}^2N_{A/\mathrm{p}}/(\mathrm{d}y\mathrm{d}p_{\mathrm{T}})$ is the invariant yield of the nuclei with mass number A or protons, respectively. The coalescence parameter in a given multiplicity interval, B_A^*, can be expressed via the weighted average of the invariant yields of the protons and the nuclei in the its subintervals, $S_{A/\mathrm{p},i}$,

$$B_A^* = \frac{\sum_{i=1}^{n}(N_i/N)S_{\mathrm{A},i}}{(\sum_{i=1}^{n}(N_i/N)S_{\mathrm{p},i})^A}. \tag{5.8}$$

The weights (N_i/N) are given by the fraction of events in the i-th charged-particle multiplicity subinterval. These nuclei yields can be expressed via the proton yield and the coalescence parameter, B_A^i, calculated for the respective subinterval employing the definition of the coalescence parameter:

$$B_A^* = \frac{\sum_{i=1}^{n}(N_i/N)B_A^i\,S_{\mathrm{p},i}^A}{(\sum_{i=1}^{n}(N_i/N)S_{\mathrm{p},i})^A} \tag{5.9}$$

Due to the hardening of the proton spectra with multiplicity, the p_{T} shape of the numerator differs from the one of the denominator because the average of the proton spectra to the power of A is not the same as the average proton spectrum to the power of A. To test this effect in the presented measurements, the coalescence parameters in the analysed multiplicity intervals are recalculated as

$$B_3^* = \frac{\sum_{i=0}^{n}(N_i/N)B_3^iS_{\mathrm{p},i}^3}{\left(\sum_{i=0}^{n}(N_i/N)S_{\mathrm{p},i}\right)^3}, \tag{5.10}$$

where the charged-particle multiplicity subintervals are chosen with a width of 1%. The values of B_3^i are assumed to be constant with p_{T}/A and are obtained by parametrizing the multiplicity dependence of the measured B_3 observed in the first p_{T}/A interval with a linear function. To estimate the uncertainty on the B_3^i, the measured B_3 values are sampled following a Gaussian function with a mean equal to the measured value and a width given by the uncertainty. The resulting distribution of the coalescence parameter as a function of the multiplicity class is fitted with a linear function which is used to calculate a new set of B_3^i values. The distribution

of B_3^i values, obtained in each multiplicity subinterval by repeating this procedure thousand times, is fitted with a Gaussian function and the width is used as the uncertainty on B_3^i.

The proton spectra in the same multiplicity subintervals are obtained by interpolation of the measured invariant production yields of protons. For this interpolation, the Blast-Wave parameters reported in [170] are parametrized as a function of the multiplicity percentile. As discussed in section 1.2.3, the Blast-Wave model can be expressed as

$$E\frac{\mathrm{d}^3N}{\mathrm{d}^3\mathbf{p}} \approx \int_0^R m_\mathrm{T} I_0\left(\frac{p_\mathrm{T}\sinh(\rho)}{T_\mathrm{kin}}\right) K_1\left(\frac{m_\mathrm{T}\cosh(\rho)}{T_\mathrm{kin}}\right) r\mathrm{d}r, \tag{5.11}$$

where $m_\mathrm{T} = \sqrt{m^2 + p_\mathrm{T}^2}$ is the transverse mass and I_0 and K_1 are the modified Bessel functions. The velocity profile ρ can be expressed as

$$\rho = \tanh^{-1}\left[\beta_\mathrm{s}\left(\frac{r}{R}\right)^n\right], \tag{5.12}$$

where β_s denotes the transverse expansion velocity at the surface and n is the exponent of the velocity profile. The radial distance in the transverse plane is expressed as r and R is the radius of the medium. The actual Blast-Wave parameter β_s is linked to the mean transverse expansion velocity $\langle\beta_\mathrm{T}\rangle$ given in the paper via the following equation:

$$\langle\beta_\mathrm{T}\rangle = \frac{2}{2+n}\beta_\mathrm{s} \tag{5.13}$$

The normalization, which is not reported in [170], is obtained by fitting the Blast-Wave function to the measured proton spectra keeping the other parameters fixed. In Figure 5.13, the dependence of the Blast-Wave parameters on the multiplicity percentile is shown and parametrized with functional forms which ensure a monotonous behaviour. The corresponding parametrizations are used to create Blast-Wave functions corresponding to the proton spectra in the subintervals of 1% width. The uncertainties on the interpolated spectra are set equal to the uncertainties of the measured proton spectra, which are in the order of 10% at $p_\mathrm{T} = 0.3$ GeV/c to 20% at $p_\mathrm{T} = 4$ GeV/c. The uncertainties on the re-calculated coalescence parameter B_3^* are obtained by propagating the uncertainties on the interpolated proton spectra and on B_3^i. As shown in Figure 5.14, the resulting coalescence parameter B_3^* increases by less than factor of two while the measured B_3 increases by a factor of eight. This clearly indicates that a constant coalescence parameter with p_T/A is too simplistic and cannot explain the observed increase in the measured B_3. The presented results clearly imply an increasing trend of B_3 also in charged-particle multiplicity intervals of 1% width. In addition, the comparison between

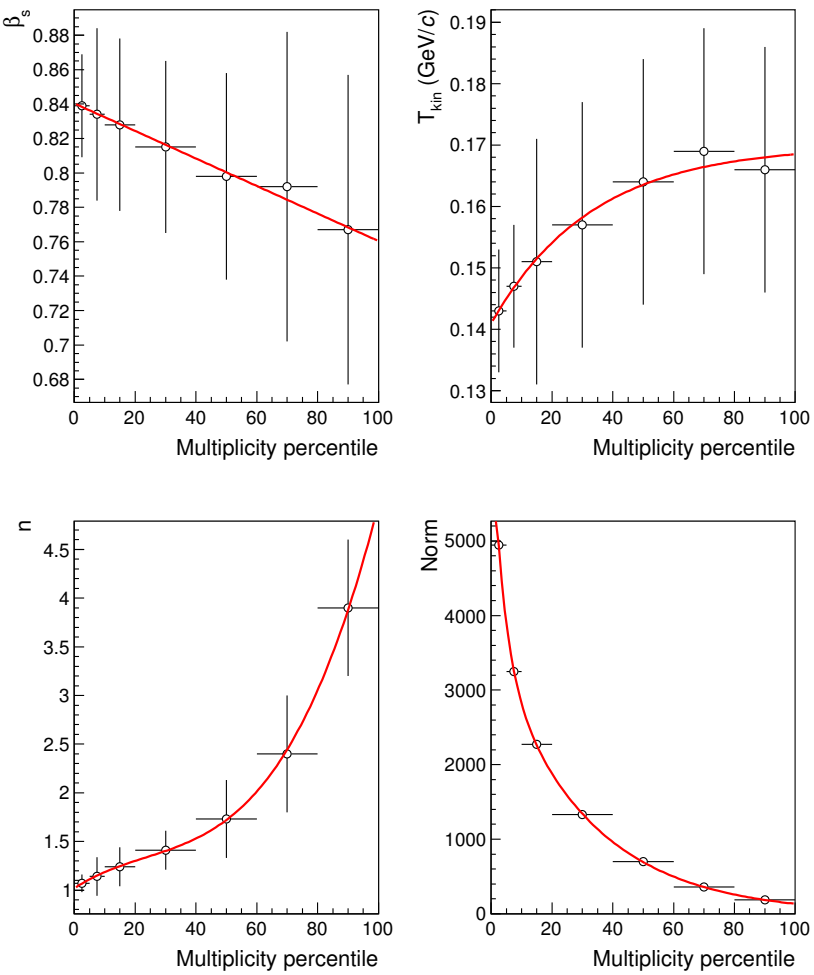

Figure 5.13: The Blast-Wave parameters reported in [170] are parametrized as a function of the multiplicity percentile.

the recalculated coalescence parameters and the measured results for each of the charged-particle multiplicity intervals is reported in Figure 5.15. The recalculated values are found to be constant with p_{T} in most of the charged-particle multiplicity intervals except of the last interval (40–100%), in which B_3^* exhibits a similar increase as observed in data. In (0-10)%, the difference in the shape of B_3^* and B_3 is more pronounced indicating that the effect could be stronger for larger system sizes than for smaller ones.

The increasing coalescence probability with increasing p_{T} implies stronger correlation of nucleons in momentum and space at higher p_{T}. This might be connected to light nuclei production in jets or the transverse-momentum dependence of the source radius as observed for HBT radii [94]. A clear answer to the question about the origin of the increasing trend with

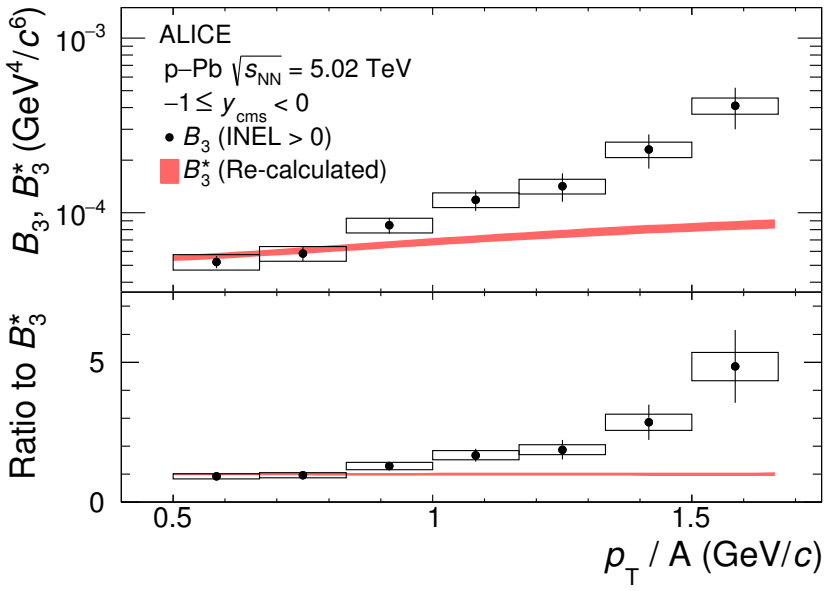

Figure 5.14: The coalescence parameter B_3 obtained in INEL > 0 p–Pb collisions is compared to the recalculated coalescence parameter B_3^* which is obtained assuming a flat B_3 in its multiplicity subintervals. B_3^* indicates the expected p_T dependence caused by the hardening of the proton spectra as a function of the multiplicity. Statistical and systematic uncertainties are drawn as vertical bars and boxes, respectively.

p_T/A observed for the different multiplicity classes requires a larger data set which would allow for more differential studies. In addition, more sophisticated theoretical descriptions would be needed which provide results for the coalescence parameter obtained in similar multiplicity intervals as in data instead of providing values for a given charged-particle multiplicity density and which incorporate a p_T-dependent source radius.

Multiplicity dependence of B_3

The multiplicity dependence of B_3 is compared to theoretical model calculations for $p_T/A = 0.73$ GeV/c and $p_T/A = 0.90$ GeV/c in Figure 5.16. The data point shown are the ones belonging to the p_T interval containing the respective p_T/A value used for the theoretical calculations. The B_3 values for the measurements in pp, p–Pb, and Pb–Pb [110, 111] collisions are shown as a function of the mean charged-particle multiplicity density. In addition, the expected values for the coalescence approach taken from [106] are shown for two different parametrization of the source radius as a function of the mean charged-particle multiplicity density. For one of the parametrizations, the ALICE HBT radii measurements are used, while the other one is constrained by the ALICE B_2 measurements in 0–10% central Pb–Pb colli-

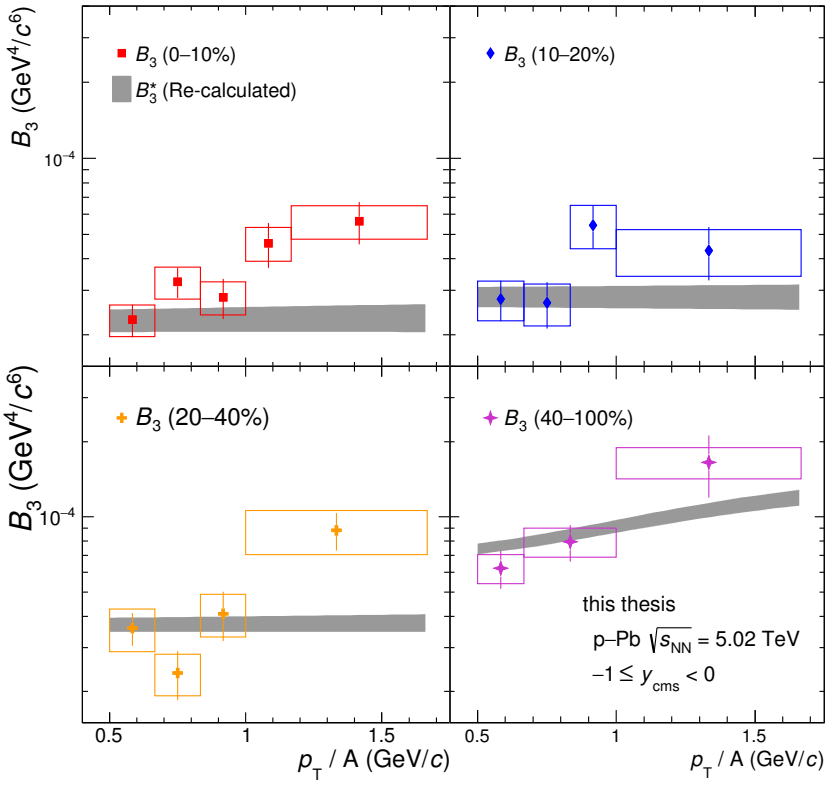

Figure 5.15: The coalescence parameter B_3 obtained in four different charged-particle multiplicity classes are compared to the recalculated coalescence parameter B_3^* which indicates the p_T dependence caused by the change of the spectral shape of the protons with multiplicity. Statistical and systematic uncertainties are indicated by vertical bars and boxes, respectively.

sions. The two parametrizations can be understood as an indication of the uncertainty band of the model description.

In addition, the measurements are compared to the expected values for the grand canonical version of the SHM, the GSI-Heidelberg model [97, 46], assuming that the transverse momentum shape is given by a Blast-Wave parametrization obtained by a simultaneous fit to the pion, kaon, and proton spectra measured in Pb–Pb collisions [138]. Since this model uses a grand canonical description, it is applicable only for high mean charged-particle multiplicity densities. If canonical suppression is taken into account, the expected B_3 deviates from the grand canonical value, as indicated in Figure 5.16 by exchanging the GSI-Heidelberg model with the Thermal-FIST model [101]. The change to the canonical ensemble description extends the applicability of the model to intermediate mean charged-particle multiplicity densities. At low $\langle \mathrm{d}N_{\mathrm{ch}}/\mathrm{d}\eta_{\mathrm{lab}} \rangle$, the assumption that the p_T shape of the nuclei follows the

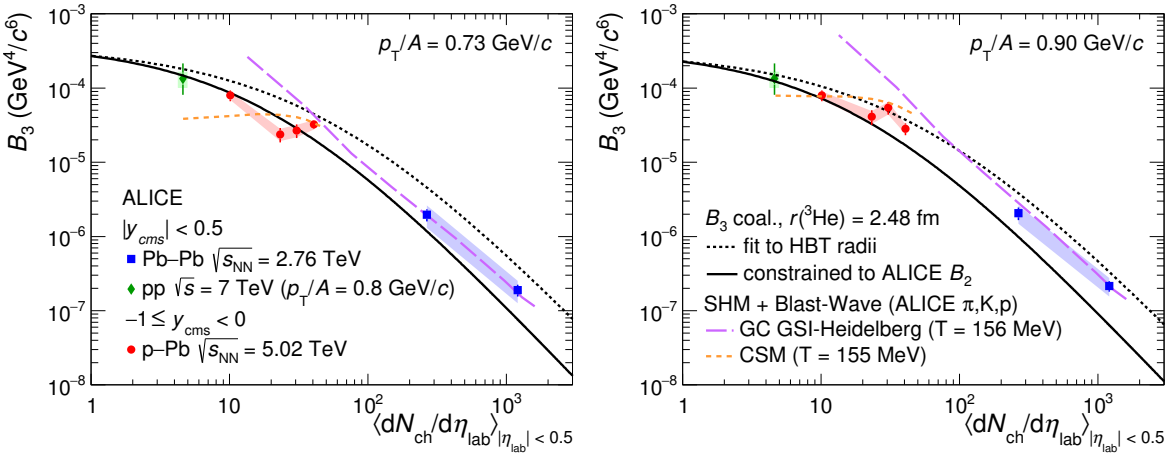

Figure 5.16: The coalescence parameter B_3, calculated using the average of ^{3}He and $^3\overline{\mathrm{He}}$, is shown as a function of the mean charged-particle multiplicity density for $p_T/A = 0.73$ GeV/c (left) and $p_T/A = 0.90$ GeV/c (right). The coalescence parameter is shown with its statistical (vertical line) and systematic (shaded bands) uncertainties. In addition, the expectations from the coalescence approach is shown for two different parametrizations of the source radius as a function of $\langle dN_{ch}/d\eta_{lab} \rangle$ [106]. To calculate the coalescence parameter from the statistical hadronization model, the spectral shape is assumed to be given by a Blast-Wave function. The SHM expectations are shown for the grand canonical [97, 46] and the canonical ensemble (CSM) version [101].

Blast-Wave parametrization breaks down. This is reflected by the larger deviation of the CSM plus Blast-Wave curve from the measurements in pp collisions for $p_T/A = 0.73$ GeV/c. Thus, the comparison between the CSM + Blast-Wave curve and the data measured in pp has to be taken with a grain of salt since it depends strongly on the difference between the true p_T-shape of the ^{3}He yield and the Blast-Wave parameterization.

The best description of the coalescence parameter B_3 is given by the coalescence expectation for low and by the SHM for higher charged-particle multiplicity densities. The measurement of B_3 presented in this thesis indicates a smooth transition between the regimes that are described by the two different approaches which could hint towards the presence of a single, system-size dependent underlying hadronization mechanism.

5.6. Upper limit on the $^4\overline{\mathrm{He}}$ production

The upper limit at 90%-confidence level on the total production yield of $^4\overline{\mathrm{He}}$ in p–Pb collisions at $\sqrt{s_{NN}}$ = 5.02 TeV is found to be $dN/dy = 2.3 \cdot 10^{-8}$. It is shown in Figure 5.17 together

with the measured total production yields corrected for the spin degeneracy factor, $2J+1$, of (anti-)protons [170], (anti-)deuterons [167], and (anti-)^{3}He at midrapidity.

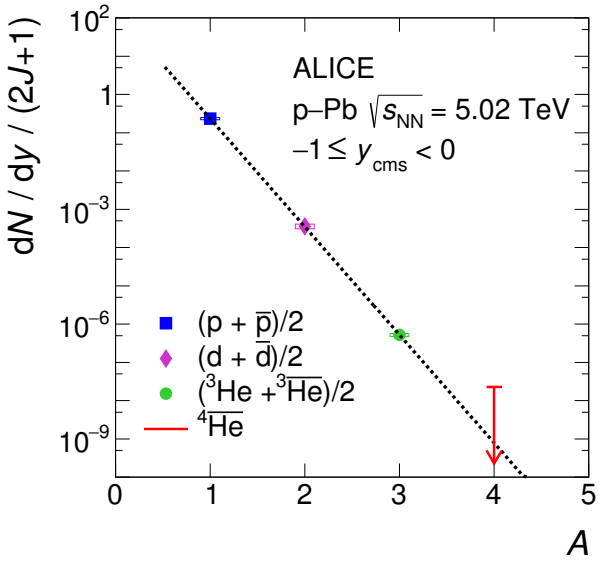

Figure 5.17: The production yields of (anti-)protons [170], (anti-)deuterons [167] and (anti-)^{3}He corrected for the spin degeneracy factor, $(2J+1)$, measured minimum-bias p–Pb collisions at $\sqrt{s_{\mathrm{NN}}}$ = 5.02 TeV are shown as a function of the mass number. In addition, the upper limit for $^4\overline{\mathrm{He}}$ is indicated. The empty boxes represent the total systematic uncertainty while the statistical uncertainties are shown by the vertical bars. The line represent the fit with an exponential function.

Previous measurements in pp collisions at $\sqrt{s} = 7$ TeV [110] and Pb–Pb collisions at $\sqrt{s_{\mathrm{NN}}}$ = 5.02 TeV [111] have indicated that the integrated yields are expected to decrease exponentially with increasing atomic number. This behaviour is also described in the SHM. Based on these observations, an exponential function is fitted to the integrated yields of the (anti-)protons, (anti-)deuterons and (anti-)^{3}He. The expected integrated yield $\mathrm{d}N/\mathrm{d}y$ for $^4\overline{\mathrm{He}}$ is obtained by extrapolation of the exponential fit to $A = 4$ and is found to be about $8 \cdot 10^{-10}$ which is more than one order of magnitude lower than the upper limit reported in this thesis. Thus, the first observation of $^4\overline{\mathrm{He}}$ should be possible in future if the data sample is at least a factor of 30 larger than the current. The penalty factor, which suppresses the integrated yield of a nucleus for each additional nucleon, is found to be 668 ± 45 in p–Pb collisions which is similar to 635 ± 90 reported previously by the ALICE collaboration [167]. The latter was obtained using the smaller p–Pb data set collected in 2013 for the determination of the total production yield of (anti-)^{3}He, which has about a factor of 3 and 5 times lager statistical and systematic uncertainties compared to the one presented in this thesis, respectively.

6. Conclusion and outlook

The p_{T}-differential yields of ^{3}H and ^{3}He nuclei and their antinuclei are measured within $1.5 \leq p_{\mathrm{T}} < 3$ GeV/c and $1.5 \leq p_{\mathrm{T}} < 5$ GeV/c in INEL > 0 p–Pb collisions at $\sqrt{s_{\mathrm{NN}}} = 5.02$ TeV with ALICE at the LHC, respectively. The (anti-)^{3}He spectra are found to be in good agreement with the previously published result by ALICE [167] within uncertainties. The production yield of (anti-)^{3}He is also studied in four different classes of charged-particle multiplicity. This is not possible for (anti-)^{3}H because of the worse separation of the $\mathrm{d}E/\mathrm{d}x$ signal from other particle species in the TPC compared to (anti-)^{3}He which leads to the need of additional particle identification information from the time-of-flight detector. This additional requirement reduces the reconstruction efficiency and thus, the number of ^{3}H candidates is not sufficient to study the multiplicity dependence. The yield ratio of antinuclei to nuclei is consistent with unity in all the measured transverse momentum and multiplicity intervals as expected considering that antimatter and matter are produced in equal amounts at the LHC. This observation is consistent with other measurements of (anti-)deuterons, (anti-)^{3}H and (anti-)^{3}He in pp, p–Pb and Pb–Pb collisions at different center-of-mass energies at the LHC [110, 167, 111]. An increasing trend of the mean transverse momentum of (anti-)^{3}He with increasing charged-particle multiplicity is observed which fits to the measurements in pp and Pb–Pb collisions and hints at a hardening of the spectra. This could be explained by an enhanced production of light nuclei in jets or collective expansion effects. The latter would indicate that (anti-)^{3}He or its constituents participate in the hydrodynamical expansion of the medium and the $\langle p_{\mathrm{T}} \rangle$ of the (anti-)nuclei should follow a mass ordering as observed for π, K, p, Λ [170], Ξ, and Ω [183]. For measurements performed at a similar values of $\langle \mathrm{d}N_{\mathrm{ch}}/\mathrm{d}\eta_{\mathrm{lab}} \rangle$, the mean transverse momenta of deuterons and (anti-)^{3}He deviate from the linear mass scaling observed for the aforementioned particles. Measurements of even heavier nuclei, like ^{4}He, would help to clarify if there is a linear mass scaling with different parameters also for nuclei or not. If it is not present, this would indicate that the light (anti-)nuclei do not participate in the hydrodynamic evolution of the medium or the signature of the participation of their constituents is altered by the process of nuclei formation. However, the analyzed data set is not large enough to observe primary (anti-)^{4}He. Thus, an upper limit for the production of $^4\overline{\mathrm{He}}$ is obtained based on the

non-observation of candidates. The measurement of (anti-)^{4}He in p–Pb collisions is much more difficult than (anti-)^{3}He because the production yield is suppressed by an additional factor of 668 ± 45. This number is obtained from the measured proton [170], deuteron [167], and ^{3}He integrated production yields. The comparison between the expected production yield of (anti-)^{4}He and the upper limit indicates that an about 30 times larger data set would be needed to observe $^4\overline{\mathrm{He}}$ in p–Pb for the first time at the LHC. Another possibility to gain insight on the question of the degree of thermalization of light nuclei and their constituents is to measure their anisotropic flow coefficients. However, the available p–Pb data set is not yet sufficiently large for such a study. First measurements of the elliptic flow, v_2, of (anti-)^{3}He in 0–20%, 20–40%, and 40–60% central Pb–Pb collisions at $\sqrt{s_{\mathrm{NN}}} = 5.02$ TeV at the LHC has been published by the ALICE collaboration [185]. A positive v_2 has been found which is compatible with a state-of-the-art model combining a viscous hydrodynamic expansion of the medium with the coalescence approach [186]. Thus, the (anti-)nuclei yields in Pb–Pb collisions seem to be affected by effects due to the collective expansion of the medium.

The ratio of the integrated yields of (anti-)^{3}He and protons is studied as a function of the mean charged-particle multiplicity density in p–Pb which indicates a smooth trend connecting the result obtained in pp and Pb–Pb collisions. The observed ^{3}He/p yield ratios are in agreement with the theoretical expectations from the canonical statistical hadronization [101] and the coalescence model [121], even though the measurements in p–Pb have a tendency to be below the calculations. Since also the coalescence parameter B_3 shows a smooth evolution with the mean charged-particle multiplicity density for different transverse-momentum intervals, this could hint towards a single, system-size dependent underlying hadronization mechanism. Unfortunately, the precision of the data and the theory predictions are not yet good enough to put strong constraints on the theoretical description. In the future, larger data sets of pp, p–Pb and Pb–Pb collisions will be available to measure not only (anti-)^{3}He and (anti-)^{3}H in finer multiplicity intervals but also (anti-)$^3_\Lambda$H and maybe heavier (anti-)hypernuclei. This will allow for a more detailed study of the observed trend and would put stronger constraints for the theoretical description. The B_3 parameters calculated from (anti-)^{3}He at different $\langle \mathrm{d}N_{\mathrm{ch}}/\mathrm{d}\eta_{\mathrm{lab}} \rangle$ contribute to the estimation of the $^3\overline{\mathrm{He}}$ background [187] in the searches for segregated primordial antimatter and dark matter via satellite-borne instruments, like AMS-02 [112]. These calculations employ the scaling of the coalescence parameter with the size of the emitting system which can be validated against the measurements. In contrast to most coalescence expectations, the measured coalescence parameter B_3 shows an increasing trend with p_{T}/A which is not compatible with the expectation of a flat B_3 even in small charged-particle multiplicity subintervals. Only about a quarter of the observed increase with p_{T}/A can be explained by the

change of the spectral shape of protons with $\langle \mathrm{d}N_{\mathrm{ch}}/\mathrm{d}\eta_{\mathrm{lab}} \rangle$ but the dominate process responsible for this behavior is not yet known. One possibility to improve the coalescence expectations is to take the measured transverse-momentum dependence of the size of the medium produced in the collision into account [92] which is one of the parameters entering the modern calculations of the coalescence parameter.

For the first time, the ^{3}H-to-^{3}He yield ratio is measured. Even though the measurement presented in this thesis is not yet conclusive due to the large uncertainties, an apparent deviation of the ^{3}H/^{3}He yield ratio from unity can be observed which would slightly favors the coalescence description including the dependence on the radii of the nucleus and the emitting source over the simple coalescence and the statistical hadronization description. The measurement indicates an increasing trend with p_{T} which might be explained within the coalescence approach via the transverse-momentum dependence of the system size observed via two-particle correlations [92]. According to recent coalescence predictions [106, 121], the ^{3}H-to-^{3}He yield ratio increasingly deviates from unity with the charged-particle multiplicity density going from Pb-Pb to pp collisions. This could be studied by measuring the p_{T}-differential production yields of (anti-) ^{3}H and (anti-)^{3}He for different charged-particle multiplicity densities which again requires larger data sets not only for p–Pb collisions but also for pp and Pb–Pb collisions.

Fortunately, the issue of the statistical precision and the limited size of the data set will be addressed by the ALICE collaboration in future data taking campaigns because the collision and readout rates will be increased to at least 200 kHz in p–Pb collisions [154]. To cope with such high rates, the ALICE detector is upgraded [155] and, especially the readout chambers of the TPC will be exchanged going from multi-wire proportional chambers to gas electron multipliers. These do not only amplify the signal but also hinder the ions from flowing back into the detector volume. Together with the upgrade of the readout electronics, this will allow to operate the TPC in continuous readout mode. ALICE is expected to collect two p–Pb data sets corresponding to 300 nb^{-1} each during LHC Run 3 and 4 [188]. This corresponds to an increase of the size of the data set by about a factor of 1000 for each data taking campaign compared to the data size employed in the presented analysis. The two data sets might be taken at different strength of the ALICE magnetic field which would make a combined analysis more difficult and possibly affected by additional systematic uncertainties. Nevertheless, already the increase in the size of the data set collected in one of the future LHC runs will allow to measure the production of light (hyper-)nuclei and their antiparticle more differentially and with improved precision challenging the theoretical descriptions and offering more detailed insight about the underlying hadronization process.

A. Publications

I am also the main author of [1], in which the analyses presented in this thesis are also published. This paper is published in the peer-reviewed journal *Physical Review C*. In addition, I participated in the preparation of [2] which is published in the peer-reviewed journal *Physics Letters B*.

I have presented recent results on the production of light (anti-)nuclei measured in pp, p–Pb and Pb–Pb collisions with ALICE at the *European Physical Society Conference on High Energy Physics* 2019 in Ghent, Belgium and published a conference proceeding [3] which includes the preliminary version of the presented analyses.

The results of my master's thesis about the measurement of electrons from semi-electronic decays of hadrons containing heavy-flavor quarks are published in [4].

List of publications

[1] Shreyasi Acharya et al. "Production of (anti-)^{3}He and (anti-)^{3}H in p–Pb collisions at $\sqrt{s_{\mathrm{NN}}}$ = 5.02 TeV". In: *Phys. Rev.* C101.4 (Apr. 2020), p. 044906. DOI: 10.1103/PhysRevC.101.044906. arXiv: 1910.14401 [nucl-ex].

[2] Shreyasi Acharya et al. "Measurement of the (anti-)^{3}He elliptic flow in Pb-Pb collisions at $\sqrt{s_{\mathrm{NN}}}$ = 5.02 TeV". In: *Phys. Lett. B* 805 (2020), p. 135414. DOI: 10.1016/j.physletb.2020.135414. arXiv: 1910.09718 [nucl-ex].

[3] Sebastian Hornung. "(Anti-)nuclei production and flow in pp, p–Pb and Pb–Pb collisions with ALICE". In: *2019 European Physical Society Conference on High Energy Physics (EPS-HEP2019) Ghent, Belgium, July 10-17, 2019*. 2019. arXiv: 1910.00438 [nucl-ex].

[4] Shreyasi Acharya et al. "Measurements of low-p$_T$ electrons from semileptonic heavy-flavour hadron decays at mid-rapidity in pp and Pb-Pb collisions at $\sqrt{s_{\mathrm{NN}}} = 2.76$ TeV". In: *JHEP* 10 (2018), p. 061. DOI: 10.1007/JHEP10(2018)061. arXiv: 1805.04379 [nucl-ex].

Bibliography

[1] M. Tanabashi et al. “Review of Particle Physics”. In: *Phys. Rev.* D98.3 (2018), p. 030001. DOI: 10.1103/PhysRevD.98.030001.

[2] Keith A. Olive. “Inflation”. In: *Phys. Rept.* 190 (1990), pp. 307–403. DOI: 10.1016/0370-1573(90)90144-Q.

[3] 2014. URL: https://particleadventure.org/history-universe.html.

[4] Mark Thomson. *Modern particle physics*. New York: Cambridge University Press, 2013. ISBN: 9781107034266.

[5] Andrei D. Linde. “Phase Transitions in Gauge Theories and Cosmology”. In: *Rept. Prog. Phys.* 42 (1979), p. 389. DOI: 10.1088/0034-4885/42/3/001.

[6] Alan H. Guth. “The Inflationary Universe: A Possible Solution to the Horizon and Flatness Problems”. In: *Phys. Rev.* D23 (1981). [Adv. Ser. Astrophys. Cosmol.3,139(1987)], pp. 347–356. DOI: 10.1103/PhysRevD.23.347.

[7] Csaba Balazs. “Baryogenesis: A small review of the big picture”. In: (2014). arXiv: 1411.3398 [hep-ph].

[8] A. D. Sakharov. “Violation of CP Invariance, C asymmetry, and baryon asymmetry of the universe”. In: *Pisma Zh. Eksp. Teor. Fiz.* 5 (1967). [JETP Lett.5,24(1967); Sov. Phys. Usp.34,no.5,392(1991); Usp. Fiz. Nauk161,no.5,61(1991)], pp. 32–35. DOI: 10.1070/PU1991v034n05ABEH002497.

[9] Y. Akrami et al. “Planck 2018 results. I. Overview and the cosmological legacy of Planck”. In: (2018). arXiv: 1807.06205 [astro-ph.CO].

[10] Craig J. Copi, David N. Schramm, and Michael S. Turner. “Big bang nucleosynthesis and the baryon density of the universe”. In: *Science* 267 (1995), pp. 192–199. DOI: 10.1126/science.7809624. arXiv: astro-ph/9407006 [astro-ph].

[11] R. H. Dicke et al. “Cosmic Black-Body Radiation”. In: *Astrophys. J.* 142 (1965), pp. 414–419. DOI: 10.1086/148306.

[12] Dominik J. Schwarz. “The first second of the universe”. In: *Annalen Phys.* 12 (2003), pp. 220–270. DOI: 10.1002/andp.200310010. arXiv: astro-ph/0303574 [astro-ph].

[13] Johann Rafelski. "Connecting QGP-Heavy Ion Physics to the Early Universe". In: (2013). [Nucl. Phys. Proc. Suppl.243-244,155(2013)].
DOI: 10.1016/j.nuclphysbps.2013.09.017. arXiv: 1306.2471 [astro-ph.CO].

[14] F. Englert and R. Brout. "Broken Symmetry and the Mass of Gauge Vector Mesons". In: *Phys. Rev. Lett.* 13 (1964), pp. 321–323.
DOI: 10.1103/PhysRevLett.13.321.

[15] Peter W. Higgs. "Broken Symmetries and the Masses of Gauge Bosons". In: *Phys. Rev. Lett.* 13 (1964), pp. 508–509.
DOI: 10.1103/PhysRevLett.13.508.

[16] Peter W. Higgs. "Broken symmetries, massless particles and gauge fields". In: *Phys. Lett.* 12 (1964), pp. 132–133.
DOI: 10.1016/0031-9163(64)91136-9.

[17] B. Povh et al. *Particles and nuclei: An Introduction to the physical concepts*. Graduate Texts in Physics. Springer, 1995. ISBN: 978-3-662-46320-8, 978-3-662-46321-5.
DOI: 10.1007/3-540-36684-9.

[18] Kenneth G. Wilson. "Confinement of Quarks". In: (Feb. 1974), pp. 45–59.
DOI: 10.1103/PhysRevD.10.2445.

[19] A. Chodos et al. "A New Extended Model of Hadrons". In: *Phys. Rev.* D9 (1974), pp. 3471–3495.
DOI: 10.1103/PhysRevD.9.3471.

[20] N. Tetradis. "The Quark meson model and the phase diagram of two flavor QCD". In: *Nucl. Phys.* A726 (2003), pp. 93–119.
DOI: 10.1016/S0375-9474(03)01624-5. arXiv: hep-th/0303244 [hep-th].

[21] Bernd-Jochen Schaefer and Jochen Wambach. "The Phase diagram of the quark meson model". In: *Nucl. Phys.* A757 (2005), pp. 479–492.
DOI: 10.1016/j.nuclphysa.2005.04.012. arXiv: nucl-th/0403039 [nucl-th].

[22] Paulo F. Bedaque and Ubirajara van Kolck. "Effective field theory for few nucleon systems". In: *Ann. Rev. Nucl. Part. Sci.* 52 (2002), pp. 339–396.
DOI: 10.1146/annurev.nucl.52.050102.090637. arXiv: nucl-th/0203055.

[23] N. Cabibbo and G. Parisi. "Exponential Hadronic Spectrum and Quark Liberation". In: *Phys. Lett.* 59B (1975), pp. 67–69.
DOI: 10.1016/0370-2693(75)90158-6.

[24] John C. Collins and M. J. Perry. "Superdense Matter: Neutrons Or Asymptotically Free Quarks?" In: *Phys. Rev. Lett.* 34 (1975), p. 1353.
DOI: 10.1103/PhysRevLett.34.1353.

[25] M. Durante et al. "All the fun of the FAIR: fundamental physics at the facility for antiproton and ion research". In: *Phys. Scripta* 94.3 (2019), p. 033001.
DOI: 10.1088/1402-4896/aaf93f. arXiv: 1903.05693 [nucl-th].

[26] Tanmoy Bhattacharya et al. "QCD Phase Transition with Chiral Quarks and Physical Quark Masses". In: *Phys. Rev. Lett.* 113.8 (2014), p. 082001.
DOI: 10.1103/PhysRevLett.113.082001. arXiv: 1402.5175 [hep-lat].

[27] P. Rosnet. "Quark-Gluon Plasma: from accelerator experiments to early Universe". In: *11th Rencontres du Vietnam: Cosmology: 50 years after CMB discovery Quy Nhon, Vietnam, August 16-22, 2015*. 2015. arXiv: 1510.04200 [hep-ph].

[28] Philippe de Forcrand. "Simulating QCD at finite density". In: *Proceedings, 27th International Symposium on Lattice field theory (Lattice 2009): Beijing, P.R. China, July 26-31, 2009*. Vol. LAT2009. 2009, p. 010.
DOI: 10.22323/1.091.0010. arXiv: 1005.0539 [hep-lat].

[29] Bertrand C. Barrois. "Superconducting Quark Matter". In: *Nucl. Phys.* B129 (1977), pp. 390–396.
DOI: 10.1016/0550-3213(77)90123-7.

[30] Mark G. Alford, Krishna Rajagopal, and Frank Wilczek. "QCD at finite baryon density: Nucleon droplets and color superconductivity". In: *Phys. Lett.* B422 (1998), pp. 247–256.
DOI: 10.1016/S0370-2693(98)00051-3. arXiv: hep-ph/9711395 [hep-ph].

[31] Lyndon Evans and Philip Bryant. "LHC Machine". In: *JINST* 3 (2008), S08001.
DOI: 10.1088/1748-0221/3/08/S08001.

[32] David Tlusty. "The RHIC Beam Energy Scan Phase II: Physics and Upgrades". In: *13th Conference on the Intersections of Particle and Nuclear Physics (CIPANP 2018) Palm Springs, California, USA, May 29-June 3, 2018*. 2018. arXiv: 1810.04767 [nucl-ex].

[33] T. Ablyazimov et al. "Challenges in QCD matter physics –The scientific programme of the Compressed Baryonic Matter experiment at FAIR". In: *Eur. Phys. J.* A53.3 (2017), p. 60.
DOI: 10.1140/epja/i2017-12248-y. arXiv: 1607.01487 [nucl-ex].

[34] K. Aamodt et al. "Two-pion Bose-Einstein correlations in central Pb–Pb collisions at $\sqrt{s_{NN}} = 2.76$ TeV". In: *Phys. Lett.* B696 (2011), pp. 328–337.
DOI: 10.1016/j.physletb.2010.12.053. arXiv: 1012.4035 [nucl-ex].

[35] Peter Braun-Munzinger and Benjamin Dönigus. "Loosely-bound objects produced in nuclear collisions at the LHC". In: *Nucl. Phys.* A987 (2019), pp. 144–201.
DOI: 10.1016/j.nuclphysa.2019.02.006. arXiv: 1809.04681 [nucl-ex].

[36] Michael L. Miller et al. "Glauber modeling in high energy nuclear collisions". In: *Ann. Rev. Nucl. Part. Sci.* 57 (2007), pp. 205–243.
DOI: 10.1146/annurev.nucl.57.090506.123020. arXiv: nucl-ex/0701025 [nucl-ex].

[37] Bjoern Schenke, Prithwish Tribedy, and Raju Venugopalan. "Fluctuating Glasma initial conditions and flow in heavy ion collisions". In: *Phys. Rev. Lett.* 108 (2012), p. 252301.
DOI: 10.1103/PhysRevLett.108.252301. arXiv: 1202.6646 [nucl-th].

[38] J. Scott Moreland, Jonah E. Bernhard, and Steffen A. Bass. "Alternative ansatz to wounded nucleon and binary collision scaling in high-energy nuclear collisions". In: *Phys. Rev.* C92.1 (2015), p. 011901.
DOI: 10.1103/PhysRevC.92.011901. arXiv: 1412.4708 [nucl-th].

[39] H. Niemi, K. J. Eskola, and R. Paatelainen. "Event-by-event fluctuations in a perturbative QCD + saturation + hydrodynamics model: Determining QCD matter shear viscosity in ultrarelativistic heavy-ion collisions". In: *Phys. Rev.* C93.2 (2016), p. 024907.
DOI: 10.1103/PhysRevC.93.024907. arXiv: 1505.02677 [hep-ph].

[40] T. Wibig and D. Sobczynska. "Proton–nucleus cross section at high energies". In: *J. Phys.* G24 (1998), pp. 2037–2047.
DOI: 10.1088/0954-3899/24/11/006. arXiv: hep-ph/9809494 [hep-ph].

[41] J. Bartels, Krzysztof J. Golec-Biernat, and H. Kowalski. "A modification of the saturation model: DGLAP evolution". In: *Phys. Rev.* D66 (2002), p. 014001.
DOI: 10.1103/PhysRevD.66.014001. arXiv: hep-ph/0203258 [hep-ph].

[42] Edmond Iancu and Raju Venugopalan. "The Color glass condensate and high-energy scattering in QCD". In: *Quark Gluon Plasma 3*. Ed. by R. C. Hwa and X.N. Wang. World Scientific, Singapore, 2003, pp. 249–3363.
DOI: 10.1142/9789812795533_0005. arXiv: hep-ph/0303204 [hep-ph].

[43] Raju Venugopalan. "From Glasma to Quark-Gluon Plasma in heavy-ion collisions". In: *J. Phys.* G35 (2008), p. 104003.
DOI: 10.1088/0954-3899/35/10/104003. arXiv: 0806.1356 [hep-ph].

[44] K. A. Bugaev et al. "Thermodynamically Anomalous Regions and Possible New Signals of Mixed Phase Formation". In: *Eur. Phys. J.* A52.6 (2016), p. 175.
DOI: 10.1140/epja/i2016-16175-1. arXiv: 1412.0718 [nucl-th].

[45] V. A. Kizka et al. "A possible evidence of the hadron-quark-gluon mixed phase formation in nuclear collisions". In: (2015). arXiv: 1504.06483 [hep-ph].

[46] Anton Andronic et al. "Decoding the phase structure of QCD via particle production at high energy". In: *Nature* 561.7723 (2018), pp. 321–330.
DOI: 10.1038/s41586-018-0491-6. arXiv: 1710.09425 [nucl-th].

[47] Raimond Snellings. "Collective Expansion at the LHC: selected ALICE anisotropic flow measurements". In: *J. Phys.* G41.12 (2014), p. 124007.
DOI: 10.1088/0954-3899/41/12/124007. arXiv: 1408.2532 [nucl-ex].

[48] K. Adcox et al. "Centrality dependence of charged particle multiplicity in Au–Au collisions at $\sqrt{s_{\mathrm{NN}}} = 130$ GeV". In: *Phys. Rev. Lett.* 86 (2001), pp. 3500–3505.
DOI: 10.1103/PhysRevLett.86.3500. arXiv: nucl-ex/0012008 [nucl-ex].

[49] G. J. Alner et al. "An Investigation of Multiplicity Distributions in Different Pseudorapidity Intervals in $\overline{\mathrm{p}}\mathrm{p}$ Reactions at a C.M.S. Energy of 540 GeV". In: *Phys. Lett.* 160B (1985), pp. 193–198.
DOI: 10.1016/0370-2693(85)91491-1.

[50] K. Aamodt et al. "Charged-particle multiplicity measurement in proton-proton collisions at $\sqrt{s} = 0.9$ and 2.36 TeV with ALICE at LHC". In: *Eur. Phys. J.* C68 (2010), pp. 89–108.
DOI: 10.1140/epjc/s10052-010-1339-x. arXiv: 1004.3034 [hep-ex].

[51] Betty Abelev et al. "Centrality determination of Pb–Pb collisions at $\sqrt{s_{\mathrm{NN}}} = 2.76$ TeV with ALICE". In: *Phys. Rev.* C88.4 (2013), p. 044909.
DOI: 10.1103/PhysRevC.88.044909. arXiv: 1301.4361 [nucl-ex].

[52] *Centrality dependence of the charged-particle multiplicity density at midrapidity in Pb–Pb collisions at $\sqrt{s_{\mathrm{NN}}} = 5.02$ TeV*. Dec. 2015. URL: https://cds.cern.ch/record/2118084.

[53] Betty Bezverkhny Abelev et al. "Transverse momentum dependence of inclusive primary charged-particle production in p–Pb collisions at $\sqrt{s_{\mathrm{NN}}} = 5.02$ TeV". In: *Eur. Phys. J.* C74.9 (2014), p. 3054.
DOI: 10.1140/epjc/s10052-014-3054-5. arXiv: 1405.2737 [nucl-ex].

[54] B. Z. Kopeliovich et al. "Cronin effect in hadron production off nuclei". In: *Phys. Rev. Lett.* 88 (2002), p. 232303.
DOI: 10.1103/PhysRevLett.88.232303. arXiv: hep-ph/0201010 [hep-ph].

[55] Rainer J. Fries, Kyongchol Han, and Che Ming Ko. "Jet Hadronization via Recombination of Parton Showers in Vacuum and in Medium". In: *Proceedings, 7th International Conference on Hard and Electromagnetic Probes of High-Energy Nuclear Collisions (Hard Probes 2015): Montréal, Québec, Canada, June 29-July 3, 2015*. 2016.
DOI: 10.1016/j.nuclphysbps.2016.05.068. arXiv: 1511.06742 [nucl-th].

[56] S. Acharya et al. "Transverse momentum spectra and nuclear modification factors of charged particles in pp, p–Pb and Pb–Pb collisions at the LHC". In: *JHEP* 11 (2018), p. 013.
DOI: 10.1007/JHEP11(2018)013. arXiv: 1802.09145 [nucl-ex].

[57] Yuri L. Dokshitzer, Valery A. Khoze, and S. I. Troian. "On specific QCD properties of heavy quark fragmentation ('dead cone')". In: *J. Phys.* G17 (1991), pp. 1602–1604.
DOI: 10.1088/0954-3899/17/10/023.

[58] Ramona Lea. "Nuclear modification of light flavour and strangeness at LHC energies with ALICE". In: *J. Phys. Conf. Ser.* 878.1 (2017), p. 012006.
DOI: 10.1088/1742-6596/878/1/012006.

[59] Jeremy Wilkinson. "Open heavy-flavour production in heavy-ion collisions at the LHC". In: *J. Phys. Conf. Ser.* 1137.1 (2019), p. 012032.
DOI: 10.1088/1742-6596/1137/1/012032. arXiv: 1809.01899 [nucl-ex].

[60] Karen M. Burke et al. "Extracting the jet transport coefficient from jet quenching in high-energy heavy-ion collisions". In: *Phys. Rev.* C90.1 (2014), p. 014909. DOI: 10.1103/PhysRevC.90.014909. arXiv: 1312.5003 [nucl-th].

[61] Francesco Scardina et al. "Estimating the charm quark diffusion coefficient and thermalization time from D meson spectra at energies available at the BNL Relativistic Heavy Ion Collider and the CERN Large Hadron Collider". In: *Phys. Rev.* C96.4 (2017), p. 044905. DOI: 10.1103/PhysRevC.96.044905. arXiv: 1707.05452 [nucl-th].

[62] T. Matsui and H. Satz. "J/ψ Suppression by Quark-Gluon Plasma Formation". In: *Phys. Lett.* B178 (1986), pp. 416–422. DOI: 10.1016/0370-2693(86)91404-8.

[63] B. Alessandro et al. "A New measurement of J/ψ suppression in Pb–Pb collisions at 158 GeV per nucleon". In: *Eur. Phys. J.* C39 (2005), pp. 335–345. DOI: 10.1140/epjc/s2004-02107-9. arXiv: hep-ex/0412036 [hep-ex].

[64] R. Arnaldi et al. "J/ψ production in indium-indium collisions at 158 GeV/nucleon". In: *Phys. Rev. Lett.* 99 (2007), p. 132302. DOI: 10.1103/PhysRevLett.99.132302.

[65] A. Adare et al. "J/ψ Production vs Centrality, Transverse Momentum, and Rapidity in Au+Au Collisions at $\sqrt{s_{\mathrm{NN}}} = 200$ GeV". In: *Phys. Rev. Lett.* 98 (2007), p. 232301. DOI: 10.1103/PhysRevLett.98.232301. arXiv: nucl-ex/0611020 [nucl-ex].

[66] B. I. Abelev et al. "J/ψ production at high transverse momentum in p+p and Cu+Cu collisions at $\sqrt{s_{\mathrm{NN}}} = 200$ GeV". In: *Phys. Rev.* C80 (2009), p. 041902. DOI: 10.1103/PhysRevC.80.041902. arXiv: 0904.0439 [nucl-ex].

[67] F. Karsch, D. Kharzeev, and H. Satz. "Sequential charmonium dissociation". In: *Phys. Lett.* B637 (2006), pp. 75–80. DOI: 10.1016/j.physletb.2006.03.078. arXiv: hep-ph/0512239 [hep-ph].

[68] Peter Braun-Munzinger and Johanna Stachel. "On charm production near the phase boundary". In: *Nucl. Phys.* A690 (2001), pp. 119–126. DOI: 10.1016/S0375-9474(01)00936-8. arXiv: nucl-th/0012064 [nucl-th].

[69] Robert L. Thews, Martin Schroedter, and Johann Rafelski. "Enhanced J/ψ production in deconfined quark matter". In: *Phys. Rev.* C63 (2001), p. 054905. DOI: 10.1103/PhysRevC.63.054905. arXiv: hep-ph/0007323 [hep-ph].

[70] L. Grandchamp and R. Rapp. "Charmonium suppression and regeneration from SPS to RHIC". In: *Nucl. Phys.* A709 (2002), pp. 415–439. DOI: 10.1016/S0375-9474(02)01027-8. arXiv: hep-ph/0205305 [hep-ph].

[71] Shreyasi Acharya et al. "Studies of J/ψ production at forward rapidity in Pb–Pb collisions at $\sqrt{s_{\mathrm{NN}}}$ = 5.02 TeV". In: *JHEP* 02 (2020), p. 041. DOI: 10.1007/JHEP02(2020)041. arXiv: 1909.03158 [nucl-ex].

[72] S. Digal, P. Petreczky, and H. Satz. "Quarkonium feed down and sequential suppression". In: *Phys. Rev.* D64 (2001), p. 094015.
DOI: 10.1103/PhysRevD.64.094015. arXiv: hep-ph/0106017 [hep-ph].

[73] Z. Hu et al. "Review of bottomonium measurements from CMS". In: *Int. J. Mod. Phys.* A32.19n20 (2017), p. 1730015.
DOI: 10.1142/S0217751X17300150. arXiv: 1708.02913 [hep-ex].

[74] Ulrich W. Heinz. "'RHIC serves the perfect fluid': Hydrodynamic flow of the QGP". In: *Proceedings, Workshop on Extreme QCD, 2005*. 2005, pp. 3–12. arXiv: nucl-th/0512051 [nucl-th].

[75] Ekkard Schnedermann, Josef Sollfrank, and Ulrich W. Heinz. "Thermal phenomenology of hadrons from 200*A* GeV S+S collisions". In: *Phys. Rev.* C48 (1993), pp. 2462–2475.
DOI: 10.1103/PhysRevC.48.2462. arXiv: nucl-th/9307020 [nucl-th].

[76] Shreyasi Acharya et al. "Production of charged pions, kaons and (anti-)protons in Pb–Pb and inelastic pp collisions at $\sqrt{s_{\mathrm{NN}}}$ = 5.02 TeV". In: (2019). arXiv: 1910.07678 [nucl-ex].

[77] Ulrich W. Heinz. "Concepts of heavy-ion physics". In: *2002 European School of high-energy physics, Pylos, Greece, 25 Aug-7 Sep 2002: Proceedings*. 2004, pp. 165–238. arXiv: hep-ph/0407360 [hep-ph]. URL: http://doc.cern.ch/yellowrep/CERN-2004-001.

[78] Arthur M. Poskanzer and S. A. Voloshin. "Methods for analyzing anisotropic flow in relativistic nuclear collisions". In: *Phys. Rev.* C58 (1998), pp. 1671–1678.
DOI: 10.1103/PhysRevC.58.1671. arXiv: nucl-ex/9805001 [nucl-ex].

[79] S. Acharya et al. "Anisotropic flow of identified particles in Pb–Pb collisions at $\sqrt{s_{\mathrm{NN}}}$ = 5.02 TeV". In: *JHEP* 09 (2018), p. 006.
DOI: 10.1007/JHEP09(2018)006. arXiv: 1805.04390 [nucl-ex].

[80] Denes Molnar and Sergei A. Voloshin. "Elliptic flow at large transverse momenta from quark coalescence". In: *Phys. Rev. Lett.* 91 (2003), p. 092301.
DOI: 10.1103/PhysRevLett.91.092301. arXiv: nucl-th/0302014 [nucl-th].

[81] Jonah E. Bernhard, J. Scott Moreland, and Steffen A. Bass. "Bayesian estimation of the specific shear and bulk viscosity of quark–gluon plasma". In: *Nature Phys.* 15.11 (2019), pp. 1113–1117.
DOI: 10.1038/s41567-019-0611-8.

[82] R. Hanbury Brown and R. Q. Twiss. "A New type of interferometer for use in radio astronomy". In: *Phil. Mag. Ser.7* 45 (1954), pp. 663–682.
DOI: 10.1080/14786440708520475.

[83] Michael Annan Lisa et al. "Femtoscopy in relativistic heavy ion collisions". In: *Ann. Rev. Nucl. Part. Sci.* 55 (2005), pp. 357–402.
DOI: 10.1146/annurev.nucl.55.090704.151533. arXiv: nucl-ex/0505014 [nucl-ex].

[84] G. F. Bertsch. "Pion Interferometry as a Probe of the Plasma". In: *Nucl. Phys.* A498 (1989). [,254(1989)], pp. 173C–180C.
DOI: 10.1016/0375-9474(89)90597-6.

[85] S. Pratt. "Pion Interferometry of Quark-Gluon Plasma". In: *Phys. Rev.* D33 (1986), pp. 1314–1327.
DOI: 10.1103/PhysRevD.33.1314.

[86] S. E. Koonin. "Proton Pictures of High-Energy Nuclear Collisions". In: *Phys. Lett.* 70B (1977), pp. 43–47.
DOI: 10.1016/0370-2693(77)90340-9.

[87] S. Pratt, T. Csorgo, and J. Zimanyi. "Detailed predictions for two pion correlations in ultrarelativistic heavy ion collisions". In: *Phys. Rev.* C42 (1990), pp. 2646–2652.
DOI: 10.1103/PhysRevC.42.2646.

[88] Richard Lednicky. "Finite-size effects on two-particle production in continuous and discrete spectrum". In: *Phys. Part. Nucl.* 40 (2009), pp. 307–352.
DOI: 10.1134/S1063779609030034. arXiv: nucl-th/0501065 [nucl-th].

[89] J. Adams et al. "Pion interferometry in Au+Au collisions at $\sqrt{s_{\mathrm{NN}}} = 200$ GeV". In: *Phys. Rev.* C71 (2005), p. 044906.
DOI: 10.1103/PhysRevC.71.044906. arXiv: nucl-ex/0411036 [nucl-ex].

[90] K. Adcox et al. "Transverse-mass dependence of two pion correlations in Au + Au collisions at $\sqrt{s_{\mathrm{NN}}} = 130$ GeV". In: *Phys. Rev. Lett.* 88 (2002), p. 192302.
DOI: 10.1103/PhysRevLett.88.192302. arXiv: nucl-ex/0201008 [nucl-ex].

[91] D. Adamová et al. "Beam energy and centrality dependence of two pion Bose-Einstein correlations at SPS energies". In: *Nucl. Phys.* A714 (2003), pp. 124–144.
DOI: 10.1016/S0375-9474(02)01369-6. arXiv: nucl-ex/0207005 [nucl-ex].

[92] Jaroslav Adam et al. "Centrality dependence of pion freeze-out radii in Pb–Pb collisions at $\sqrt{s_{\mathrm{NN}}} = 2.76$ TeV". In: *Phys. Rev.* C93.2 (2016), p. 024905.
DOI: 10.1103/PhysRevC.93.024905. arXiv: 1507.06842 [nucl-ex].

[93] Adam Kisiel et al. "Azimuthally-sensitive femtoscopy from RHIC to LHC in hydrodynamics with statistical hadronization". In: *Phys. Rev.* C79 (2009), p. 014902.
DOI: 10.1103/PhysRevC.79.014902. arXiv: 0808.3363 [nucl-th].

[94] J. Adam et al. "Two-pion femtoscopy in p–Pb collisions at $\sqrt{s_{\mathrm{NN}}} = 5.02$ TeV". In: *Phys. Rev.* C91 (2015), p. 034906.
DOI: 10.1103/PhysRevC.91.034906. arXiv: 1502.00559 [nucl-ex].

[95] Shreyasi Acharya et al. "First Observation of an Attractive Interaction between a Proton and a Cascade Baryon". In: *Phys. Rev. Lett.* 123.11 (2019), p. 112002.
DOI: 10.1103/PhysRevLett.123.112002. arXiv: 1904.12198 [nucl-ex].

[96] Tetsuo Hatsuda et al. "$p\Xi^-$ Correlation in Relativistic Heavy Ion Collisions with Nucleon-Hyperon Interaction from Lattice QCD". In: *Nucl. Phys.* A967 (2017), pp. 856–859.
DOI: 10.1016/j.nuclphysa.2017.04.041. arXiv: 1704.05225 [nucl-th].

[97] A. Andronic et al. “Production of light nuclei, hypernuclei and their antiparticles in relativistic nuclear collisions”. In: *Phys. Lett.* B697 (2011), pp. 203–207. DOI: 10.1016/j.physletb.2011.01.053. arXiv: 1010.2995 [nucl-th].

[98] S. Wheaton and J. Cleymans. “THERMUS: A Thermal model package for ROOT”. In: *Comput. Phys. Commun.* 180 (2009), pp. 84–106. DOI: 10.1016/j.cpc.2008.08.001. arXiv: hep-ph/0407174 [hep-ph].

[99] Giorgio Torrieri et al. “SHARE: Statistical hadronization with resonances”. In: *Comput. Phys. Commun.* 167 (2005), pp. 229–251. DOI: 10.1016/j.cpc.2005.01.004. arXiv: nucl-th/0404083 [nucl-th].

[100] Anton Andronic et al. “The thermal proton yield anomaly in Pb–Pb collisions at the LHC and its resolution”. In: *Phys. Lett.* B792 (2019), pp. 304–309. DOI: 10.1016/j.physletb.2019.03.052. arXiv: 1808.03102 [hep-ph].

[101] Volodymyr Vovchenko, Benjamin Dönigus, and Horst Stoecker. “Multiplicity dependence of light nuclei production at LHC energies in the canonical statistical model”. In: *Phys. Lett.* B785 (2018), pp. 171–174. DOI: 10.1016/j.physletb.2018.08.041. arXiv: 1808.05245 [hep-ph].

[102] Volodymyr Vovchenko et al. “Nucleosynthesis in heavy-ion collisions at the LHC via the Saha equation”. In: *Phys. Lett.* B800 (2020), p. 135131. DOI: 10.1016/j.physletb.2019.135131. arXiv: 1903.10024 [hep-ph].

[103] Dmytro Oliinychenko et al. “Microscopic study of deuteron production in PbPb collisions at $\sqrt{s} = 2.76$ TeV via hydrodynamics and a hadronic afterburner”. In: *Phys. Rev.* C99.4 (2019), p. 044907. DOI: 10.1103/PhysRevC.99.044907. arXiv: 1809.03071 [hep-ph].

[104] J. Weil et al. “Particle production and equilibrium properties within a new hadron transport approach for heavy-ion collisions”. In: *Phys. Rev.* C94.5 (2016), p. 054905. DOI: 10.1103/PhysRevC.94.054905. arXiv: 1606.06642 [nucl-th].

[105] Joseph I. Kapusta. “Mechanisms for deuteron production in relativistic nuclear collisions”. In: *Phys. Rev.* C21 (1980), pp. 1301–1310. DOI: 10.1103/PhysRevC.21.1301.

[106] Francesca Bellini and Alexander Philipp Kalweit. “Testing production scenarios for (anti-)(hyper-)nuclei and exotica at energies available at the CERN Large Hadron Collider”. In: *Phys. Rev.* C99.5 (2019), p. 054905. DOI: 10.1103/PhysRevC.99.054905. arXiv: 1807.05894 [hep-ph].

[107] R. Scheibl and Ulrich W. Heinz. “(Anti-)deuteron coalescence in ultrarelativistic heavy ion collisions”. In: (1997). arXiv: nucl-th/9701053 [nucl-th].

[108] Francesca Bellini and Alexander P. Kalweit. “Testing production scenarios for (anti-)(hyper-)nuclei with multiplicity-dependent measurements at the LHC”. In: *Acta Phys. Polon.* B50 (2019), p. 991. DOI: 10.5506/APhysPolB.50.991. arXiv: 1907.06868 [hep-ph].

[109] J. Steinheimer et al. “Hypernuclei, dibaryon and antinuclei production in high energy heavy ion collisions: Thermal production versus Coalescence”. In: *Phys. Lett.* B714 (2012), pp. 85–91.
DOI: 10.1016/j.physletb.2012.06.069. arXiv: 1203.2547 [nucl-th].

[110] Shreyasi Acharya et al. “Production of deuterons, tritons, ^{3}He nuclei and their antinuclei in pp collisions at $\sqrt{s}$ = 0.9, 2.76 and 7 TeV”. In: *Phys. Rev.* C97.2 (2018), p. 024615.
DOI: 10.1103/PhysRevC.97.024615. arXiv: 1709.08522 [nucl-ex].

[111] Jaroslav Adam et al. “Production of light nuclei and anti-nuclei in pp and Pb–Pb collisions at energies available at the CERN Large Hadron Collider”. In: *Phys. Rev.* C93.2 (2016), p. 024917.
DOI: 10.1103/PhysRevC.93.024917. arXiv: 1506.08951 [nucl-ex].

[112] Andrei Kounine. “The Alpha Magnetic Spectrometer on the International Space Station”. In: *Int. J. Mod. Phys.* E21.08 (2012), p. 1230005.
DOI: 10.1142/S0218301312300056.

[113] Enrico Fermi. “High-energy nuclear events”. In: *Prog. Theor. Phys.* 5 (1950), pp. 570–583.
DOI: 10.1143/PTP.5.570.

[114] F. Becattini and L. Ferroni. “Statistical hadronization and hadronic microcanonical ensemble II”. In: *Eur. Phys. J.* C38 (2004). [Erratum: Eur. Phys. J.66,341(2010)], pp. 225–246.
DOI: 10.1140/epjc/s10052-010-1243-4, 10.1140/epjc/s2004-02027-8. arXiv: hep-ph/0407117 [hep-ph].

[115] R. Hagedorn. “How We Got to QCD Matter from the Hadron Side: 1984”. In: *Lect. Notes Phys.* 221 (1985). [,287(2016)], pp. 53–76.
DOI: 10.1007/978-3-319-17545-4_25.

[116] Roger Dashen, Shang-Keng Ma, and Herbert J. Bernstein. “*S*-Matrix formulation of statistical mechanics”. In: *Phys. Rev.* 187 (1969), pp. 345–370.
DOI: 10.1103/PhysRev.187.345.

[117] Francesco Becattini. “What is the meaning of the statistical hadronization model?” In: *Focus on multiplicity. Proceedings, International Workshop on Particle Multiplicity in Relativistic Heavy Ion Collisions, Bari, Italy, June 17-19, 2004*. Vol. 5. [,175(2004)]. 2005, pp. 175–188.
DOI: 10.1088/1742-6596/5/1/015. arXiv: hep-ph/0410403 [hep-ph].

[118] Peter Braun-Munzinger, Krzysztof Redlich, and Johanna Stachel. “Particle production in heavy ion collisions”. In: *Quark Gluon Plasma 3*. Ed. by R. C. Hwa and X.N. Wang. World Scientific, Singapore, 2003, pp. 491–599.
DOI: 10.1142/9789812795533_0008. arXiv: nucl-th/0304013 [nucl-th].

[119] Francesco Becattini. “A Thermodynamical approach to hadron production in e^+ e^- collisions”. In: *Z. Phys.* C69.3 (1996), pp. 485–492.
DOI: 10.1007/BF02907431.

[120] A. Andronic et al. "Thermal description of hadron production in e^+e^- collisions revisited". In: *Phys. Lett.* B675 (2009), pp. 312–318.
DOI: 10.1016/j.physletb.2009.04.024. arXiv: 0804.4132 [hep-ph].

[121] Kai-Jia Sun, Che Ming Ko, and Benjamin Dönigus. "Suppression of light nuclei production in collisions of small systems at the Large Hadron Collider". In: *Phys. Lett.* B792 (2019), pp. 132–137.
DOI: 10.1016/j.physletb.2019.03.033. arXiv: 1812.05175 [nucl-th].

[122] Sebastian Hornung. "(Anti-)nuclei production and flow in pp, p–Pb and Pb–Pb collisions with ALICE". In: *2019 European Physical Society Conference on High Energy Physics (EPS-HEP2019) Ghent, Belgium, July 10-17, 2019*. 2019. arXiv: 1910.00438 [nucl-ex].

[123] Volodymyr Vovchenko, Benjamin Dönigus, and Horst Stoecker. "Canonical statistical model analysis of p–p, p–Pb, and Pb–Pb collisions at the LHC". In: *Phys. Rev.* C100.5 (2019), p. 054906.
DOI: 10.1103/PhysRevC.100.054906. arXiv: 1906.03145 [hep-ph].

[124] Rudiger Scheibl and Ulrich W. Heinz. "Coalescence and flow in ultrarelativistic heavy ion collisions". In: *Phys. Rev.* C59 (1999), pp. 1585–1602.
DOI: 10.1103/PhysRevC.59.1585. arXiv: nucl-th/9809092 [nucl-th].

[125] Fred Cooper and Graham Frye. "Comment on the Single Particle Distribution in the Hydrodynamic and Statistical Thermodynamic Models of Multiparticle Production". In: *Phys. Rev.* D10 (1974), p. 186.
DOI: 10.1103/PhysRevD.10.186.

[126] Urs Achim Wiedemann, Pierre Scotto, and Ulrich W. Heinz. "Transverse momentum dependence of Hanbury-Brown–Twiss correlation radii". In: *Phys. Rev.* C53 (1996), pp. 918–931.
DOI: 10.1103/PhysRevC.53.918. arXiv: nucl-th/9508040 [nucl-th].

[127] Ulrich W. Heinz et al. "Lifetimes and sizes from two particle correlation functions". In: *Phys. Lett.* B382 (1996), pp. 181–188.
DOI: 10.1016/0370-2693(96)00657-0. arXiv: nucl-th/9603011 [nucl-th].

[128] Ulrich W. Heinz. "How to extract physics from HBT radius parameters". In: *Nucl. Phys.* A610 (1996), pp. 264C–277C.
DOI: 10.1016/S0375-9474(96)00361-2. arXiv: nucl-th/9608002 [nucl-th].

[129] C. M. Herbach et al. "Charged-particle evaporation and pre-equilibrium emission in 1.2 GeV proton-induced spallation reactions". In: *Nucl. Phys.* A765 (2006), pp. 426–463.
DOI: 10.1016/j.nuclphysa.2005.10.014.

[130] J. Cugnon, C. Volant, and S. Vuillier. "Improved intranuclear cascade model for nucleon-nucleus interactions". In: *Nucl. Phys.* A620 (1997), pp. 475–509.
DOI: 10.1016/S0375-9474(97)00186-3.

[131] J. Cugnon. “INTRANUCLEAR CASCADE MODEL. A REVIEW”. In: *Nucl. Phys.* A387 (1982), pp. 191C–203C.
DOI: 10.1016/0375-9474(82)90200-7.

[132] J. J. Griffin. “Statistical Model of Intermediate Structure”. In: *Phys. Rev. Lett.* 17 (1966), pp. 478–481.
DOI: 10.1103/PhysRevLett.17.478.

[133] M. Blann. “Hybrid Model for Pre-Equilibrium Decay in Nuclear Reactions”. In: *Phys. Rev. Lett.* 27.6 (1971), p. 337.
DOI: 10.1103/PhysRevLett.27.337.

[134] A. Boudard et al. “A new model for production of fast light clusters in spallation reactions”. In: *Nucl. Phys.* A740 (2004), pp. 195–210.
DOI: 10.1016/j.nuclphysa.2004.05.003.

[135] Walter Hauser and Herman Feshbach. “The Inelastic Scattering of Neutrons”. In: *Phys. Rev.* 87 (1952), pp. 366–373.
DOI: 10.1103/PhysRev.87.366.

[136] V. F. Weisskopf and D. H. Ewing. “On the Yield of Nuclear Reactions with Heavy Elements”. In: *Phys. Rev.* 57.6 (1940), p. 472.
DOI: 10.1103/PhysRev.57.472.

[137] Niels Bohr and John Archibald Wheeler. “The Mechanism of nuclear fission”. In: *Phys. Rev.* 56 (1939), pp. 426–450.
DOI: 10.1103/PhysRev.56.426.

[138] Betty Abelev et al. “Centrality dependence of π, K, p production in Pb–Pb collisions at $\sqrt{s_{\mathrm{NN}}} = 2.76$ TeV”. In: *Phys. Rev.* C88 (2013), p. 044910.
DOI: 10.1103/PhysRevC.88.044910. arXiv: 1303.0737 [hep-ex].

[139] Michael Benedikt et al. *LHC Design Report*. CERN Yellow Reports: Monographs. Geneva: CERN, 2004.
DOI: 10.5170/CERN-2004-003-V-3. URL: https://cds.cern.ch/record/823808.

[140] Esma Mobs. *The CERN accelerator complex - August 2018. Complexe des accélérateurs du CERN - Août 2018*. General Photo. Aug. 2018. URL: https://cds.cern.ch/record/2636343.

[141] G. Aad et al. “The ATLAS Experiment at the CERN Large Hadron Collider”. In: *JINST* 3 (2008), S08003.
DOI: 10.1088/1748-0221/3/08/S08003.

[142] S. Chatrchyan et al. “The CMS Experiment at the CERN LHC”. In: *JINST* 3 (2008), S08004.
DOI: 10.1088/1748-0221/3/08/S08004.

[143] G. Anelli et al. “The TOTEM experiment at the CERN Large Hadron Collider”. In: *JINST* 3 (2008), S08007.
DOI: 10.1088/1748-0221/3/08/S08007.

[144] O. Adriani et al. "The LHCf detector at the CERN Large Hadron Collider". In: *JINST* 3 (2008), S08006.
DOI: 10.1088/1748-0221/3/08/S08006.

[145] A. Augusto Alves Jr. et al. "The LHCb Detector at the LHC". In: *JINST* 3 (2008), S08005.
DOI: 10.1088/1748-0221/3/08/S08005.

[146] James L. Pinfold. "The MoEDAL experiment at the LHC - A new light on the high energy frontier". In: *Mod. Phys. Lett.* A29 (2014), p. 1430003.
DOI: 10.1142/S0217732314300031.

[147] K. Aamodt et al. "The ALICE experiment at the CERN LHC". In: *JINST* 3 (2008), S08002.
DOI: 10.1088/1748-0221/3/08/S08002.

[148] J. Schukraft. "Heavy-ion physics with the ALICE experiment at the CERN Large Hadron Collider". In: *Phil. Trans. Roy. Soc. Lond.* A370 (2012), pp. 917–932.
DOI: 10.1098/rsta.2011.0469. arXiv: 1109.4291 [hep-ex].

[149] Francesco Noferini. "ALICE results from Run-1 and Run-2 and perspectives for Run-3 and Run-4". In: *J. Phys. Conf. Ser.* 1014.1 (2018), p. 012010.
DOI: 10.1088/1742-6596/1014/1/012010.

[150] Betty Bezverkhny Abelev et al. "Performance of the ALICE Experiment at the CERN LHC". In: *Int. J. Mod. Phys.* A29 (2014), p. 1430044.
DOI: 10.1142/S0217751X14300440. arXiv: 1402.4476 [nucl-ex].

[151] E. Abbas et al. "Performance of the ALICE VZERO system". In: *JINST* 8 (2013), P10016.
DOI: 10.1088/1748-0221/8/10/P10016. arXiv: 1306.3130 [nucl-ex].

[152] K Aamodt et al. "Alignment of the ALICE Inner Tracking System with cosmic-ray tracks". In: *JINST* 5 (2010), P03003.
DOI: 10.1088/1748-0221/5/03/P03003. arXiv: 1001.0502 [physics.ins-det].

[153] *Upgrade of the ALICE Time Projection Chamber*. Tech. rep. CERN-LHCC-2013-020. ALICE-TDR-016. Oct. 2013. URL: https://cds.cern.ch/record/1622286.

[154] B Abelev et al. "Upgrade of the ALICE Experiment: Letter Of Intent". In: *J. Phys. G* 41 (2014), p. 087001.
DOI: 10.1088/0954-3899/41/8/087001.

[155] *ALICE upgrade physics performance studies for 2018 Report on HL/HE-LHC physics*. Feb. 2019. URL: https://cds.cern.ch/record/2661798.

[156] M. Bondila et al. "ALICE T0 detector". In: *IEEE Trans. Nucl. Sci.* 52 (2005), pp. 1705–1711.
DOI: 10.1109/TNS.2005.856900.

[157] Jaroslav Adam et al. "Determination of the event collision time with the ALICE detector at the LHC". In: *Eur. Phys. J. Plus* 132.2 (2017), p. 99.
DOI: 10.1140/epjp/i2017-11279-1. arXiv: 1610.03055 [physics.ins-det].

[158] A. Akindinov et al. “Performance of the ALICE Time-Of-Flight detector at the LHC”. In: *Eur. Phys. J. Plus* 128 (2013), p. 44.
DOI: 10.1140/epjp/i2013-13044-x.

[159] R. Fruhwirth. “Application of Kalman filtering to track and vertex fitting”. In: *Nucl. Instrum. Meth.* A262 (1987), pp. 444–450.
DOI: 10.1016/0168-9002(87)90887-4.

[160] Torbjorn Sjostrand, Stephen Mrenna, and Peter Z. Skands. “A Brief Introduction to PYTHIA 8.1”. In: *Comput. Phys. Commun.* 178 (2008), pp. 852–867.
DOI: 10.1016/j.cpc.2008.01.036. arXiv: 0710.3820 [hep-ph].

[161] Johannes Bellm et al. “Herwig 7.0/Herwig++ 3.0 release note”. In: *Eur. Phys. J.* C76.4 (2016), p. 196.
DOI: 10.1140/epjc/s10052-016-4018-8. arXiv: 1512.01178 [hep-ph].

[162] T. Pierog et al. “EPOS LHC: Test of collective hadronization with data measured at the CERN Large Hadron Collider”. In: *Phys. Rev.* C92.3 (2015), p. 034906.
DOI: 10.1103/PhysRevC.92.034906. arXiv: 1306.0121 [hep-ph].

[163] Xin-Nian Wang and Miklos Gyulassy. “HIJING: A Monte Carlo model for multiple jet production in pp, pA and AA collisions”. In: *Phys. Rev.* D44 (1991), pp. 3501–3516.
DOI: 10.1103/PhysRevD.44.3501.

[164] Stefan Roesler, Ralph Engel, and Johannes Ranft. “The Monte Carlo event generator DPMJET-III”. In: *Advanced Monte Carlo for radiation physics, particle transport simulation and applications. Proceedings, Conference, MC2000, Lisbon, Portugal, October 23-26, 2000*. 2000, pp. 1033–1038.
DOI: 10.1007/978-3-642-18211-2_166. arXiv: hep-ph/0012252 [hep-ph].
URL: http://www-public.slac.stanford.edu/sciDoc/docMeta.aspx?slacPubNumber=SLAC-PUB-8740.

[165] René Brun et al. *GEANT: Detector Description and Simulation Tool; Oct 1994*. Long Writeup W5013. Geneva, 1993.
DOI: 10.17181/CERN.MUHF.DMJ1. URL: http://cds.cern.ch/record/1082634.

[166] S. Agostinelli et al. “GEANT4: A Simulation toolkit”. In: *Nucl. Instrum. Meth.* A506 (2003), pp. 250–303.
DOI: 10.1016/S0168-9002(03)01368-8.

[167] Shreyasi Acharya et al. “Multiplicity dependence of light (anti-)nuclei production in p-Pb collisions at $\sqrt{s_{\mathrm{NN}}}$ = 5.02 TeV”. In: *Phys. Lett. B* 800 (2020), p. 135043.
DOI: 10.1016/j.physletb.2019.135043. arXiv: 1906.03136 [nucl-ex].

[168] Shreyasi Acharya et al. “Production of (anti-)^{3}He and (anti-)^{3}H in p–Pb collisions at $\sqrt{s_{\mathrm{NN}}}$ = 5.02 TeV”. In: *Phys. Rev.* C101.4 (Apr. 2020), p. 044906.
DOI: 10.1103/PhysRevC.101.044906. arXiv: 1910.14401 [nucl-ex].

[169] Betty Abelev et al. "Pseudorapidity density of charged particles in p + Pb collisions at $\sqrt{s_{\mathrm{NN}}} = 5.02$ TeV". In: *Phys. Rev. Lett.* 110.3 (2013), p. 032301. DOI: 10.1103/PhysRevLett.110.032301. arXiv: 1210.3615 [nucl-ex].

[170] Betty Bezverkhny Abelev et al. "Multiplicity Dependence of Pion, Kaon, Proton and Lambda Production in p–Pb Collisions at $\sqrt{s_{\mathrm{NN}}}$ = 5.02 TeV". In: *Phys. Lett.* B728 (2014), pp. 25–38. DOI: 10.1016/j.physletb.2013.11.020. arXiv: 1307.6796 [nucl-ex].

[171] H. Kamada et al. "Pi mesonic decay of the hypertriton". In: *Phys. Rev.* C57 (1998), pp. 1595–1603. DOI: 10.1103/PhysRevC.57.1595. arXiv: nucl-th/9709035 [nucl-th].

[172] Jaroslav Adam et al. "${}^{3}_{\Lambda}\mathrm{H}$ and ${}^{\overline{3}}_{\overline{\Lambda}}\overline{\mathrm{H}}$ production in Pb–Pb collisions at $\sqrt{s_{\mathrm{NN}}} = 2.76$ TeV". In: *Phys. Lett.* B754 (2016), pp. 360–372. DOI: 10.1016/j.physletb.2016.01.040. arXiv: 1506.08453 [nucl-ex].

[173] Roger Barlow. "Systematic errors: Facts and fictions". In: *Advanced Statistical Techniques in Particle Physics. Proceedings, Conference, Durham, UK, March 18-22, 2002*. 2002, pp. 134–144. arXiv: hep-ex/0207026 [hep-ex]. URL: http://www.ippp.dur.ac.uk/Workshops/02/statistics/proceedings//barlow.pdf.

[174] S. P. Denisov et al. "Measurements of antideuteron absorption and stripping cross sections at the momentum 13.3 GeV/c". In: *Nucl. Phys.* B31 (1971), pp. 253–260. DOI: 10.1016/0550-3213(71)90229-X.

[175] F. G. Binon et al. "Absorption cross-sections of 25 GeV/c antideuterons in Li, C, Al, Cu and Pb". In: *Phys. Lett.* 31B (1970), pp. 230–232. DOI: 10.1016/0370-2693(70)90112-7.

[176] V. Uzhinsky et al. "Antinucleus-nucleus cross sections implemented in Geant4". In: *Phys. Lett.* B705 (2011), pp. 235–239. DOI: 10.1016/j.physletb.2011.10.010.

[177] Gary J. Feldman and Robert D. Cousins. "A Unified approach to the classical statistical analysis of small signals". In: *Phys. Rev.* D57 (1998), pp. 3873–3889. DOI: 10.1103/PhysRevD.57.3873. arXiv: physics/9711021 [physics.data-an].

[178] Shreyasi Acharya et al. "Production of ${}^{4}\mathrm{He}$ and ${}^{4}\overline{\mathrm{He}}$ in Pb–Pb collisions at $\sqrt{s_{\mathrm{NN}}}$ = 2.76 TeV at the LHC". In: *Nucl. Phys.* A971 (2018), pp. 1–20. DOI: 10.1016/j.nuclphysa.2017.12.004. arXiv: 1710.07531 [nucl-ex].

[179] Jan Conrad et al. "Including systematic uncertainties in confidence interval construction for Poisson statistics". In: *Phys. Rev.* D67 (2003), p. 012002. DOI: 10.1103/PhysRevD.67.012002. arXiv: hep-ex/0202013 [hep-ex].

[180] Gary C. Hill. "Comment on 'Including systematic uncertainties in confidence interval construction for Poisson statistics'". In: *Phys. Rev.* D67 (2003), p. 118101. DOI: 10.1103/PhysRevD.67.118101. arXiv: physics/0302057 [physics].

[181] S. S. Adler et al. "Identified charged particle spectra and yields in Au+Au collisions at $\sqrt{s_{\mathrm{NN}}}$ = 200 GeV". In: *Phys. Rev.* C69 (2004), p. 034909.
DOI: 10.1103/PhysRevC.69.034909. arXiv: nucl-ex/0307022 [nucl-ex].

[182] Shreyasi Acharya et al. "Charged-particle production as a function of multiplicity and transverse spherocity in pp collisions at $\sqrt{s} = 5.02$ and 13 TeV". In: *Eur. Phys. J.* C79.10 (2019), p. 857.
DOI: 10.1140/epjc/s10052-019-7350-y. arXiv: 1905.07208 [nucl-ex].

[183] Jaroslav Adam et al. "Multi-strange baryon production in p–Pb collisions at $\sqrt{s_{\mathrm{NN}}} =$ 5.02 TeV". In: *Phys. Lett.* B758 (2016), pp. 389–401.
DOI: 10.1016/j.physletb.2016.05.027. arXiv: 1512.07227 [nucl-ex].

[184] Shreyasi Acharya et al. "Multiplicity dependence of (anti-)deuteron production in pp collisions at $\sqrt{s}$ = 7 TeV". In: *Phys. Lett.* B794 (2019), pp. 50–63.
DOI: 10.1016/j.physletb.2019.05.028. arXiv: 1902.09290 [nucl-ex].

[185] Shreyasi Acharya et al. "Measurement of the (anti-)^{3}He elliptic flow in Pb-Pb collisions at $\sqrt{s_{\mathrm{NN}}}$ = 5.02 TeV". In: *Phys. Lett. B* 805 (2020), p. 135414.
DOI: 10.1016/j.physletb.2020.135414. arXiv: 1910.09718 [nucl-ex].

[186] Wenbin Zhao et al. "Spectra and flow of light nuclei in relativistic heavy ion collisions at energies available at the BNL Relativistic Heavy Ion Collider and at the CERN Large Hadron Collider". In: *Phys. Rev.* C98.5 (2018), p. 054905.
DOI: 10.1103/PhysRevC.98.054905. arXiv: 1807.02813 [nucl-th].

[187] Kfir Blum et al. "Cosmic rays, antihelium, and an old navy spotlight". In: *Phys. Rev.* D96.10 (2017), p. 103021.
DOI: 10.1103/PhysRevD.96.103021. arXiv: 1704.05431 [astro-ph.HE].

[188] Z. Citron et al. "Report from Working Group 5: Future physics opportunities for high-density QCD at the LHC with heavy-ion and proton beams". In: *Report on the Physics at the HL-LHC,and Perspectives for the HE-LHC*. Vol. 7. Dec. 2019, pp. 1159–1410.
DOI: 10.23731/CYRM-2019-007.1159. arXiv: 1812.06772 [hep-ph].

Acknowledgements

First, I would like to thank Prof. Dr. Silvia Masciocchi for giving me the opportunity to join her group for my PhD studies and the excellent support during the last years. It had been great fun and a pleasure to be part of the ALICE group at GSI. Thanks for the welcoming and warm atmosphere. Even though, I did not manage to participate in all of the nice group activities, they have always been well organised and pleasant occasions for interesting conversations about physics and non-physics topics. My gratefulness also goes to Dr. Alberto Calivà and Dr. Kai Schweda for many helpful discussions and the support not only during the analysis project but also while preparing the publication and this thesis. In addition, I want to thank Dr. Ralf Averbeck for the valuable comments and suggestions while preparing this thesis. I would like to thank Prof. Dr. Johanna Stachel, Dr. Maximiliano Puccio and Dr. Stefano Trogolo for all the helpful comments and suggestion during the detailed review of the analyses and the paper preparation. I want to express my sincere gratitude to Prof. Dr. Anton Andronic, Dr. Benjamin Dönigus, Dr. Alexander Kalweit and Dr. Francesca Bellini for the support concerning the theory description of the hadronization process. It had been a pleasure to be part of the light flavour working group of ALICE and especially its nuclei and exotica subsection. Many thanks to all the members and the conveners for the support during the process of approving the preliminary result, the paper proposal and during the development of the analyses. I want to thank everyone involved in HSG-HIRe and HGSFP for the organization of PhD program including the lecture weeks, Graduate Days and the soft skill courses.

Mein besonderer Dank gilt meiner Familie und meinen Freunden für ihre Geduld und die vielen schönen Aktivitäten, welche ein wertvoller Ausgleich und ein Quell neuer Energie waren.